A COMPUTATIONAL FLUID DYNAMICS STUDY OF THE SMALLEST FLYING INSECTS

Shannon Kathleen Jones

A dissertation submitted to the faculty at the University of North Carolina at Chapel Hill in partial fulfillment of the requirements for the degree of Doctor of Philosophy in the Curriculum of Bioinformatics and Computational Biology.

Chapel Hill
2016

Approved by:

Laura Miller

Tyson Hedrick

Gregory Forest

William Kier

Jan Prins

ABSTRACT

Shannon Kathleen Jones: A Computational Fluid Dynamics Study of the Smallest Flying Insects
(Under the direction of Laura Miller and Tyson Hedrick)

The flight of insects has fascinated scientists for centuries, and a large body of work has focused on understanding the intricacies of the aerodynamics of these organisms. Most of this work has focused on the flight of insects ranging in size from a fruit fly to a hawkmoth. The smallest flying insects, however, are ten times smaller than a fruit fly, and much less is known about their wing kinematics and aerodynamics. These insects fly at Reynolds numbers on the order of 10, and at this scale relative viscous forces are much greater than they are for larger insects. Consequently, these small insects must overcome significant aerodynamic challenges in order to propel themselves.

The main goal of this dissertation is to better understand the challenges of flying at low Reynolds numbers and to investigate possible mechanisms to overcome those challenges. I used the immersed boundary method to solve for the fluid flow around insect wings in both two- and three-dimensions. In Chapter 3, I use a two-dimensional model to explore theoretically whether small insects could “swim” through the air using a drag-based stroke mechanism to generate vertical force. Chapter 4 investigates the aerodynamic role of bristled wings, especially engaged in wing-wing interactions. And finally, Chapter 5 introduces a three-dimensional revolving wing which is used to explore the forces and flow structures generated at low Reynolds numbers.

Overall, the results suggest that there are drastic differences in the aerodynamics of flight at the scale of the smallest flying insects, which makes their flight more challenging, compared to larger insects. As the Reynolds number decreases, drag increases and the lift-to-drag ratio decreases significantly. Chapter 3 reveals that neither lift- nor drag-based vertical force generation mechanisms are very efficient at the range of the smallest flying insects. Chapter 4 demonstrates that bristled wings could reduce the force required to fling the wings apart during clap and fling while still maintaining lift during translation. And Chapter 5 shows that both the leading edge vortex and trailing edge vortex remain attached to the wing and spanwise flow decreases as the Reynolds number is lowered.

To my parents.

ACKNOWLEDGEMENTS

I am eternally grateful to my family and friends. I would especially like to thank my parents for their continued support and assistance over the years, but especially recently for being such wonderful grandparents. My brother, Christopher, has come to my rescue during more than one inconvenient computer failure. My husband, Chris, has been a constant source of love and support all these years. And my dear little Oliver has helped me maintain perspective and remember what is most important. I'd also like to thank Becky for our long walks and chats.

My current and former lab mates have been wonderful friends and colleagues: Austin Baird, Nick Battista, Jeremy Greeter, Christy Hamlet, Alex Hoover, Julia Samson, Arvind Santhanakrishan, Dwight Springthorpe, Christopher Strickland and Lindsay Waldrop. You all have provided much needed support, feedback, and friendship. Alex's advice for using IBAMR was incredibly valuable for the work presented in this dissertation. I would also like to thank Ryan Laurenza, Carol Knight, Young Yun and Daniel Goldfarb for their assistance on projects in the Miller lab, including some of the work presented here.

Thank you to my committee members: Greg Forest, Bill Kier and Jan Prins for positive and constructive conversations about my research and career guidance. I am grateful to have such kind and supportive scientists help me along the way. I would also like to thank Boyce Griffith for making IBAMR freely available.

I'd also like to express my gratitude for the financial support I received during my graduate years. My graduate work was partially funded by a UNC Merit Assistantship, a

National Science Foundation Graduate Research Fellowship (NSF GRFP Grant No. DGE-1144081), and a graduate fellowship from SAMSI.

And last, but not least, I'd like to thank my advisors, Laura Miller and Ty Hedrick. In addition to being a brilliant scientist, Ty is always available to chat and provide his assistance. I was shocked when he asked me to present my research project at a conference just 2 months into my lab rotation with him, but I'm glad he encouraged me to push beyond my comfort zone. I'm also incredibly grateful for his support and advice as I welcomed a little one into my family. And of course, I'd like to express my deepest appreciation and gratitude to Laura for her guidance, patience, and caring. She has been a terrific advisor and friend, and she provided an excellent atmosphere for doing research. I am amazingly fortunate to have found an advisor who cares so much about her students, not just as scientists, but as individuals. I have been inspired by her kindness and selflessness on more occasions than I can count. Without her patience and support over these last few years, I would never have been able to finish my dissertation.

TABLE OF CONTENTS

LIST OF TABLES

LIST OF FIGURES

CHAPTER 1: INTRODUCTION

For more than a century, the flight of insects has fascinated scientists and the public. The flight of these organisms even seems improbable using aerodynamic theory, resulting in the lingering myth that, according to physics, "bumblebees can't fly" (McMasters 1989, Peterson 2004). As a result, a large body of work in the field of biomechanics has focused on the subtle complexities of insect flight. The majority of this work has focused on insects ranging in size from a fruit fly to a hawkmoth, whereas much less is known about the aerodynamics of the smallest insects (Ellington 1999, Dudley 2002, Miller and Peskin 2005, Miller and Peskin 2009).

Because of their small size, we know that viscosity plays a much larger role in the aerodynamics of the smallest flying insects than it does for larger insects, however details of how these insects fly still remains a mystery. To fully appreciate the challenge faced by these insects, consider the following analogy: a tiny insect flying through the air would be similar to a human trying to swim through thick syrup (Childress 1981)—no easy feat!

The focus of this work is to understand the challenges of flight at the scale of the smallest flying insects and to investigate possible mechanisms to overcome these challenges. In this introductory section, I will discuss background on small insects, the challenges of being small, and previous work on the aerodynamics of the smallest flying insects.

1.1 The smallest flying insects.

The smallest flying insects, who are less than one millimeter in length, might be mistaken for a speck of dust floating through the air. A microscope, however, reveals interesting details of these small organisms (**Fig. 1.1**). The most interesting morphological difference between small

and large insects is that many species of small insects have wings that are fringed or bristled rather than continuous (Dudley 2002).

While we rarely notice them in our day to day activities, the smallest flying insects are ubiquitous in nature. For example, over 5500 species of thrips (order Thysanoptera) have been described to date (Morse and Hoddle 2006). These insects are of significant agricultural, ecological, and economical importance. Thrips are a common agricultural pest (Palmer, Reddy et al. 1990, Crespi, Carmean et al. 1997), and parasitoid wasps have the potential to be used for natural biological control of agricultural pests (Austin and Dowton 2000). For example, a recent study demonstrated that successful biological control of thrips in California using a small predatory insect resulted in an economic benefit of nearly $60 million (Shogren and Paine 2015). These tiny insects can also transmit pollen (Terry 2001, Terry 2002), and serve as biological vectors for plant pathogens through mechanical transmission (Ullman, Meideros et al. 2002, Jones 2005).

While one might assume that such small insects would be dependent upon wind currents for locomotion (and this may be true for long distance travel), they are capable of flight over short distances (Terry 2001). Understanding the aerodynamics of flapping flight at this small scale may lead to improved dispersal strategies for biological control. Additionally, further insight into the aerodynamical limits of flight of tiny insects will be beneficial to engineers developing biologically-inspired micro-aerial vehicles (Żbikowski 2002).

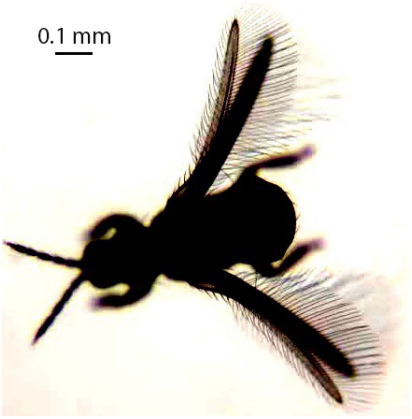

Figure 1.1. Photograph of a thrips (photo taken in Tyson Hedrick's lab at UNC by Sarah Wright).

1.2 It's difficult to be small (or life at lower Reynolds numbers).

Before I discuss the aerodynamics of small insect flight and how they differ from larger insects, it is useful to first introduce the Reynolds number (*Re*). *Re* is a dimensionless scaling parameter commonly used in fluid dynamics to predict similar patterns of flow in different fluid situations, and is defined as:

$$Re = \frac{\rho U L}{\mu}, \qquad \text{Eq. 1.1}$$

where ρ is the fluid density, U is the characteristic velocity, L is a characteristic length scale, and μ is the dynamic viscosity. The choices of U and L are somewhat arbitrary, but allow for comparisons across different organism sizes so long as the definition of the variables is consistent within a study. In studies of insect flight, U is typically the average wingtip velocity over a complete flapping cycle and L is typically the chord length of the wing. This convenient variable gives the ratio of inertial forces to viscous forces, and consequently describes the relative importance of these two forces.

Organisms that move through fluid (i.e. air or water) at *Re* approaching 1 experience greater challenges than their larger counterparts. As the *Re* decreases, the ratio of inertial forces to viscous forces decreases. Therefore, viscosity plays a much larger role in the movement of these organisms than it does for larger organisms. To overcome these challenges, different mechanisms for locomotion at low *Re* have evolved (Purcell 1977). Examples of low *Re* locomotion can be found in many organisms, including insects (Weis-Fogh 1973, Wang 2000, Sunada, Takashima et al. 2002, Miller and Peskin 2004, Miller and Peskin 2005, Miller and Peskin 2009), larval fish (Müller and van Leeuwen 2004, Müller, van den Boogaart et al. 2008, Gazzola, Van Rees et al. 2012), pteropods (Satterlie, LaBarbera et al. 1985, Borrell, Goldbogen et al. 2005) and jellyfish (Wilson, Peng et al. 2009, Herschlag and Miller 2011).

Of particular interest to this work is the length scale (L) in **Eq. 1.1**. The smallest flying insects are nearly 10 times smaller than a fruit fly and 100 times smaller than a hawkmoth (**Fig 1.2**), and that size difference plays a significant role in the aerodynamics experienced by the insects. For example, a 10-fold decrease in size (L) will increase the relative viscous forces just as much as a 10-fold increase in viscosity (μ) (Vogel 1996). Now consider that there is approximately a 100-fold decrease in *Re* from the largest ($Re \sim 1000$) to the smallest ($Re \sim 10$) flying insects. Even though both are flying in air, the relative viscous forces are 100 times greater for the smallest insects than the largest. Consequently, these small insects must overcome significant aerodynamic challenges in order to propel themselves in this *Re* range.

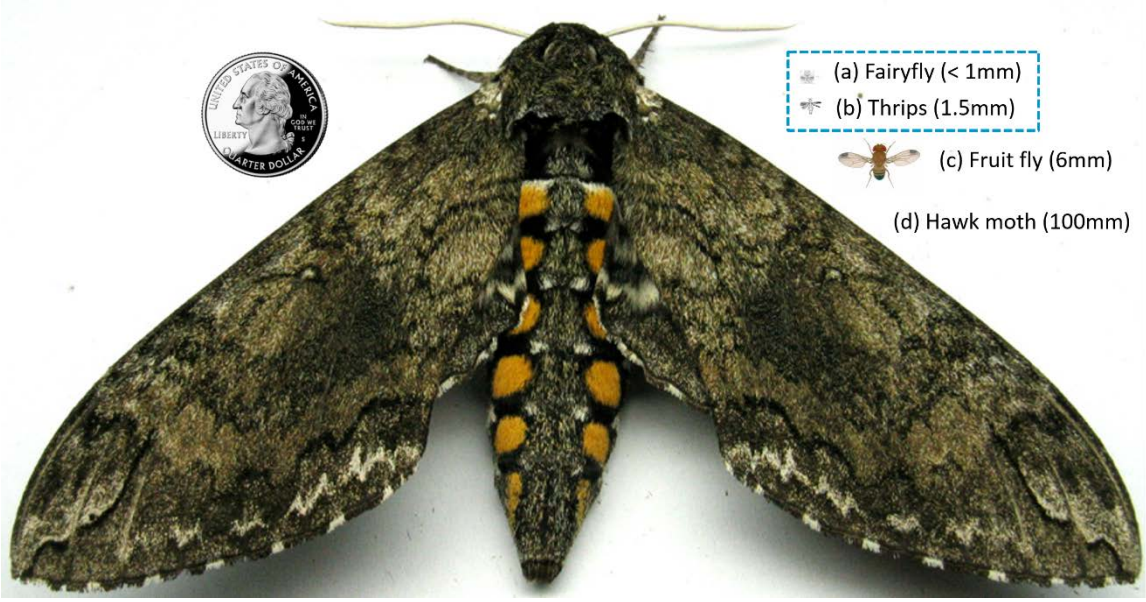

Figure 1.2. The smallest flying insects, such as (a) fairyflies and (b) thrips, fly at *Re* that are an order of magnitude smaller than (c) fruit flies, and two orders of magnitude lower than (d) hawkmoths. The lengths are the approximate wingspan lengths. The smallest flying insects are on the order of 1 mm in size (dashed box).

1.3 Aerodynamics of the smallest flying insects.

1.3.1 Previous work in small insect flight.

Previous work has shown that the flight kinematics and aerodynamics of the smallest insects may be significantly different from that of their larger counterparts (Weis-Fogh 1973, Ellington 1980, Wang 2000, Sunada, Takashima et al. 2002, Miller and Peskin 2004, Miller and Peskin 2005, Sun and Yu 2006, Miller and Peskin 2009, Kolomenskiy, Moffatt et al. 2010, Kolomenskiy, Moffatt et al. 2011, Santhanakrishnan, Robinson et al. 2014). Because of their small size and high wing beat frequency, detailed quantitative data on the wing kinematics of the smallest insects is not readily available (Sane 2003, Miller and Peskin 2009). As a result, there has been much debate and speculation about the flight strategies employed by these insects.

The smallest flying insects are on the order of 1 mm in length, and some species of fairyfly are less than 250 μm long (Huber and Noyes 2013). They have been reported to flap their wings

at frequencies greater than 200 Hz (Santhanakrishnan, Robinson et al. 2014) and possibly as high as 400 Hz (Weis-Fogh 1973) or 1000 Hz (Sotavalta 1947). At this scale and wingbeat frequency, viscous forces are significant, and the relevant *Re* are on the order of 4-60. For flying insects, *Re* is usually defined using **Eq. 1.1**, where ρ is the density of air, U is the velocity of the wingtip, L is the chord length of the wing (**Fig 1.3a**), and μ is the dynamic viscosity of air.

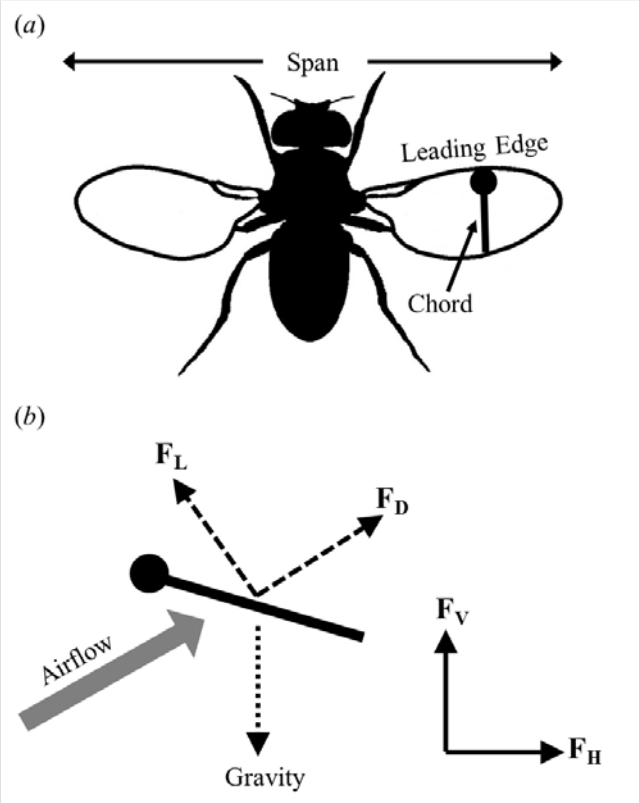

Figure 1.3. (a) A cross section through the chord of the wing provides a simplified way to study insect wing aerodynamics in two dimensions. (b) Drag (F_D) is the component of force in the direction of oncoming airflow relative to the motion of the wing, and lift (F_L) is the component of force normal to oncoming airflow. Vertical force (F_V) is the component of force opposing gravity, and horizontal force (F_H) is the component of force normal to gravity.

Well-studied insects, such as *Drosophila* (Dickinson and Gotz 1993, Dickinson, Lehmann et al. 1999) and *Manduca sexta* (Usherwood and Ellington 2002, Hedrick, Cheng et al. 2009), fly at a *Re* on the order of 100 and 1000, respectively. Smaller and less well-studied insects, such as

thrips and fairyflies, operate at a *Re* on the order of 10 or below. At this low *Re* range, the lift to drag ratio decreases significantly (Wang 2000, Miller and Peskin 2004) and the flight aerodynamics and wing kinematics differ from those of larger insects.

Video recordings of free-flying tiny insects require high-speed cameras equipped with macro-lenses and high intensity lighting; even with an ideal set-up, the field of view is very narrow. Consequently, very few tiny insect species have been filmed to date. Those that have been filmed include *Encarsia formosa* (Weis-Fogh 1973), *Trialeurodes vaporarioru* (Weis-Fogh 1975), *Thrips physapus* (Ellington 1984), *Muscidifurax raptor* and *Nasonia vitripennis* (Miller and Peskin 2009), and other species of thrips (Santhanakrishnan, Robinson et al. 2014). All of these species appear to use the 'clap and fling' mechanism.

To improve lift generation, it is thought that many tiny insects clap their wings together at the end of upstroke and fling them apart at the beginning of the downstroke in a flight mechanism called 'clap and fling' (Weis-Fogh 1973). The rotation of the wings during "fling" results in a large attached leading edge vortex on each wing (Maxworthy 1979, Spedding and Maxworthy 1986). This structure leads to larger lift forces compared with a single wing engaged in similar kinematics (Lighthill 1973, Maxworthy 1979, Ellington 1984, Ellington 1984, Spedding and Maxworthy 1986, Sun and Xin 2003, Lehmann, Sane et al. 2005, Miller and Peskin 2005, Sun and Yu 2006, Lehmann and Pick 2007, Miller and Peskin 2009). Clap and fling has been observed in tiny insects such as *Encarsia formosa* (Weis-Fogh 1973) and thrips (Ellington 1984), and larger insects such as butterflies (Srygley and Thomas 2002). While clap and fling is surely an important mechanism in small insect flight, a quantitative description of clap and fling kinematics for the smallest flying insects is still unavailable. Additionally, Miller and Peskin showed in two-dimensional simulations that very large forces are required to fling the wings apart at the low *Re*

of tiny insects (Miller and Peskin 2005). Consequently, clap and fling may not be the only flight strategy used by these organisms to overcome the challenges of flying at lower *Re*. In addition to clap and fling, drag-based strokes (Horridge 1956, Wang 2000) and bristled wings (Thompson 1942, Vogel 1996, Miller and Peskin 2009) have been proposed to aid small insects. In the following two sections, I introduce the role of drag and bristled wings in insect flight, which will be the topics of research in Chapters 3 and 4, respectively.

1.3.2 Lift vs. drag.

At this point, it would be useful to define conventional terminology that will be used throughout the following chapters (**Fig 1.3b**). I define lift as the component of force that is normal to the oncoming flow with respect to the motion of the wing, whereas I define drag as the component of force parallel to oncoming flow. In the case of a hovering insect, lift and drag are perpendicular and parallel, respectively, to the direction of wing motion. Intuitively, one might expect that lift is always "up", however lift may also be entirely downward or even horizontal since it is defined with respect to the direction of movement of the wing. To help keep this clear, I will also define two other forces: vertical force (F_V) and horizontal force (F_H). F_V is parallel to the direction of gravity, whereas F_H is normal to gravity. Unlike lift and drag, the orientation of F_V and F_H remain constant with respect to the global frame. I will adhere to these definitions of lift, drag, F_V and F_H as I investigate force production and flight aerodynamics of the smallest insects.

A lift-based strategy for small insect flight became widely accepted following Weis-Fogh's influential 1973 paper that described clap and fling (Weis-Fogh 1973). As described in the previous section, various lines of evidence supported the idea that insects increase the lift generated during flight by clapping their wings together at the end of upstroke and flinging them apart at the beginning of the downstroke (Lighthill 1973, Maxworthy 1979, Ellington 1984, Ellington 1984,

Spedding and Maxworthy 1986, Sun and Xin 2003, Lehmann, Sane et al. 2005, Miller and Peskin 2005, Sun and Yu 2006, Lehmann and Pick 2007, Miller and Peskin 2009). However, very large forces are required to fling the wings apart at the low *Re* of the smallest insects (Miller and Peskin 2005, Miller and Peskin 2009, Santhanakrishnan, Robinson et al. 2014).

A drag-based strategy for small insect flight was first suggested when Horridge proposed that small insects might generate vertical force by 'swimming' or paddling through the air, rather than using a lift-based aerofoil action (Horridge 1956). This strategy has been observed in larger insects, such as butterflies, which use a nearly-vertical stroke plane (Ellington 1984). A computational study showed that the importance of drag is frequently underestimated in hovering flight, with an idealized dragonfly wing motion supporting three quarters of the insect's weight with drag (Wang 2004). Recently, a drag-based, swimming-like mode of forward flight was observed in the fruit fly (Ristroph, Bergou et al. 2011). However, most studies of insect flight focus on insects with $Re>100$. With the challenges associated with generating lift at low *Re*, it could be beneficial for the smallest insects to use a drag-based motion to generate some or all of its vertical force. This has not, however, been rigorously investigated.

A drag-based flight mechanism works for insects at higher *Re* because the pressure drag of the downstroke is much greater than the skin friction drag of the upstroke, which generates a sufficiently high net-vertical force (Ellington 1984). However, as the *Re* approaches the Stokes regime ($Re << 1$), the drag is primarily due to skin friction, is not very sensitive to angle of attack, and is linearly proportional to velocity. A drag-based flapping flight mechanism in the Stokes regime would generate net-zero vertical force because the drag experienced during the upstroke would counter the drag-based vertical force produced during the downstroke. Therefore, I propose that there is a *Re*-based limit at which drag alone would no longer work as

an aerodynamic mechanism for vertical force production in insects. A comparison of lift- and drag- based strategies for vertical force production is discussed in detail in Chapter 3.

1.3.3 Bristled wings.

Interestingly, the smallest flying insects commonly possess wings with long bristles on the fringes (**Fig. 1.1**). Thysanoptera, Trichogrammatidae, Mymaridae, Ptiliidae, Cecidomyiidae, Ceratopogonidae, and Nepticulidae (A. Deans, personal communication, 2012) all include species that have bristled wings. Little information is available on the diameter, spacing and *Re* of bristles on tiny insect wings. The bristle-based Reynolds number (Re_b), is defined the same as **Eq. 1.1**, but the characteristic length, L, is the diameter of the bristle. The bristles on the wings of *Encarsia formosa* (Ellington 1975) and *Thrips physapus* (Kuethe 1975) function near $Re_b = 7 \times 10^{-2}$ and 1×10^{-2}, respectively; while the chord-based *Re* for these insects is on the order of 10. The ratios of gap spacing to bristle diameter are 5:1 and 10:1, respectively (Ellington 1975, Ellington 1980).

A number of studies have investigated the fluid dynamics of flow through bristled appendages similar to those on the wings of small insects (Cheer and Koehl 1987, Loudon, Best et al. 1994, Sunada, Takashima et al. 2002, Barta and Weihs 2006, Weihs and Barta 2008, Barta 2011, Davidi and Weihs 2012), however, these studies generally focus on the drag and leakiness of a row of bristles, without considering the angle of attack and more complicated kinematics. As a result, the mechanical significance of bristled insect wings remains a mystery.

Computational fluid dynamics provides a convenient way to model a row of bristles. The bristles on insect wings can be approximated as a row of cylinders (**Fig 1.4**). Many examples of flow through an infinite row of cylinders exists in the literature (Tamada and Fujikawa 1957, Fornberg 1991, Ayaz and Pedley 1999, Gajjar and Azzam 2004). When fluid is forced to flow

between the bristles of an infinite row, however, shear gradients become steeper and drag becomes higher as the gap between bristles decreases. On the other hand, in a finite row of bristles, shear gradients become less steep and drag is reduced as the width of the gap between bristles decreases (Cheer and Koehl 1987). This is because fluid is free to move both around and through the array of bristles.

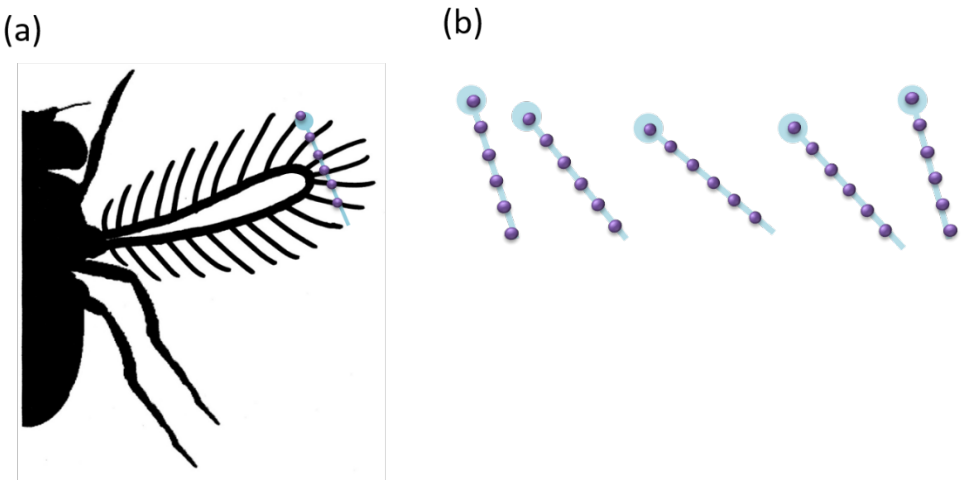

Figure 1.4. A bristled wing can be modeled in two-dimensions using a cross section through the chord of the wing (a). The row of two-dimensional cylinders can then be modeled performing desired kinematics (b).

Cheer and Koehl mathematically approximated steady state flow near a finite array of bristles in free space by considering the flow around and between a two-dimensional cross-section of a pair of circular cylinders (Cheer and Koehl 1987). They described the fluid motion mathematically at a variety of biologically relevant cylinder diameters, spacings, and Re_b. They discovered that appendages with bristles that operate at very low Re_b are paddle-like, while appendages with bristles operating at Re_b close to 1 are more leaky and rake-like (**Fig. 1.5**).

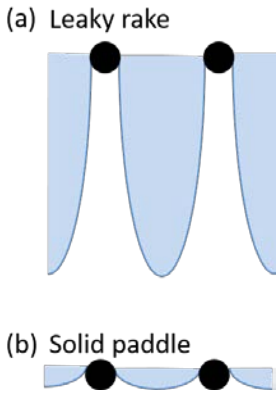

Figure. 1.5. The *Re* influences the fluid dynamic behavior of bristles. Bristles at higher Re_b are more leaky (a), while bristles at low Re_b act more like solid paddles (b).

The degree to which bristles operate as a rake versus a paddle is described as 'leakiness'. Here, the leakiness of a pair of bristles is defined as the ratio of the volume of fluid that actually moves between a pair of bristles to the volume across which that bristle pair sweeps in a unit of time (Cheer and Koehl 1987). An ideal rake would have a leakiness of 1, and an ideal paddle would have a leakiness of 0. A transition in leakiness occurs as the Re_b of the bristles or the width of the gap between them changes. This means that the bristles on tiny insect wings could act as both paddles and rakes during different portions of the stroke. The performance of bristled appendages operating at the biological conditions of thrips ($Re_b = 10^{-2}$) would be expected to change as a function of bristle spacing and velocity (Cheer and Koehl 1987).

Previous work suggests that single bristled wings are almost as effective as solid wings at producing aerodynamic forces. Sunada et al. used a dynamically scaled mechanical model of a single thrips forewing to compare the fluid dynamic forces acting on a bristled wing and a solid wing during translation and rotation. They discovered that the lift and drag acting on the bristled wing were a little smaller than those on the solid wing over a range of angles of attack (Sunada, Takashima et al. 2002). Similarly, Davidi and Weihs used computational fluid dynamics to show that bristled wings can produce a very high percentage of the force produced by solid wings

(Davidi and Weihs 2012). While these works suggest that bristles may not significantly alter the aerodynamic forces experienced by a single wing during steady translation, the bristles might offer an aerodynamic benefit during wing-wing interactions (i.e. 'clap and fling').

Miller and Peskin showed that very large forces are required to fling insect wings apart at the low *Re* relevant to tiny insects (Miller and Peskin 2005). They suggest that bristled wings could reduce the force required to clap the wings together and fling the wings apart (Miller and Peskin 2009). If the Re_b and spacing of the bristles are near the transition where the bristled appendage acts either as a solid paddle or leaky rake (Cheer and Koehl 1987), then during clap and fling it could be possible for the bristles to offer an aerodynamic benefit. The bristles could reduce the force required to "fling" the wings apart. Then the wings could preserve lift by acting as a solid plate during the translational part of the stroke. Experiments with physical models have shown that leakiness is increased when bristles move near a boundary (Loudon, Best et al. 1994). During the fling, there could be some flow between the wings' bristles enhanced by the presence of the other wing, which would reduce the force required to fling the wings apart. The idea that bristles offer an aerodynamic benefit during clap and fling is supported by a numerical study of porous wings, which showed that porous wings, compared to solid wings, reduce the drag required to move two wings apart (Santhanakrishnan, Robinson et al. 2014). A computational study of the aerodynamic role of bristles is the topic of Chapter 4.

1.4 Computational work in small insects.

1.4.1 Previous computational studies in small insect aerodynamics.

Computational fluid dynamics provide an opportune method to investigate the aerodynamics of flying insects where direct experimentation would be difficult (as is the case with tiny insects). Computational studies also have the advantage of being able to explore parameter

space and optimize the aerodynamics of the theoretical computational flier (Berman and Wang 2007, Nakata and Liu 2012, Zheng, Hedrick et al. 2013). Most of the computational studies to date have focused on larger insects (Bush and Baeder 2007, Ramamurti and Sandberg 2007, Nakata and Liu 2012, Zheng, Hedrick et al. 2013, Xu and Sun 2014), but some have investigated fliers at $Re<100$ (Wang 2000, Miller and Peskin 2004, Wang, Birch et al. 2004, Miller and Peskin 2005, Miller and Peskin 2009).

Computational fluid dynamics provides a convenient framework to compare theoretically the flight of small and large insects. For example, the forces and flow structure around a flapping wing can be compared over a range of *Re* simply by changing the dynamic viscosity while holding all other parameters constant. This has allowed for many theoretical studies that show that the aerodynamics of insect flight change as the *Re* decreases to that of the smallest flying insects. In a two-dimensional numerical study, Wang (2000) showed that when the *Re* was lowered from 157 to 15.7, the lift coefficients decreased by more than 50 percent. Similarly, Wu and Sun showed that lift coefficients decreased and drag coefficients increased when the *Re* decreased from 1800 to 20 in three-dimensional simulations (Wu and Sun 2004). Miller and Peskin (2004) found that at $Re<32$, the flow patterns around a wing are different than at $Re>64$ in two-dimensional simulations. They also showed that the force required to fling two wings apart using clap and fling is greater at lower *Re* (Miller and Peskin 2005), however these forces are somewhat reduced by wing flexibility (Miller and Peskin 2009). In addition to comparing different sized insects by changing the *Re* in a numerical simulation, different wing kinematics can be compared. For example, Wang (2004) compared fruit fly and dragonfly kinematics using a two-dimensional model.

1.4.2 Three-dimensional studies of the smallest flying insects.

Most studies of insect flight at the *Re* relevant to tiny insects have been performed in two-dimensions (Miller and Peskin 2004, Wang 2004, Wang, Birch et al. 2004, Miller and Peskin 2005, Miller and Peskin 2009, Kolomenskiy, Moffatt et al. 2010, Arora, Gupta et al. 2014, Santhanakrishnan, Robinson et al. 2014). While valuable information can be obtained from two-dimensional studies, previous research shows that differences exist between two- and three-dimensional studies. In general, two-dimensional studies fail to capture any three-dimensional effects from spanwise flow, and there can be differences in the separation of the leading edge vortex (Wang, Birch et al. 2004). Two-dimensional studies also fails to take into account that the wings of insects are rotated about a wing base, rather than translated.

A few studies have modeled tiny insect flight in three dimensions. Sun and Yu (2006) investigated the flight of a tiny insect at *Re*=15. Kolomenskiy et al. (2011) modeled three-dimensional effects during clap and fling, but did not consider *Re* below 128. And Liu and Aono (2009) modeled a thrips (*Re*=10) and fruit fly (*Re*=134) in three-dimensions, and found that the thrips did not produce as much force as a fruit fly, but they did not explore *Re* between these two cases.

To better understand the flight of the smallest flying insects, a more complete study of three-dimensional aerodynamics at low *Re* is required. In Chapter 5, I used a three-dimensional model of a revolving insect wing to compare the forces and flow structures over a range of *Re* relevant to the smallest insects. This study complements an experimental investigation by collaborators in Michael Dickinson's and Laura Miller's groups into the forces and flow structures around a dynamically scaled physical model of an insect wing. A three-dimensional numerical study can obtain additional information that enhances an experimental study. In the experimental

study, the particle image velocimetry performed on the physical model was limited to capturing the flow structures in a two-dimensional slice through the fluid domain, whereas the three-dimensional numerical study captured the three-dimensional flow structures over the entire fluid domain. Using the computational model, I investigated three-dimensional effects, such as spanwise flow. To date, this is the first study to quantify the flow structures and forces around a three-dimensional wing at a range of angles of attack and *Re* relevant to the smallest flying insects (*Re* ~ 4-100).

1.5 Concluding remarks.

In the following chapters, two-dimensional and three-dimensional computational models were developed to explore the aerodynamic forces and the flow structures around the wings of the smallest flying insects. In Chapter 3, I compare theoretical drag-based and lift-based wing strokes using a two-dimensional model to determine if tiny insects could “swim” through the air. In Chapter 4, I investigate the aerodynamic role of bristles using a two-dimensional model. And in Chapter 5, I explore the forces and flow structures around a three-dimensional wing at the *Re* relevant to tiny insects and compare these to larger insects. The goal of these studies is to better understand the aerodynamics of the smallest flying insects and to explore possible strategies these insects might use to overcome the challenges of low *Re* flight.

CHAPTER 2: METHODS

2.1 Numerical Method

2.1.1 Immersed Boundary Method.

In Chapters 3, 4, and 5, I used the immersed boundary (IB) method (Peskin 2002) to model insect wings immersed in a viscous, incompressible fluid. The IB method was first developed by Peskin in 1972 to study the flow patterns around heart valves. Since then, the immersed boundary method has been used to model a variety of biological fluid dynamics problems at low to moderate *Re*, including aquatic locomotion (Fauci and Peskin 1988, Fauci and Fogelson 1993), insect flight (Miller and Peskin 2004, Miller and Peskin 2005, Miller and Peskin 2009), bacterial flagella (Lim and Peskin 2012, Maniyeri, Suh et al. 2012), jellyfish swimming (Herschlag and Miller 2011) and ciliary driven flows (Grunbaum, Eyre et al. 1998).

Because the structure (in this case, an insect wing) changes the fluid flow and the fluid moves the structure simultaneously, coupling the deformation of the structure and the fluid flow is a challenging numerical problem. The IB method solves this fluid-structure interaction at low to intermediate *Re* by solving the fluid and the elasticity equations on separate grids using different frames of reference. The viscous, incompressible fluid equations are discretized on a fixed Cartesian grid in the Eulerian frame, whereas the structure is defined on a curvilinear mesh in the Lagrangian frame **(Fig. 2.1**). The structure moves freely through the Cartesian grid without being constrained to the grid's node points. This allows the fluid grid to be relatively coarse, without limiting the geometric complexity of the structure, resulting in reduced computational expense. The Eulerian and Lagrangian equations are coupled by interaction equations that

involve integral transforms with delta function kernels: forces generated by the structure are spread to the local fluid and the structure is moved at the local fluid velocity.

The Navier-Stokes equations govern the motion for the viscous, incompressible fluid. Here I provide the formulation for two dimensions, but the extension to three dimensions is straightforward (at least in terms of the formulation itself):

$$\rho\left(\frac{\partial \boldsymbol{u}(\boldsymbol{x},t)}{\partial t} + \boldsymbol{u}(\boldsymbol{x},t)\cdot\nabla\boldsymbol{u}(\boldsymbol{x},t)\right) = -\nabla p(\boldsymbol{x},t) + \mu\Delta\boldsymbol{u}(\boldsymbol{x},t) + \boldsymbol{f}(\boldsymbol{x},t), \qquad \text{Eq. 2.1}$$

$$\nabla\cdot\boldsymbol{u}(\boldsymbol{x},t) = 0 \qquad \text{Eq. 2.2}$$

where $\boldsymbol{u}(\boldsymbol{x},t)$ is the fluid velocity at position **x**=[*x*,*y*] and time *t*, $p(\boldsymbol{x},t)$ is the pressure, and **f(x,***t***)** is the force per unit area applied to the fluid by the structure. **Eq. 2.1** is the momentum equation, and is essentially Newton's second law of motion, *F=ma*, for a parcel of fluid. **Eq. 2.2** is the incompressibility condition.

The force term, $\boldsymbol{f}(\boldsymbol{x},t)$, from **Eq 2.1** depends on the application, but can include resistance of the structure to bending and stretching, applied forces required to move the structure with a preferred motion, force due to the action of muscles, and other external forces. In the following chapters, the force is a result of (1) prescribed motion of the structure using target points and (2) resistance of the structure to bending and stretching:

$$\boldsymbol{F}(r,t) = \boldsymbol{F}_{\boldsymbol{target}}(r,t) + \boldsymbol{F}_{\boldsymbol{elastic}}(r,t), \qquad \text{Eq. 2.3}$$

where **F**(*r*,*t*) is the force per unit length applied to the body as a function of Lagrangian position *r* and time *t*, $\boldsymbol{F}_{target}(r,t)$ is the force per unit length applied by a target point to the immersed boundary point (discussed below), and $\boldsymbol{F}_{elastic}(r,t)$ is the force per unit length as a result of resistance of the structure to bending and stretching.

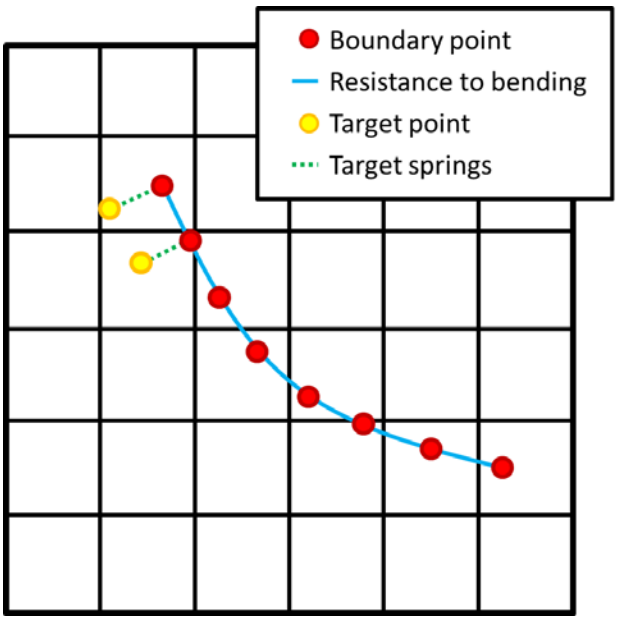

Figure 2.1. In the immersed boundary method, the fluid is discretized on a fixed Cartesian grid in the Eulerian frame, whereas the structure (red circles) is defined on a curvilinear mesh in the Lagrangian frame. The blue lines represent resistance to bending and stretching. The structure can be made to move in a prescribed way by using target points (yellow circles) attached to the structure via springs (green, dashed lines).

A common way to prescribe the preferred motion of a structure is to apply a penalty force, $\boldsymbol{F}_{target}$, that is proportional to the displacement of the immersed boundary from a target boundary (Kim and Peskin 2007). The boundary is tethered to the target boundary by elastic springs (**Fig. 2.1**). The target points on the target boundary are given Cartesian coordinates that may change in time. At each time step of the numerical method, the position of the target points are updated. When the immersed boundary points of the structure deviate from the position of

the target points, a linear spring force is applied that is proportional to the distance between the two points.

$$\boldsymbol{F_{target}}(r,t) = k_{target}\big(\boldsymbol{X}(r,t) - \boldsymbol{Y}(r,t)\big), \qquad \text{Eq. 2.4}$$

where k_{target} is the spring stiffness, $\boldsymbol{X}(r,t)$ is the Cartesian position of the boundary at position r, and $\boldsymbol{Y}(r,t)$ is the Cartesian position of the target boundary at position r. The stiffness of the springs, k_{target}, is selected so that the force is large enough to move the boundary close to the preferred position. The entire immersed boundary can be connected to target points to model a nearly rigid structure, or a subset of the immersed boundary can be tethered, resulting in a more flexible structure as seen in Chapter 3.

The elastic deformations of the structure result in elastic body forces, $\boldsymbol{F_{elastic}}$. The immersed boundary may be thought of as being composed of fibers with a preferred curvature. Immersed boundary points may be connected by springs (to resist stretching and compression) and beams (to resist bending). $\boldsymbol{F_{elastic}}$ can then be written as:

$$\boldsymbol{F_{elastic}}(r,t) = \boldsymbol{F_{spring}}(r,t) + \boldsymbol{F_{beam}}(r,t), \qquad \text{Eq. 2.5}$$

$$\boldsymbol{F_{spring}}(r,t) = \frac{\partial}{\partial r} k_{spring}\left(\left|\frac{\partial \boldsymbol{X}(r,t)}{\partial r}\right| - 1\right)\hat{\boldsymbol{\tau}}(r,t), \qquad \text{Eq. 2.6}$$

$$\boldsymbol{F_{beam}}(r,t) = \frac{\partial^2}{\partial r^2} k_{beam} \left(\frac{\partial^2}{\partial r^2} (\boldsymbol{X}(r,t) - \boldsymbol{X_b}(r)) \right), \quad \text{Eq. 2.7}$$

where $\boldsymbol{F_{spring}}$ is the force from stretching and compression and $\boldsymbol{F_{beam}}$ is the force from bending, k_{spring} and k_{beam} are the stretching stiffness and the bending stiffness, respectively. $\hat{\boldsymbol{\tau}}(r,t)$ is the unit vector tangent to the structure, and $\boldsymbol{X_b}(r)$ is the preferred bending configuration of the structure. The material properties of the immersed boundary (how flexible it is) can be modified to resemble biological structures by changing k_{spring} and k_{beam}.

Once **F**(*r*,*t*) is calculated, the force needs to be spread from the structure to the surrounding fluid. The interaction equations between the fluid and the boundary are given by:

$$\boldsymbol{f}(\boldsymbol{x},t) = \int \boldsymbol{F}(r,t)\delta[\boldsymbol{x} - \boldsymbol{X}(r,t)]dr, \quad \text{Eq. 2.8}$$

$$\frac{\partial \boldsymbol{X}(r,t)}{\partial t} = \boldsymbol{u}(\boldsymbol{X}(r,t),t) = \int \boldsymbol{u}(\boldsymbol{x},t)\delta\big(\boldsymbol{x} - \boldsymbol{X}(r,t)\big)d\boldsymbol{x}, \quad \text{Eq. 2.9}$$

in which δ(**x**) is a two-dimensional Dirac delta function.

$$\delta_h(x) = \frac{1}{h^2}\phi\left(\frac{x}{h}\right)\phi\left(\frac{y}{h}\right), \quad \text{Eq. 2.10}$$

Where

$$\phi(r) = \begin{cases} \frac{1}{4}\left(1 + \cos\frac{\pi r}{2}\right) & |r| \leq 2 \\ 0 & otherwise \end{cases} \qquad \text{Eq. 2.11}$$

Eq. 2.8 and **Eq. 2.9** act to couple the Lagrangian and Eulerian variables. **Eq. 2.8** spreads force from the Lagrangian boundary to the Eulerian fluid grid. Using this force, the Navier-Stokes equations are solved to update the fluid information. Next, **Eq. 2.9** evaluates the fluid velocity in the Eulerian frame to interpolate the local fluid velocity at each boundary point in the Lagrangian frame. The boundary is then moved at the local fluid velocity, and this enforces the no-slip condition.

Details on the discretization used in these simulations have been described previously (Peskin and McQueen 1996, Peskin 2002, Griffith, Hornung et al. 2007, Miller and Peskin 2009). The general idea of this numerical method is as follows for each time step (see **Fig. 2.2**):

1. Calculate the force that the boundary applies to the fluid. In the following chapters, the forces are a result of resistance to bending, resistance to stretching, and forces applied by target points to drive the motion of the boundary in a preferred manner.
2. Spread the force from the Lagrangian grid describing the position of the boundaries to the Cartesian grid used to solve the fluid equations using a smoothed approximation of the Dirac delta-function (**Eq. 2.8**).
3. Solve the Navier-Stokes equations for the entire fluid domain.

4. Use the new velocity field to interpolate the local fluid velocity at the boundary using a smoothed Dirac delta-function. The boundary is moved at the local fluid velocity to enforce the no-slip condition (**Eq. 2.9**).
5. Advance to the next time step. These steps are repeated for each time step until the final simulation time is reached.

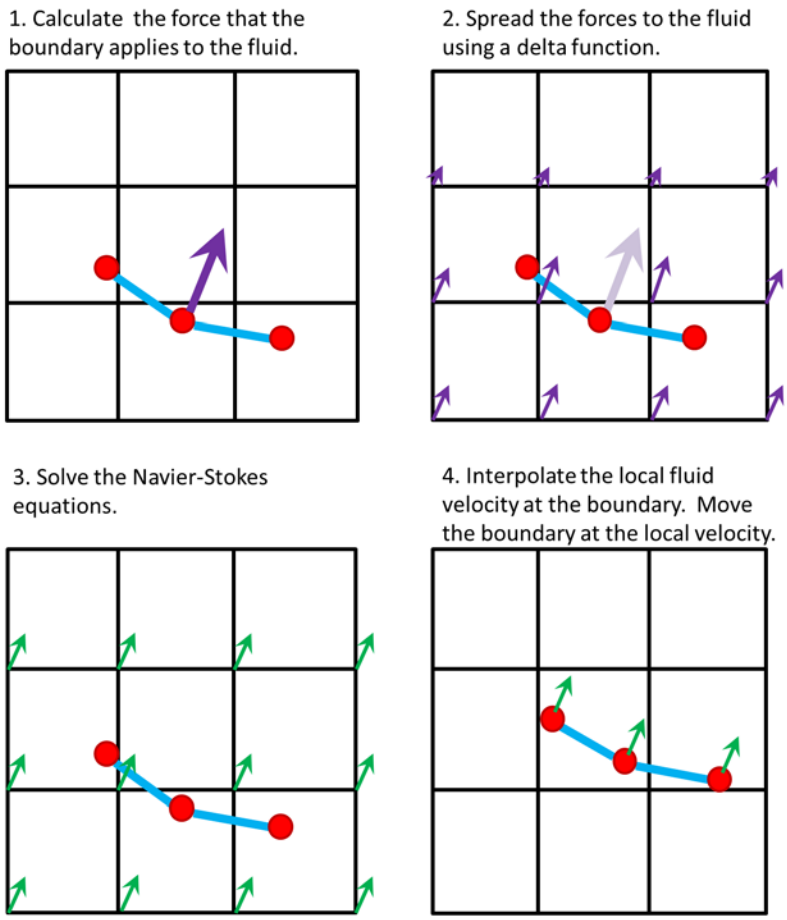

Figure 2.2. The basic steps of the immersed boundary method for each time step.

2.1.2 IBFE Method

The previous section described the classic immersed boundary method which I used to model a two-dimensional wing in Chapter 3. This method works well for simple geometries, where the structure can be modeled as a group of fibers that resist bending and stretching. However, it becomes more challenging to model complex structures, particularly in three-dimensions, using this method. Therefore, in Chapters 4 and 5, I use a hybrid finite difference / finite element version of the immersed boundary method.

As in the classical immersed boundary method, a finite difference formulation is used to solve the fluid equations in the IBFE method. The difference lies in how the structure is modeled: a finite element (FE) formulation is used to describe the boundary in IBFE, whereas a finite difference formulation is used to describe the boundary in the classical immersed boundary method. The IBFE method is described in detail in Griffith and Luo (2012). The formulation is:

$$\rho\left(\frac{\partial \boldsymbol{u}(\boldsymbol{x},t)}{\partial t}+\boldsymbol{u}(\boldsymbol{x},t)\cdot\nabla\boldsymbol{u}(\boldsymbol{x},t)\right)=-\nabla p(\boldsymbol{x},t)+\mu\Delta\boldsymbol{u}(\boldsymbol{x},t)+\boldsymbol{f}(\boldsymbol{x},t), \qquad \text{Eq. 2.12}$$

$$\nabla\cdot\boldsymbol{u}(\boldsymbol{x},t)=0 \qquad \text{Eq. 2.13}$$

$$\boldsymbol{f}(\boldsymbol{x},t)=\int_U \boldsymbol{F}(s,t)\delta[\boldsymbol{x}-\boldsymbol{\chi}(s,t)]ds, \qquad \text{Eq. 2.14}$$

$$\int_U \boldsymbol{F}(s,t)\cdot\boldsymbol{V}(s)ds=-\int_U \mathbb{P}^e(s,t):\nabla_s\boldsymbol{V}(s)ds, \qquad \forall\boldsymbol{V}(s), \qquad \text{Eq. 2.15}$$

$$\frac{\partial \boldsymbol{\chi}}{\partial t}(s,t) = \int_{\Omega} \boldsymbol{u}(\boldsymbol{x},t)\delta[\boldsymbol{x} - \boldsymbol{\chi}(s,t)]d\boldsymbol{x}, \qquad \text{Eq. 2.16}$$

$\boldsymbol{F}(s,t)$ is defined in terms of the first Piola-Kirchhoff solid stress tensor, $\mathbb{P}^e(s,t)$, using a weak formulation in which $\boldsymbol{V}(s)$ is an arbitrary Lagrangian test function. The elastic properties of the wing are described using a neo-Hookean material model. $\boldsymbol{\chi}(s,t)$ denotes the physical position of material point *s* at time *t*.

Eq. 2.12 and **Eq. 2.13** are the standard Eulerian incompressible Navier-Stokes equations. Similar to the classical IB method, **Eq. 2.14** and **Eq. 2.16** couple the Lagrangian and Eulerian variables. **Eq. 2.14** spreads force from the Lagrangian boundary to the Eulerian fluid, and **Eq. 2.16** interpolates the local fluid velocity at the boundary.

2.2 Software

2.2.1 IBAMR

The numerical studies described in Chapters 3, 4, and 5 used a distributed-memory parallel implementation of the immersed boundary method with Cartesian grid adaptive mesh refinement, called IBAMR (Griffith, Hornung et al. 2007). IBAMR was developed by Boyce Griffith and makes use of many high-quality open-source libraries, including SAMRAI, PETSc, libMesh, and hypre. IBAMR has been used to investigate a variety of biological fluid dynamics problems, including modelling spined cells (Nguyen, Karp-Boss et al. 2011), biofilm deformation in capillaries (Vo and Heys 2011), lamprey swimming (Tytell, Hsu et al. 2010), and heart valves (Griffith, Luo et al. 2009, Griffith 2012).

There are two major advantages of using IBAMR, when compared to other immersed boundary implementations. (1) The implementation can be run in parallel on multiple processors to decrease computation time. And, (2) the fluid grid is adaptive (**Fig. 2.3**). This means that

regions of fluid that contain the structure or regions of sufficiently high vorticity are discretized at higher levels of refinement, whereas regions far away from the boundary are discretized more coarsely. These features increase computational efficiency.

In the following chapters, the adaptive method used four grid levels to discretize the Eulerian equations with a refinement ratio of four between levels. Regions of fluid that contained the wing or vorticity above a threshold were discretized at the highest level of refinement. Unless otherwise specified, the effective resolution of the finest level of the grid corresponded to that of a uniform 512×512 discretization. The boundary conditions were set to no-slip ($\mathbf{u}=0$) on all sides of the computational domain.

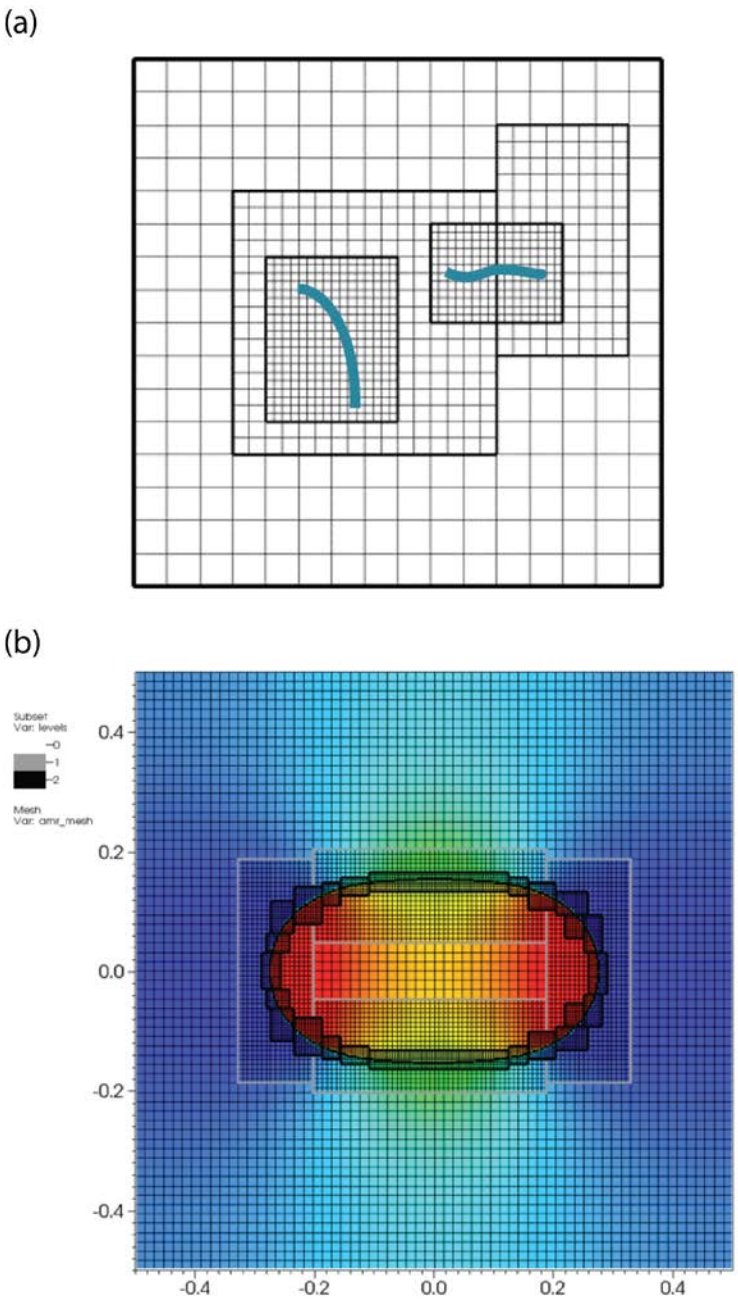

Figure 2.3. (a) In IBAMR, the fluid grid is adaptive. This means that regions of fluid that contain the structure or regions of vorticity are discretized at higher levels of refinement, whereas regions far away from the boundary are discretized more coarsely. (b) An example of IBAMR being used to model a rubber band in two-dimensions (Boyce Griffith, used with permission). The adaptive mesh is discretized at the highest level of refinement near the boundary.

2.2.2 Mesh generation

In Chapters 4 and 5, I use the IBFE method (Section 2.1.2) to model insect wings immersed in a viscous, incompressible fluid. In order to generate the finite element meshes for the immersed boundaries, I used a publicly available finite element mesh generator called Gmsh (Geuzaine and Remacle 2009). Gmsh is a free 3D finite element grid generator with a built-in CAD engine and post-processor.

2.2.3 Fluid visualization

All fluid visualization figures in the following chapters were generated by reading the output of IBAMR in VisIt (Childs 2013). VisIt is an open-source visualization and analysis tool which is able to visualize a wide variety of data including two- and three-dimensional structured, adaptive and unstructured meshes. Any quantitative calculations of fluid flow, such as fluid velocity, were also performed in VisIt.

2.2.4 Force analysis

I used MATLAB to analyze the forces in Chapters 3, 4, and 5.

CHAPTER 3: LIFT VS DRAG BASED MECHANISMS FOR VERTICAL FORCE PRODUCTION IN THE SMALLEST FLYING INSECTS[1]

3.1 Introduction

Previous work has shown that the flight kinematics and aerodynamics of the smallest insects may be significantly different than that of their larger counterparts (Weis-Fogh 1973, Wang 2000, Sunada, Takashima et al. 2002, Miller and Peskin 2004, Miller and Peskin 2005, Miller and Peskin 2009). Because of their small size and high wing beat frequency, detailed quantitative data on the wing kinematics of the smallest insects is not readily available (Sane 2003, Miller and Peskin 2009). As a result, there has been much debate and speculation about the flight strategies employed by these insects. Traditional lift-based strokes in the horizontal plane and less-traditional swimming-like strokes in the vertical plane have both been suggested. In this study, I used computational fluid dynamics to investigate whether lift- or drag-based mechanisms generate the most vertical force at $Re<100$ (the scale relevant to tiny insects).

I used the immersed boundary method to solve the fully coupled fluid-structure interaction problem of a flexible wing immersed in a 2D viscous fluid. I used this method to (*1*) compare three idealized 2D hovering kinematics: a drag-based stroke in the vertical plane, a lift-based stroke in the horizontal plane, and a hybrid stroke on a tilted plane; (*2*) compare faster and slower downstroke velocities; and (*3*) compare flexible and rigid wings. F_V and F_H were calculated as functions of time, and I determined how the structure of the vortex wake influenced the forces.

[1] This chapter previously appeared as an article in the Journal of Theoretical Biology. The original citation is as follows: SK Jones, R Laurenza, TL Hedrick, BG Griffith, LA Miller. "Lift vs. drag based mechanisms for vertical force production in the smallest flying insects." *Journal of Theoretical Biology*. 384 (2015) 105-120.

Net vertical force and the ratio of vertical force to total force generated by these strokes were compared over a range of *Re* from 1 to 200.

3.2 Methods

3.2.1 Prescribed wing kinematics.

To investigate the role of lift and drag in vertical force production, I considered three idealized stroke kinematics: a horizontal lift-based stroke, a vertical drag-based stroke, and a tilted hybrid stroke. The horizontal stroke approximates fruit fly kinematics (**Fig. 3.1a**), and lift is used to generate vertical force. The vertical stroke is a theoretical stroke (**Fig. 3.1b**), idealized to give the most possible drag-based vertical force and is similar to rowing with feathering on the upstroke. The hybrid stroke approximates dragonfly kinematics (**Fig. 3.1c**), and uses a combination of lift and drag to generate vertical force.

I explored the forces produced by these strokes with a numerical simulation of a moving elastic wing immersed in a viscous fluid. The simplified insect wing kinematics used in this chapter are similar to those used in previous computational studies to investigate hovering flight aerodynamics (Wang 2000, Wang 2004, Wang, Birch et al. 2004). A two-dimensional cross-section of the wing chord was used for all investigations, and I use the term “wing” in the remainder of the chapter to describe a wing’s cross section.

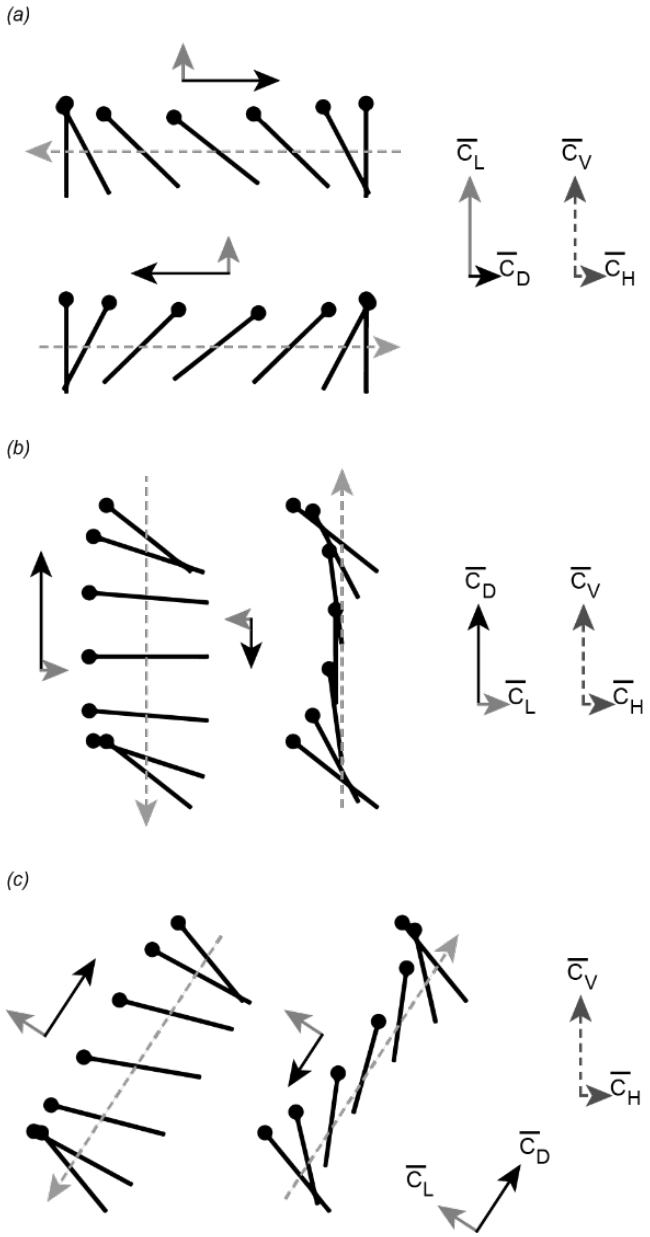

Figure 3.1. Idealized wing kinematics (sections through the chord of the wing). The closed circle represents the leading edge of the wing, and each half-stroke is shown separately. The solid black arrows indicate the direction and relative magnitude of dimensionless drag (C_D) during each half-stroke, and the solid grey arrows indicate the direction and relative magnitude of dimensionless lift (C_L). The solid axes on the right indicate the net C_D and C_L during a complete stroke. The direction of dimensionless vertical (C_V) and dimensionless horizontal (C_H) force always face the same direction with respect to the global frame (dashed arrows). (a) A horizontal, lift-based stroke (α_0=90°, β=0°) uses only C_L to produce C_V. (b) A vertical, drag-based stroke (α_0=45°, β=90°) uses only C_D to produce C_V. (c) A tilted, hybrid stroke ((α_0=60°, β=62.8°) uses both C_L and C_D to produce C_V.

The kinematics of the wing were defined as follows:

$$[x(t), y(t)] = \frac{A_0}{2}(1 + \cos(2\pi f t))[\cos(\beta), \sin(\beta)], \quad \text{Eq. 3.1}$$

$$\alpha(t) = \alpha_0 + B\sin(2\pi f t), \quad \text{Eq. 3.2}$$

in which $[x(t), y(t)]$ is the position of the center of the chord at time t, A_0 is the amplitude of translation, f is the frequency, β is the stroke plane angle, α is the chord orientation relative to β (i.e. the angle of attack), α_0 is the mean angle of attack, and B is the amplitude of rotation. In all computations, f=1, B=π/4 and A_0/c=2.5, where c is the chord length. By changing α_0 and β, I prescribe the motion of three idealized strokes: the horizontal stroke (α_0=90°, β=0°), the vertical stroke (α_0=45°, β=90°), and the tilted stroke (α_0=60°, β=62.8°).

3.2.2 Numerical method.

I used the immersed boundary method as described in Chapter 2 to model two-dimensional insect wings immersed in a viscous, incompressible fluid. The dimensionless equation describing a two-dimensional elastic wing immersed in a fluid can be written as follows:

$$\boldsymbol{F'} = k'_{beam}\frac{\partial^2}{\partial r^2}(\hat{\kappa}\hat{n}) - \frac{\partial}{\partial r}(T\hat{r}) \quad \text{Eq. 3.3}$$

Where ***F'*** is the dimensionless force applied to the wing, k'_{beam} is the dimensionless bending stiffness, $\hat{\kappa}$ is the curvature, $\hat{n}$ is the unit vector pointing normal to the wing, T is the tension, and $\hat{r}$ is the unit vector tangent to the wing. The dimensionless bending stiffness can be written as:

$$k'_{beam} = \frac{k_{beam}}{\rho U_{rms}^2 c^3} \quad \text{Eq. 3.4}$$

Where k_{beam} is the dimensional flexural stiffness and U_{rms} is the root mean square of the velocity of the center of the chord. In order to compare the forces from the computations, instantaneous forces experienced by the wing were non-dimensionalized by $0.5\rho U_{rms}^2 c$. C_V and C_H denote the vertical and horizontal force coefficients, respectively.

In this study, I used IBAMR (Griffith, Hornung et al. 2007) for all of the fluid dynamic simulations. The computational 2D wing was immersed in a fluid domain that was 20 chord lengths wide and high. The adaptive method used four grid levels to discretize the Eulerian equations with a refinement ratio of 4 between levels. Regions of fluid that contained the wing or vorticity above a threshold were discretized at the highest refinement. The effective resolution of the finest level of the grid corresponded to that of a uniform 512×512 discretization for $Re \leq 100$ and a uniform 1024×1024 discretization for $Re > 100$. The boundary conditions were set to no-slip (**u**=0) on all sides of the computational domain. Other simulation-specific numerical parameters are listed in **Table 3.1**.

Table 3.1. Numerical parameters.

Dimensionless parameter	**Value**
Chord length (c)	0.1
Domain length (L)	2
Finest Grid Refinement	512x512
Number of refinement levels	4
Refinement ratio	1:4
Time step (dt)	1.0e-6
Final simulation time	4
Spatial step size (dx)	L/512
Target stiffness (k'_{targ})	64
Spring stiffness (k'_{spring})	638
Beam stiffness (k'_{beam})	31

To investigate the role of lift and drag in tiny insect flight, I considered three idealized wing strokes for *Re* ranging from 1 to 200. *Re* is defined as

$$Re = \frac{\rho U_{max} c}{\mu} = \frac{\rho \pi f A_0 c^2}{\mu}, \qquad \text{Eq. 3.5}$$

in which U_{max} is the maximum velocity of the wing during a stroke. The *Re* was varied by changing μ while holding all other parameters constant.

The lift-to-drag ratio is one common metric of comparison used in studies of hovering. The lift-to-drag ratio is not an appropriate metric in this study, however, because I investigated wing kinematics that predominantly use drag to generate vertical force. Because I am studying very different types of strokes, comparing them in an equal way is challenging: C_V and C_H are zero at different points in the strokes, and net drag and net lift are zero for the horizontal and vertical strokes, respectively. However, our main motivation is to determine the amount of vertical force that can be generated compared to the total amount of force. For that reason, I chose to compare the three strokes using the ratio of net vertical force to net total force ($\overline{C_V}/\overline{C_T}$) over the third and fourth wing stroke. C_T determines the magnitude of the force that the muscles have to produce during flight. $\overline{C_V}/\overline{C_T}$ gives us a metric for how much of that force goes toward C_V.

3.2.3 Grid convergence study.

To test for spatial convergence, I compared four effective fine-grid resolutions: a uniform 256×256 discretization, a uniform 512×512 discretization, a uniform 1024×1024 discretization and a uniform 2048×2048 discretization. All four resolutions used the horizontal stroke kinematics described in **Fig. 3.1a** and were evaluated at *Re*=10, *Re*=100, and *Re*=200. I chose to complete the convergence study over a range of *Re* because more refined grids are often necessary at high *Re*, where the boundary layers around wings are smaller, and the error at the boundary is more

significant. The highest *Re* demonstrated the most error, because of the challenge of accurately resolving the boundary layers and the separation of vortices. C_V and C_H as functions of dimensionless time show small deviations between the grid resolutions during periods of wing acceleration and deceleration (**Fig. 3.2a-c**); however, the coefficients show overall good agreement.

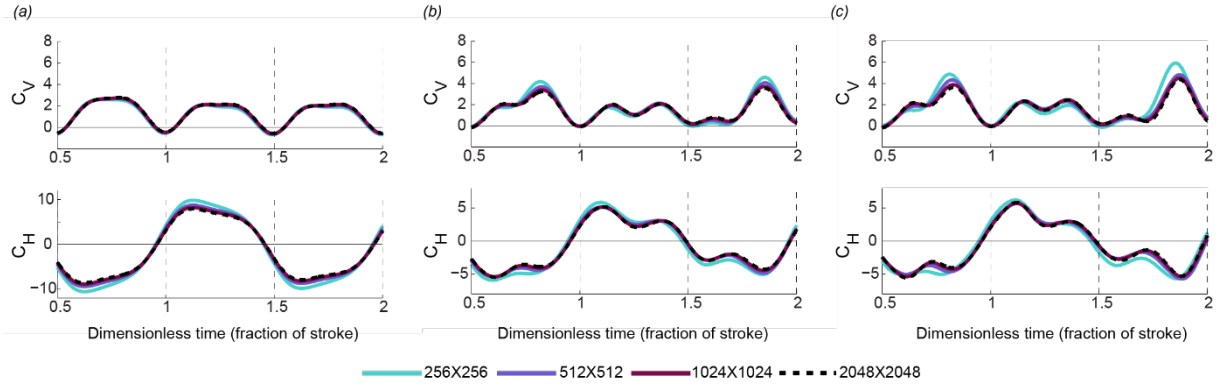

Figure 3.2. Refinement study displaying C_V and C_H as functions of dimensionless time for the horizontal stroke at (*a*) *Re*=10, (*b*) *Re*=100, and (c) *Re*=200. The legend denotes the mesh size of the finest grid near the wing and regions of vorticity. Effective 512×512 grid discretization was used for all other simulations with *Re*≤100, and 1024×1024 grid discretization was used for all other simulations with *Re*>100 in this chapter.

I compared the four grid resolutions by calculating the average percent difference in force between the selected grid and the next finest grid over the first two wingbeats (**Table 3.2**). For comparison, the average percent difference between different *Re* over two wing strokes for the horizontal stroke is shown in **Table 3.3**. Effective 512×512 grid discretization was used for all other simulations with *Re*≤100, and 1024×1024 grid discretization was used for all other simulations with *Re*>100 in this chapter. These grids were chosen because the average percent difference in force between the selected grid and the next finest grid is ≤5%.

Table 3.2. Average percent difference in forces over 2 wing strokes between different grid refinements at three different *Re*.

		% Difference	
	Grids	C_V	C_H
Re=200	256X256 vs. 512X512	19.9	19.4
	512X512 vs. 1024X1024	9.6	7.5
	1024X1024 vs. 2048X2048	4.4	3.4
Re=100	256X256 vs. 512X512	15.1	13.4
	512X512 vs. 1024X1024	5	4.1
	1024X1024 vs. 2048X2048	2.9	2.6
Re=10	256X256 vs. 512X512	6.3	10.8
	512X512 vs. 1024X1024	3	3.1
	1024X1024 vs. 2048X2048	1.2	1.8

Table 3.3. Average percent difference in forces over 2 wing strokes between different *Re* for the horizontal stroke on a 512X512 grid.

	% Difference	
	C_V	C_H
Re=100 vs. *Re*=10	94	53
Re=10 vs. *Re*=5	34	25
Re=5 vs. *Re*=1	67	55

3.2.4 Comparison to existing numerical data.

To check the method, I compared the model of the horizontal stroke to the numerical model given by Wang at *Re*=150 (Wang 2004). C_V and C_H as functions of time are shown (**Fig. 3.3**). Overall, there was good agreement between my IBAMR simulation and the numerical simulation described by Wang. The differences can probably be attributed to differences in the numerical models—our wing is a flexible two-dimensional plate, while Wang's is a rigid ellipse.

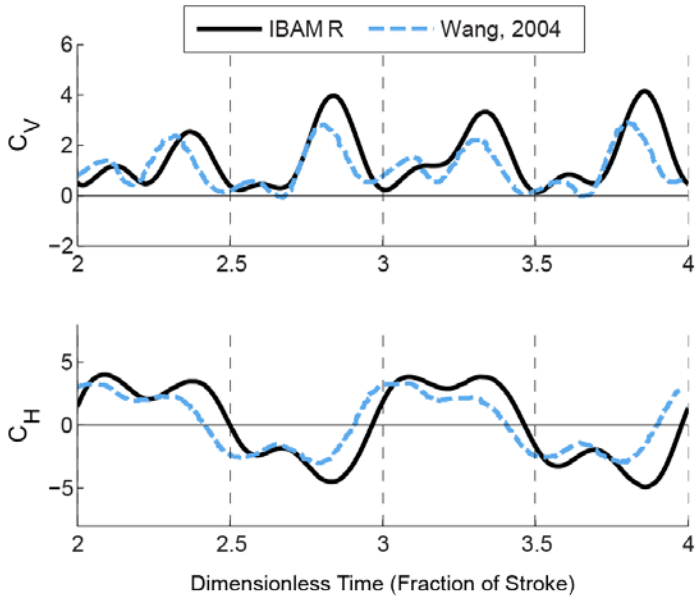

Figure 3.3. Comparison of IBAMR to an existing numerical method showing C_V and C_H as functions of dimensionless time. I compared the lift-based stroke (α_0=90°, β=0°, A_0/c=2.5, f=1, and B=$\pi/4$) at *Re*=150. Overall, there is good agreement between my simulation and the simulation described by Wang (28). Only the last two wing beats are shown.

3.3 Results

3.3.1 Comparison of three idealized hovering kinematics.

Simulations using the kinematics described in the **Fig 3.1** were performed for *Re* ranging from 1 to 200. Each simulation included four stroke cycles. Only the third and fourth stroke cycles that exhibited periodic behavior were used to obtain net aerodynamic forces.

C_V and C_H as functions of dimensionless time are shown for *Re* = 1,5,10, and 100 for the horizontal stroke (**Fig. 3.4**), the tilted stroke (**Fig. 3.5**) and the vertical stroke (**Fig. 3.6**). The shapes of the graphs of the horizontal and tilted strokes at *Re*=100 were similar to those obtained by Wang at *Re*=150 (Wang 2004), and the magnitude and trends for the horizontal stroke were consistent with those found by Miller and Peskin for a similar horizontal stroke (Miller and Peskin 2004). For all stroke types in this *Re* range, the magnitude of the instantaneous force coefficients decreased with increasing *Re*.

For the horizontal stroke (**Fig. 3.4**), C_V was positive for nearly the entire stroke, whereas for the tilted and vertical strokes (**Figs. 3.5-3.6**), C_V was positive during the downstroke and negative during the upstroke. In the tilted and vertical strokes, C_V peaked during mid-translation when the wing was moving most quickly. This was also the case for the horizontal stroke at low *Re*. At *Re*=100, C_V peaked during wing rotation and decreased during the translation phase for the horizontal stroke.

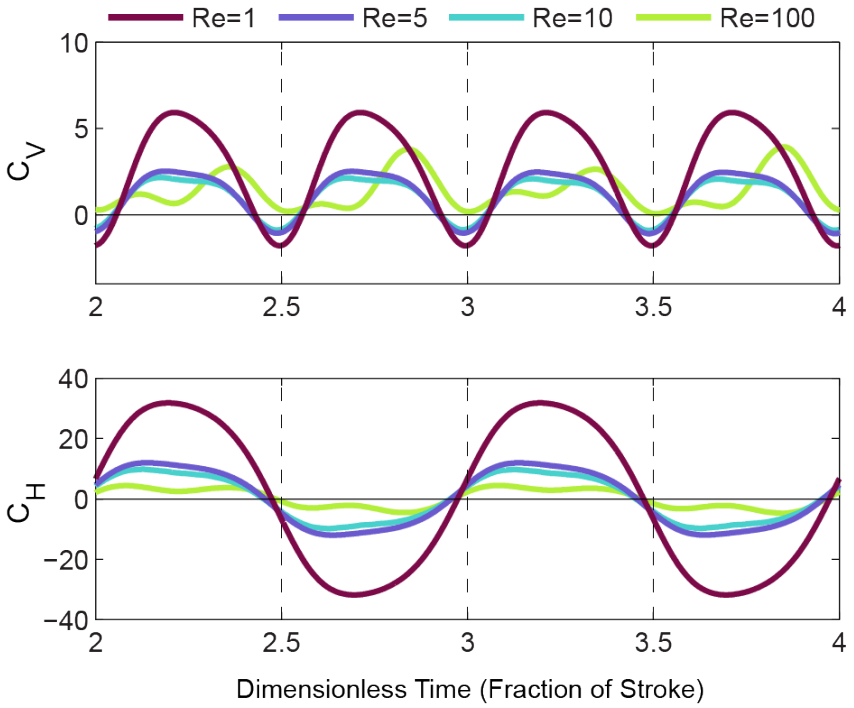

Figure 3.4. Instantaneous C_V and C_H as functions of dimensionless time for the horizontal lift-based stroke at *Re* 1, 5, 10 and 100 (α_0=90°, β=0°, A_0/c=2.5, f=1, and B=π/4). Only the last two wing beats are shown.

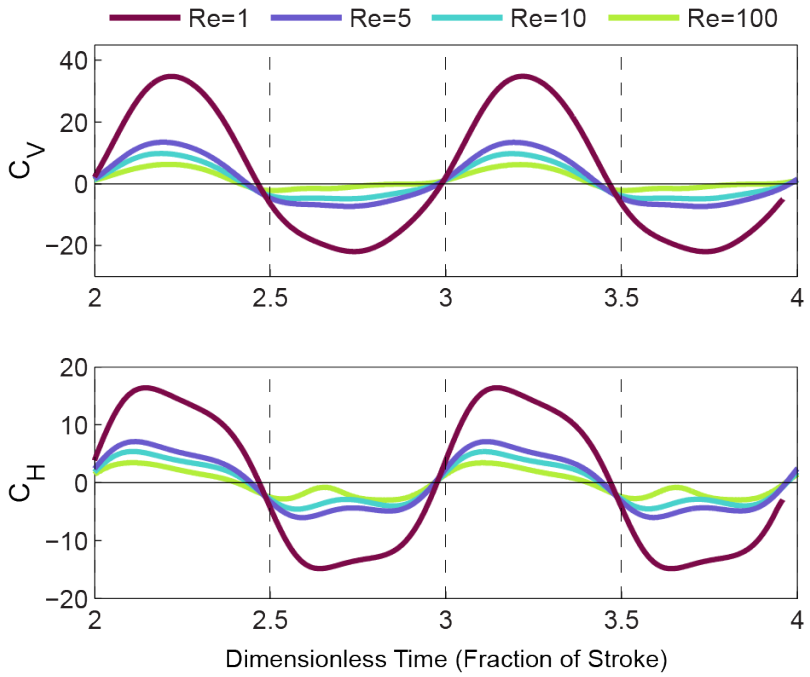

Figure 3.5. Instantaneous C_V and C_H as functions of time for the tilted hybrid stroke at *Re* 1, 5, 10 and 100 (α_0=60°, β=62.8°, A_0/c=2.5, f=1, and B=π/4).

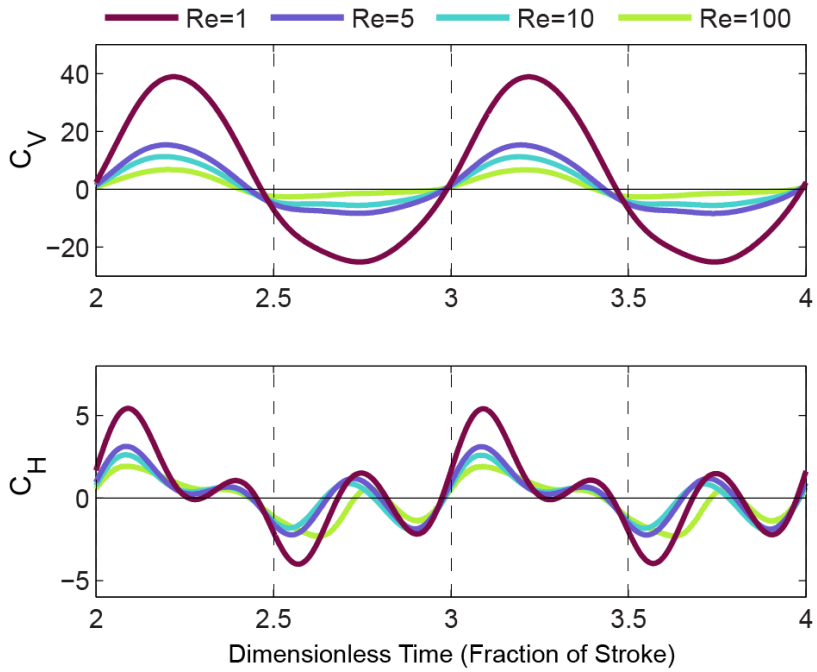

Figure 3.6. Instantaneous C_V and C_H as functions of time for the vertical drag-based stroke at *Re* 1, 5, 10 and 100 (α_0=45°, β=90°, A_0/c=2.5, f=1, and B=π/4).

For the horizontal stroke, peak C_H was much larger in magnitude than peak C_V, whereas for the tilted and vertical strokes peak C_V was larger in magnitude than peak C_H. For the horizontal and tilted strokes at lower *Re*, C_H peaked during translation. At *Re*=100, C_H increased during wing rotation and decreased during the translation phase of the stroke. For the vertical stroke, the peaks in C_H correspond to forces generated during wing rotation for all *Re* investigated. During translation, I expect C_H to be negligible due to the orientation of the wing during the vertical strokes.

The basis for some of these differences can be seen by comparing vorticity plots of the fluid flow around the wing at *Re*=10 and *Re*=100 (**Figs. 3.7-3.9**). For all strokes at *Re*=10 (**Figs. 3.7A, 3.8A, 3.9A**), leading edge vortices (LEV) and trailing edge vortices (TEV) formed during wing rotation at the beginning of downstroke (i). These vortices remained attached during downstroke (ii), and were shed at the end of downstroke during wing rotation (iii). New LEVs were formed during wing rotation and remained attached until the wing rotated at the beginning of the next downstroke (iv).

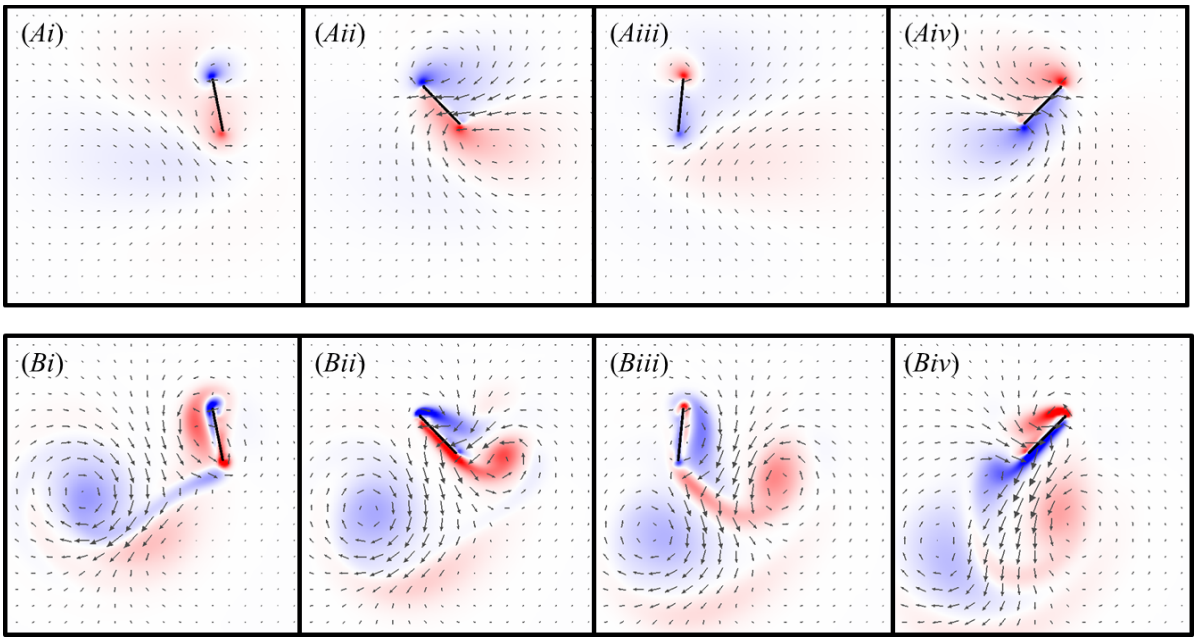

Figure 3.7. Vorticity plots of the horizontal stroke during the 4th wingbeat at (A) *Re*=10 and (B) *Re*=100, shown at (i) the beginning of downstroke, (ii) midway through downstroke, (iii) at the beginning of upstroke, and (iv) midway through upstroke. The vectors show the direction of flow and are scaled to the magnitude of the flow velocity. The colour map shows the vorticity of the fluid (min=-60 and max=60; red, counter clockwise rotation; blue, clockwise rotation).

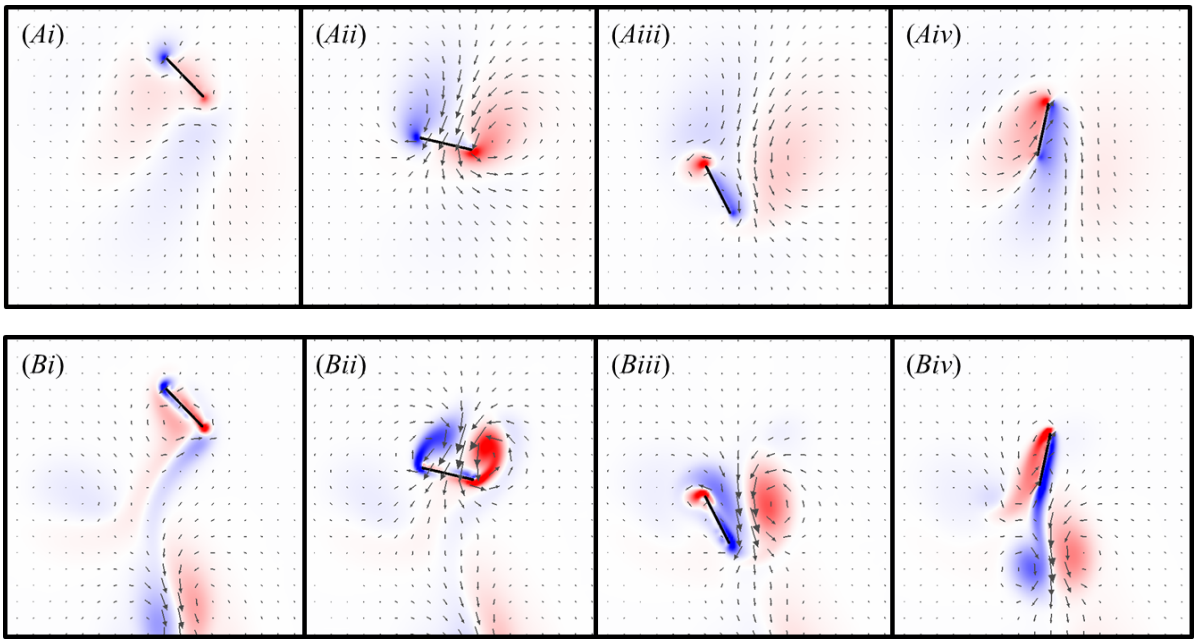

Figure 3.8. Vorticity plots of the tilted stroke during the 4th wingbeat at (A) *Re*=10 and (B) *Re*=100, shown at (i) the beginning of downstroke, (ii) midway through downstroke, (iii) at the beginning of upstroke, and (iv) midway through upstroke. The vectors show the direction of flow and are scaled to the magnitude of the flow velocity. The colour map shows the vorticity of the fluid (min=-60 and max=60; red, counter clockwise rotation; blue, clockwise rotation).

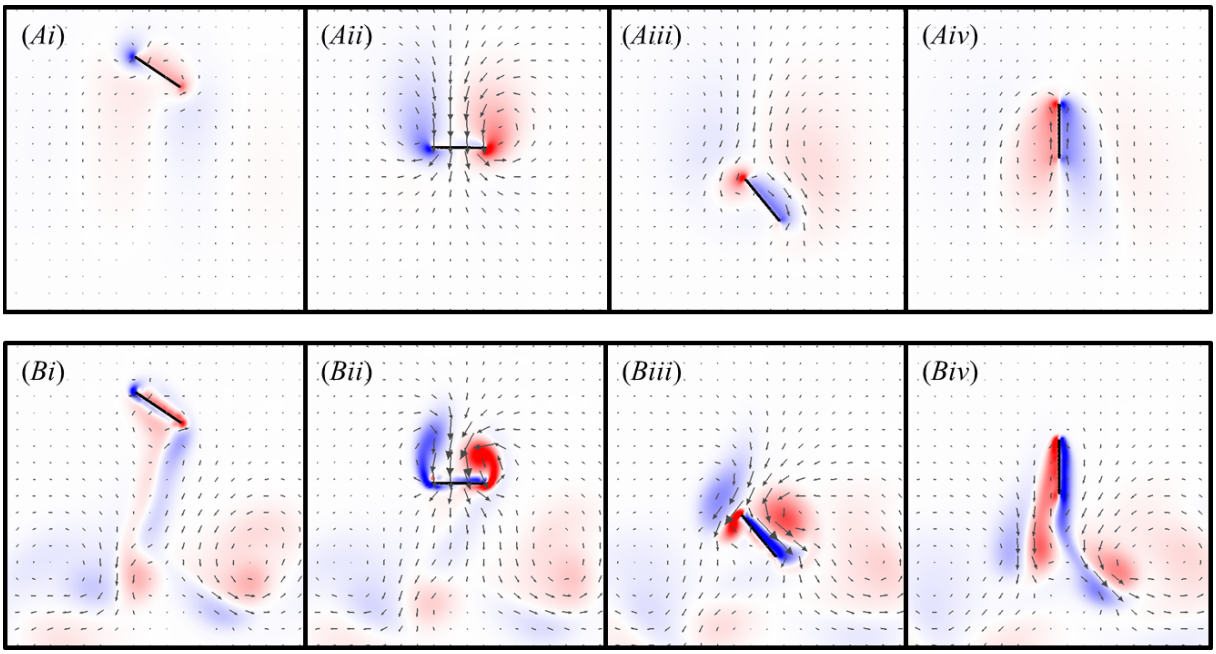

Figure 3.9. Vorticity plots of the vertical stroke during the 4th wingbeat at (A) *Re*=10 and (B) *Re*=100, shown at (i) the beginning of downstroke, (ii) midway through downstroke, (iii) at the beginning of upstroke, and (iv) midway through upstroke. The vectors show the direction of flow and are scaled to the magnitude of the flow velocity. The colour map shows the vorticity of the fluid (min=-60 and max=60; red, counter clockwise rotation; blue, clockwise rotation).

In contrast, vortex shedding played a significant role in force generation at *Re*=100. In the horizontal stroke (**Fig. 3.7B**), at the beginning of downstroke, a LEV and a TEV formed (i). Midway through downstroke, the LEV remained attached while the TEV was shed (ii). During wing rotation and the beginning of upstroke, the vortices were shed and a new LEV and TEV were formed as the wing travelled back through its wake (iii). Midway through upstroke, the LEV remained attached while the TEV was shed generating positive C_V (iv). The tilted stroke behaved similarly to the horizontal stroke at *Re*=100 (**Fig. 3.8B**). At the end of downstroke, the shed vortices travelled downward more quickly for the tilted stroke than for the horizontal stroke, which matched results reported by Wang (Wang 2004). In the vertical stroke at *Re*=100 (**Fig. 3.9B**), a larger LEV formed during wing rotation at the beginning of downstroke (i), and remained larger during downstroke (ii). During wing rotation and the beginning of upstroke, the vortices were shed (iii).

The shed vortices travelled downward more quickly for the vertical stroke than for the other strokes. During upstroke (iv), the wing was oriented parallel to the direction of movement, and vorticity was shed asymmetrically, generating some C_H.

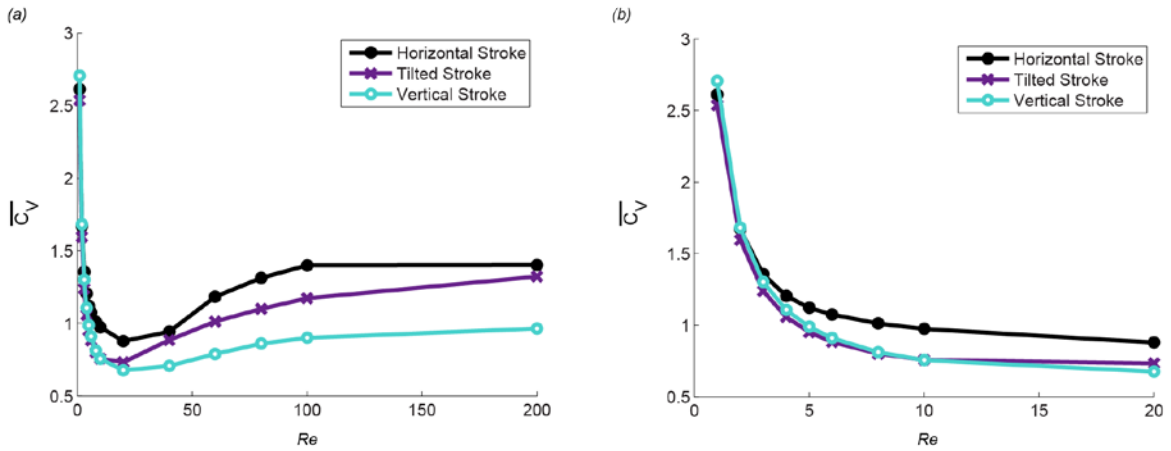

Figure 3.10. Net dimensionless vertical forces as functions of *Re*, shown for (a) all *Re* studied and (b) *Re* in the range of the smallest flying insects. The forces are averaged over the 3rd and 4th wing beats.

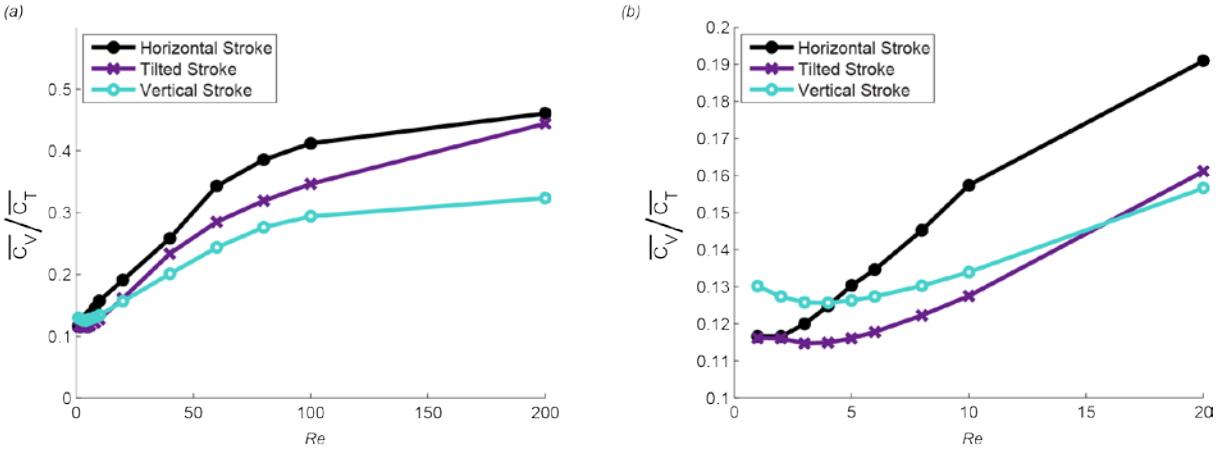

Figure 3.11. Net vertical force normalized by the total magnitude of force experienced by the wing ($\overline{C_V}/\overline{C_T}$) as a function of *Re*, shown for (a) all *Re* studied and (b) *Re* in the range of the smallest flying insects. The horizontal stroke had a higher $\overline{C_V}/\overline{C_T}$ for *Re*>5.

The three strokes were evaluated at *Re* ranging from 1 to 200. C_V was averaged over the 3rd and 4th wingbeats and plotted as functions of *Re* for each of the types of stroke (**Fig. 3.10**).

Similarly, the $\overline{C_V}/\overline{C_T}$ as functions of *Re* are shown in **Fig. 3.11**. The horizontal stroke generated more $\overline{C_V}$ than the other strokes at *Re* > 2, whereas the vertical stroke generated the most $\overline{C_V}$ at *Re* < 2. The vertical stroke generated the least $\overline{C_V}$ at *Re* > 10. The vertical stroke had the greatest $\overline{C_V}/\overline{C_T}$ at *Re*<5; however, it had the lowest $\overline{C_V}/\overline{C_T}$ at *Re*>20. The horizontal stroke had the greatest $\overline{C_V}/\overline{C_T}$ at *Re*>5. $\overline{C_V}/\overline{C_T}$ increased with *Re*, and at *Re*>20 $\overline{C_V}$ increased with *Re* for all stroke types. Both $\overline{C_V}$ and $\overline{C_V}/\overline{C_T}$ began to plateau at *Re*>100 as viscous effects become less significant. It is worthwhile to note that these results include unsteady effects, and much of the C_V for the lower *Re* was generated during wing rotation at the end of each stroke. There was a large increase in $\overline{C_V}$ as *Re* decreased below 10. This matches results of Miller and Peskin: dimensionless drag remained relatively constant with decreasing *Re*, then increased rapidly for *Re*<10 (Miller and Peskin 2004). This likely happens because at these low *Re* most C_V is generated as a result of shearing the viscous fluid during wing rotation.

3.3.2 Faster downstroke.

Bennet suggested that a faster downstroke velocity would enhance C_V produced by a drag-based mechanism (Bennet 1973). Despite observed insects having faster upstrokes rather than downstrokes (**Table 3.4**), I wanted to investigate what effect a faster downstroke would have on C_V produced by tiny insects using a drag-based mechanism.

Table 3.4 Ratio of downstroke velocity to upstroke velocity.

Insect	**Velocity Ratio (η)**
Encarsia formosa (Weis-Fogh 1973)	0.75
Thrips (Santhanakrishnan, Robinson et al. 2014)	0.88
Fruit fly (Zanker 1990)	0.6
Honeybee (Osborne 1951)	0.77
House fly (Osborne 1951)	0.67

I evaluated the vertical stroke at different ratios (η) of the downstroke velocity to the upstroke velocity. Here,

$$\eta = \frac{T_{upstroke}}{T_{downstroke}},$$

where $T_{downstroke}$ and $T_{upstroke}$ are the times to complete downstroke and upstroke, respectively. *Re* was calculated as before.

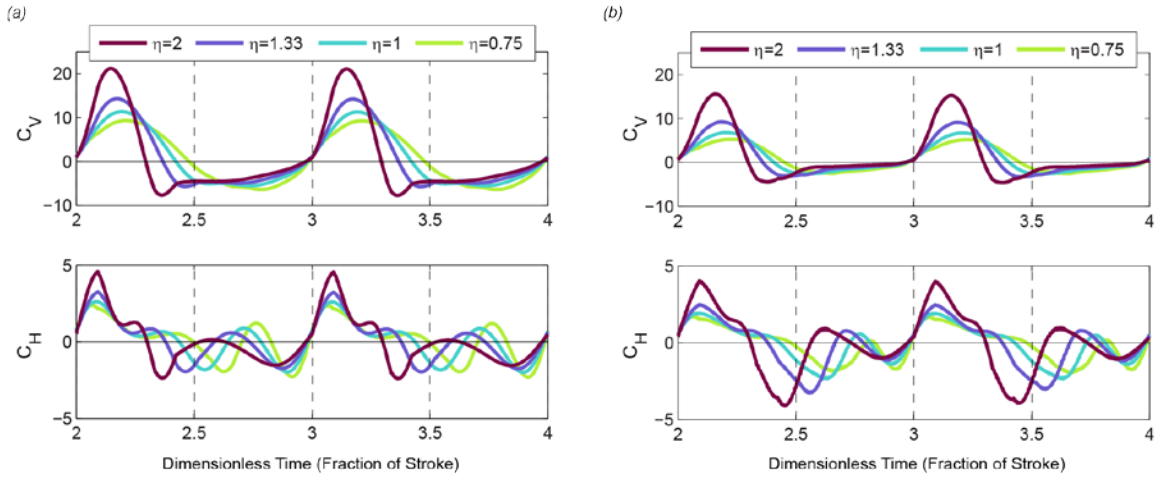

Figure 3.12. Instantaneous C_V and C_H as functions of time for the vertical drag-based stroke with different ratios of downstroke and upstroke velocity (η) for (a) *Re*=10 and (b) *Re*=100.

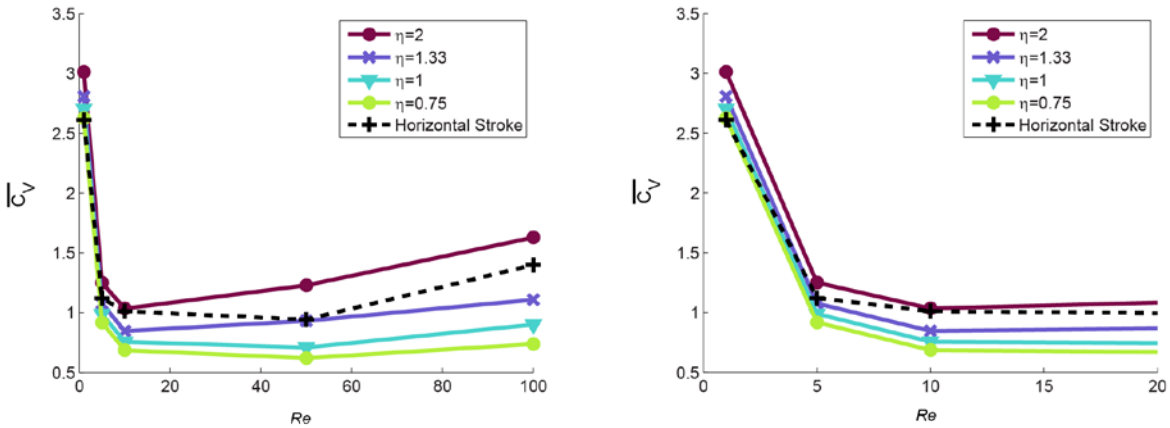

Figure 3.13. Net dimensionless vertical forces as functions of *Re* for different ratios of downstroke velocity to upstroke velocity (η) shown for the vertical stroke at (a) all *Re* studied and (b) *Re* in the range of the smallest flying insects. Greater ratios produce larger $\overline{C_V}$. The symmetric (η =1) horizontal stroke is shown for reference as the dashed line.

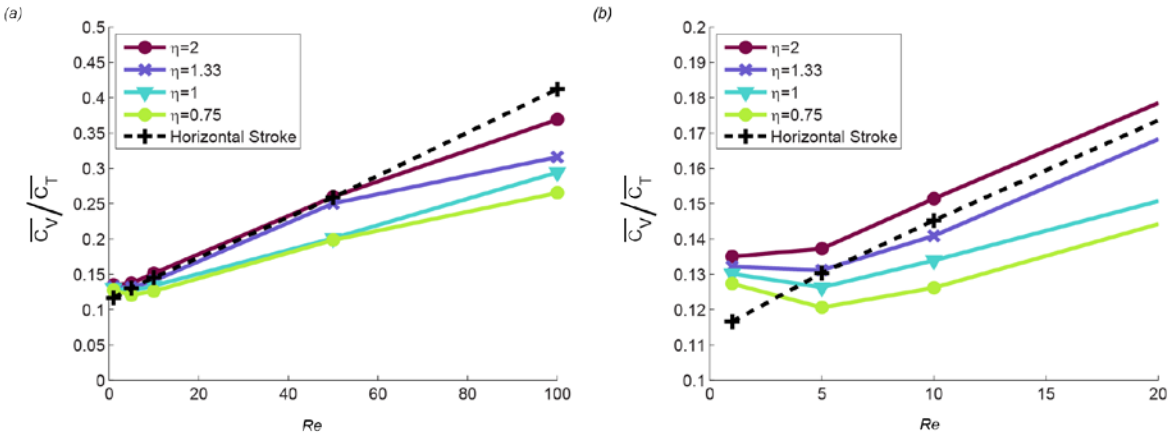

Figure 3.14. $\overline{C_V}/\overline{C_T}$ as a function of *Re* for different ratios of downstroke velocity to upstroke velocity (η) shown for (a) all *Re* studied and (b) *Re* in the range of the smallest flying insects. Greater ratios have higher $\overline{C_V}/\overline{C_T}$. The symmetric ($\eta$=1) horizontal, lift-based stroke is shown for reference as the dashed line.

C_V was evaluated for η ranging from 0.75 to 2, at *Re* from 1 to 100. C_V and C_H as functions of dimensionless time are shown for all η at *Re*=10 and *Re*=100 (**Fig. 3.12a&b**). The magnitude of C_V during downstroke increased with increasing η, however the duration of the downstroke decreased. Similarly, the magnitude of C_V during upstroke decreased with increasing η; however, the duration of the upstroke increased. In all *Re* investigated, $\overline{C_V}$ increased with η, and the η=2 case had a greater $\overline{C_V}$ than the corresponding symmetric horizontal stroke (**Fig. 3.13**). Similarly, $\overline{C_V}/\overline{C_T}$ increased with η; however, at higher *Re* the horizontal stroke had a greater $\overline{C_V}/\overline{C_T}$ than all vertical strokes regardless of η (**Fig. 3.14**). At *Re*≤10, the η=2 case had a greater $\overline{C_V}/\overline{C_T}$ than the horizontal stroke. The increase in $\overline{C_V}$ and $\overline{C_V}/\overline{C_T}$ was *Re* dependent—the magnitude of the effect decreased with decreasing *Re*. At the *Re* of the smallest insects, the increase in performance was small. Interestingly, *Encarsia formosa* has a faster upstroke than downstroke with η=0.75 (Weis-Fogh 1973). A vertical stroke with η=0.75 had a lower $\overline{C_V}$ and $\overline{C_V}/\overline{C_T}$ than η=1.

The aerodynamic basis for these changes in $\overline{C_V}$ and $\overline{C_V}/\overline{C_T}$ can be seen by comparing the vorticity field when η=1 (**Fig. 3.9**) and η=2 (**Fig. 3.15**). When η=2 at *Re*=10, larger vortices were

formed during downstroke (**Fig 3.15Aii**), and consequently larger vortices were shed during wing rotation at the end of downstroke (**Fig. 3.15Aiii**). The effect of η was even more pronounced at larger *Re*. When η=2 at *Re*=100, larger vortices were also formed during downstroke (**Fig. 3.15Bii**) and shed during wing rotation (**Fig. 3.15Biii**). The shed vortices travelled downward twice as fast when η=2 (**Fig. 3.15Biv**).

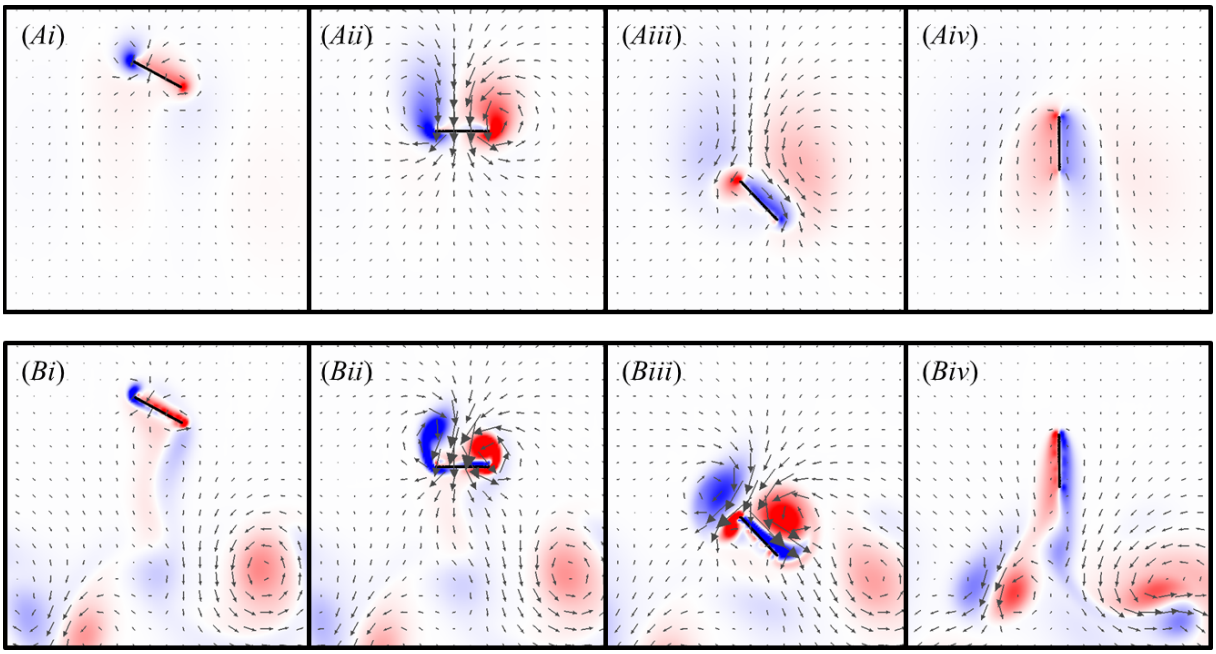

Figure 3.15. Vorticity plots of the vertical stroke with a downstroke that is twice as fast as the upstroke (η=2) during the 4th wingbeat at (A) *Re*=10 and (B) *Re*=100, shown at (i) the beginning of downstroke, (ii) midway through downstroke, (iii) at the beginning of upstroke, and (iv) midway through upstroke. The vectors show the direction of flow and are scaled to the magnitude of the flow velocity. The colour map shows the vorticity of the fluid (min=-60 and max=60; red, counter clockwise rotation; blue, clockwise rotation).

3.3.3 Flexible wings.

I also expect that flexibility will play a role in wing performance. Flexibility of biological structures has been demonstrated to reduce drag in a number of studies (Koehl 1984, Vogel 1989, Etnier and Vogel 2000, Alben, Shelley et al. 2002, Alben, Shelley et al. 2004, Miller, Santhanakrishnan et al. 2012). To compare a flexible wing to the rigid case, I selected k'_{beam}=31.

I chose this value to represent a case in which deformations are very small but some bending does occur (**Fig. 3.16**). The vertical stroke experienced bending of ~10° during mid-downstroke at *Re*=10. In the flexible wing, the leading edge of the wing (1/5 of the chord length) remained rigid, whereas the trailing edge of the wing was flexible and allowed to bend as it interacted with the fluid. This represents a simplified way of modelling a stiffer leading edge and flexible trailing edge.

Figure 3.16. Plots of the configuration of a rigid wing (gray line) and a flexible wing (black line) engaged in the vertical stroke at *Re*=10, shown at (A) the beginning of downstroke, (B) midway through downstroke, (C) at the beginning of upstroke, and (D) midway through upstroke. The greatest deformation among all of the strokes analyzed occurs during the middle of downstroke for the vertical stroke.

Vorticity fields of the three strokes with flexible wings at *Re*=10 and *Re*=100 (**Figs. 3.17-3.19**) can be compared to the rigid cases (**Figs. 3.7-3.9**). The flexible wing generated weaker vortices than the rigid wing in all wing strokes. The vortices were also shed more quickly during with rotation in the flexible wing cases.

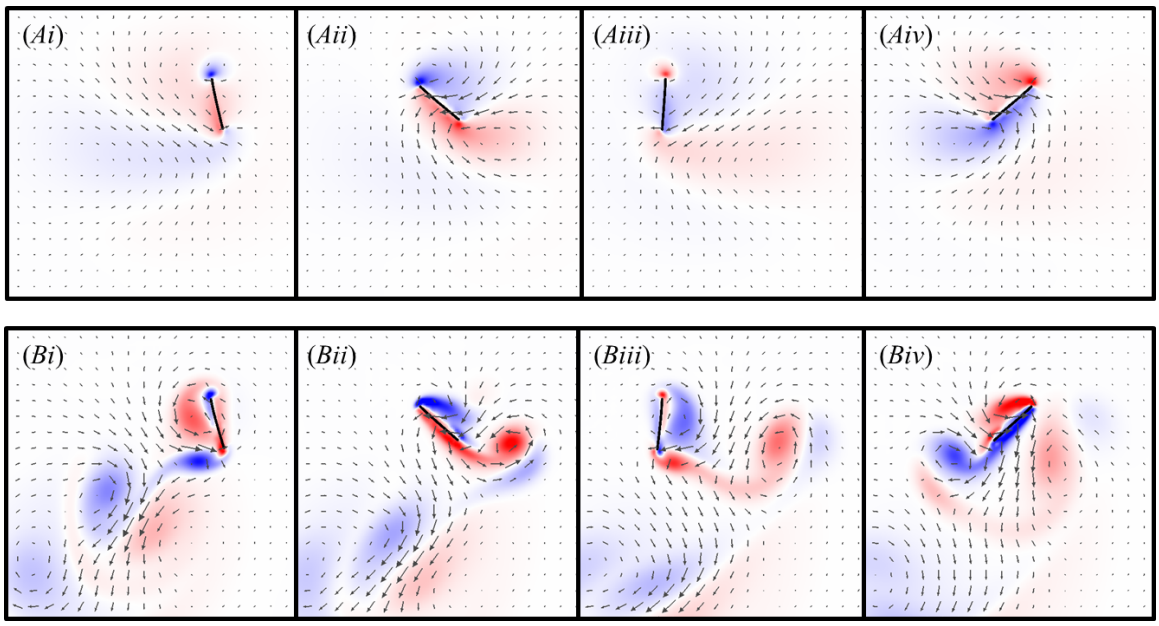

Figure 3.17. Vorticity plots of the horizontal stroke with a flexible wing during the 4th wingbeat at (A) *Re*=10 and (B) *Re*=100, shown at (i) the beginning of downstroke, (ii) midway through downstroke, (iii) at the beginning of upstroke, and (iv) midway through upstroke. The vectors show the direction of flow and are scaled to the magnitude of the flow velocity. The colour map shows the vorticity of the fluid (min=-60 and max=60; red, counter clockwise rotation; blue, clockwise rotation).

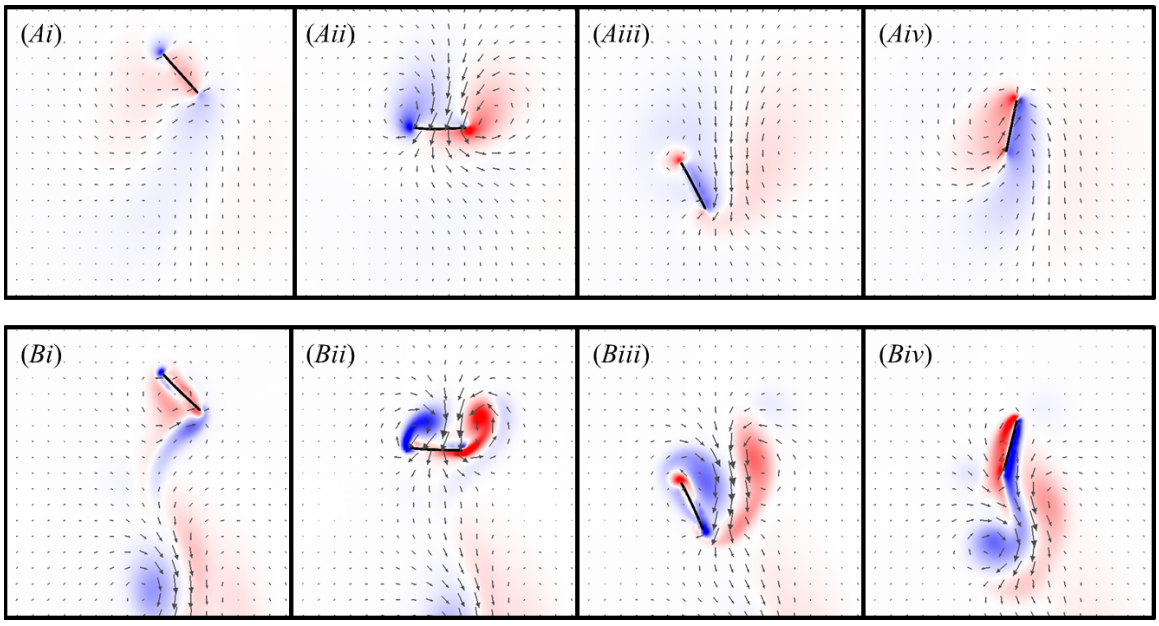

Figure 3.18. Vorticity plots of the tilted stroke with a flexible wing during the 4th wingbeat at (A) *Re*=10 and (B) *Re*=100, shown at (i) the beginning of downstroke, (ii) midway through downstroke, (iii) at the beginning of upstroke, and (iv) midway through upstroke. The vectors show the direction of flow and are scaled to the magnitude of the flow velocity. The colour map shows the vorticity of the fluid (min=-60 and max=60; red, counter clockwise rotation; blue, clockwise rotation).

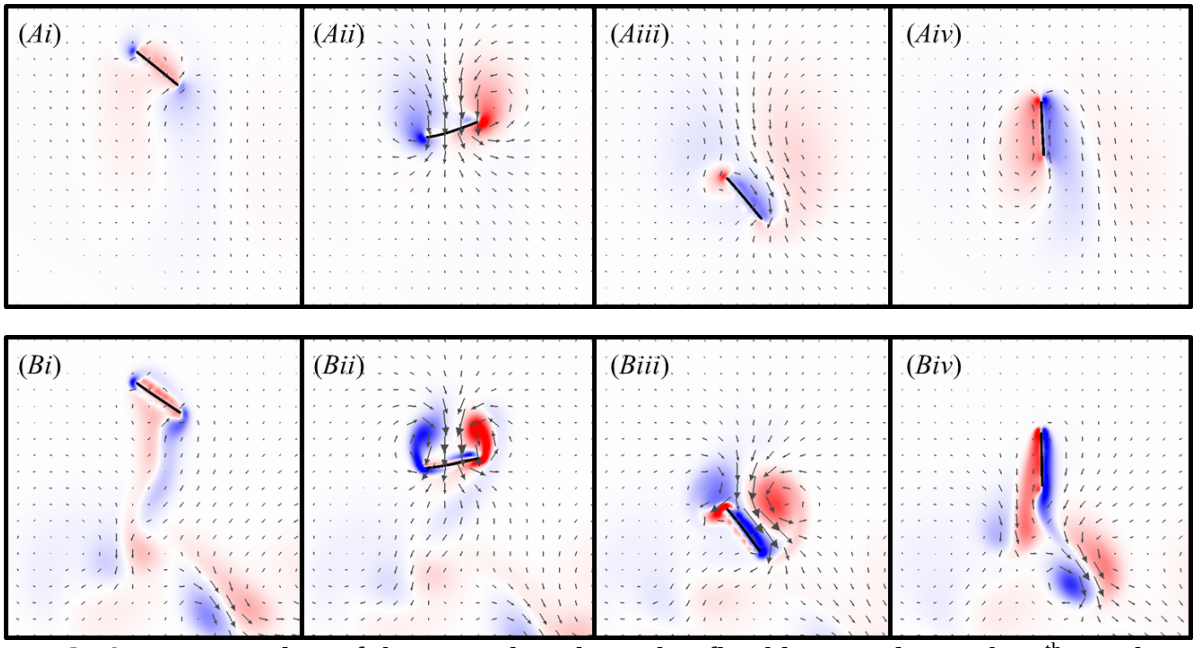

Figure 3.19. Vorticity plots of the vertical stroke with a flexible wing during the 4th wingbeat at (A) *Re*=10 and (B) *Re*=100, shown at (i) the beginning of downstroke, (ii) midway through downstroke, (iii) at the beginning of upstroke, and (iv) midway through upstroke. The vectors show the direction of flow and are scaled to the magnitude of the flow velocity. The colour map shows the vorticity of the fluid (min=-60 and max=60; red, counter clockwise rotation; blue, clockwise rotation).

C_V and C_H as functions of dimensionless time are shown for the flexible and rigid case for all stroke types at *Re*=10 and *Re*=100 (**Fig. 3.20**). In most cases, the rigid and flexible wings behaved similarly. For the horizontal stroke (**Fig. 3.20a**), there was a larger peak in C_V following wing rotation at the beginning of downstroke and upstroke in the flexible wing. During wing rotation, the wing bends slightly, and the small increase in C_V was likely a result of the wing returning to a nearly straight configuration during translation.

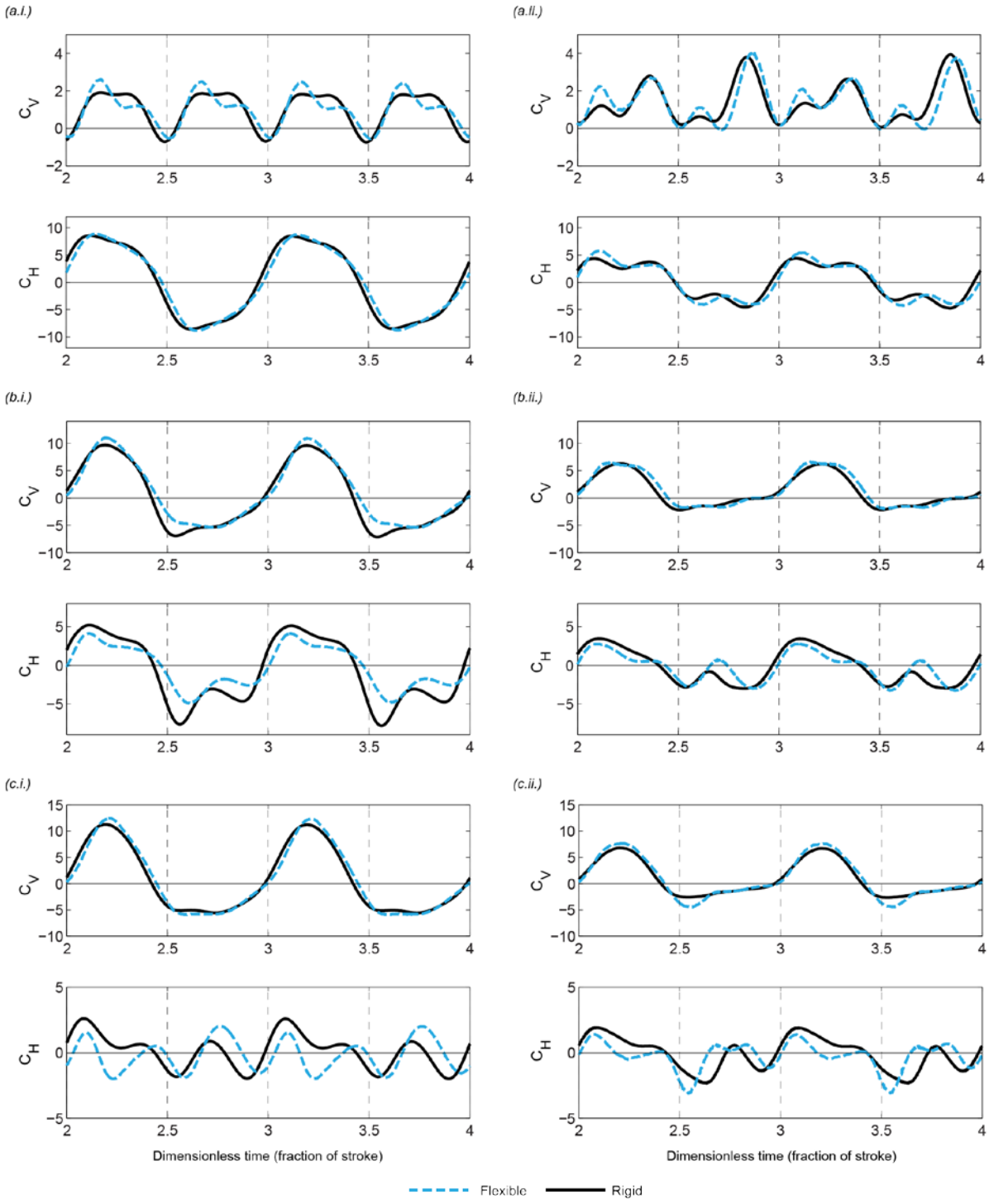

Figure 3.20. Instantaneous C_V and C_H as functions of dimensionless time for flexible wing and rigid wings at (i) *Re*=10 and (ii) *Re*=100, shown for (a) the horizontal stroke, (b) the titled stroke, and (c) the vertical stroke.

The flexible and rigid tilted strokes (**Fig. 3.20b**) had similar C_V during downstroke, but the magnitude of the negative C_V during wing rotation and upstroke was smaller for the flexible wing. This is likely due to the flexible wing encountering a smaller wake during the upstroke than the rigid wing. The magnitude of C_H was smaller during both upstroke and downstroke for the flexible wing as a result of drag reduction in the flexible wing. C_V was similar for the flexible and rigid vertical strokes (**Fig. 3.20c**); however, the plots of C_H are quite different—likely a result of variations in how vortices are shed for the two cases and oscillations in the flexible wing following wing rotation.

There was little difference in $\overline{C_V}$ for the horizontal stroke (**Fig. 3.21a**), but $\overline{C_V}$ was greater for the flexible wing at all *Re* for both the tilted and vertical strokes (**Fig. 3.21b&c**). The greatest increase in $\overline{C_V}$ was seen for the tilted stroke. There was very little difference in $\overline{C_V}/\overline{C_T}$ for flexible and rigid wings using either the horizontal or vertical strokes. The tilted stroke with the flexible wing had a ~20% greater $\overline{C_V}/\overline{C_T}$ than the rigid wing (**Fig. 3.22**). The increase in $\overline{C_V}/\overline{C_T}$ for the flexible tilted stroke resulted from decrease in negative C_V during upstroke and the decrease in the magnitude of C_H. The magnitude of this improved $\overline{C_V}/\overline{C_T}$ increased with *Re*.

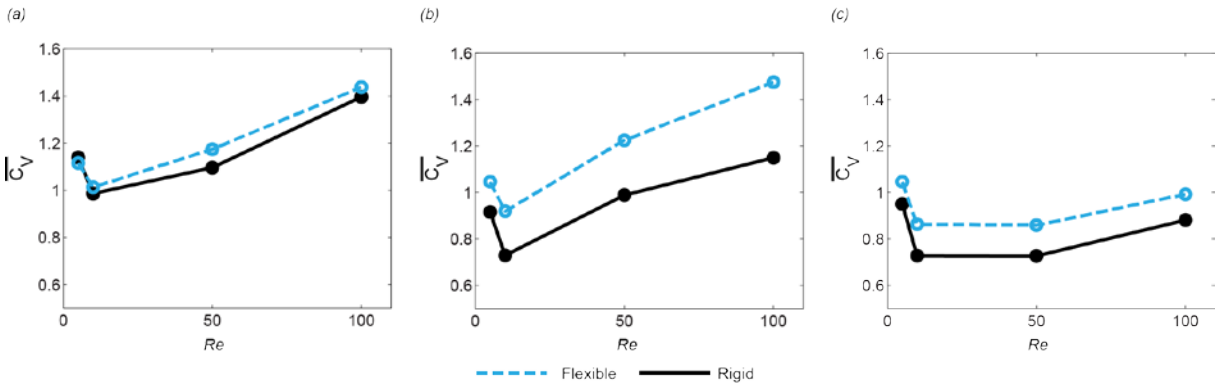

Figure 3.21. Net dimensionless vertical forces as functions of *Re* for the flexible and rigid wings, shown for (a) the horizontal stroke, (b) the titled stroke, and (c) the vertical stroke.

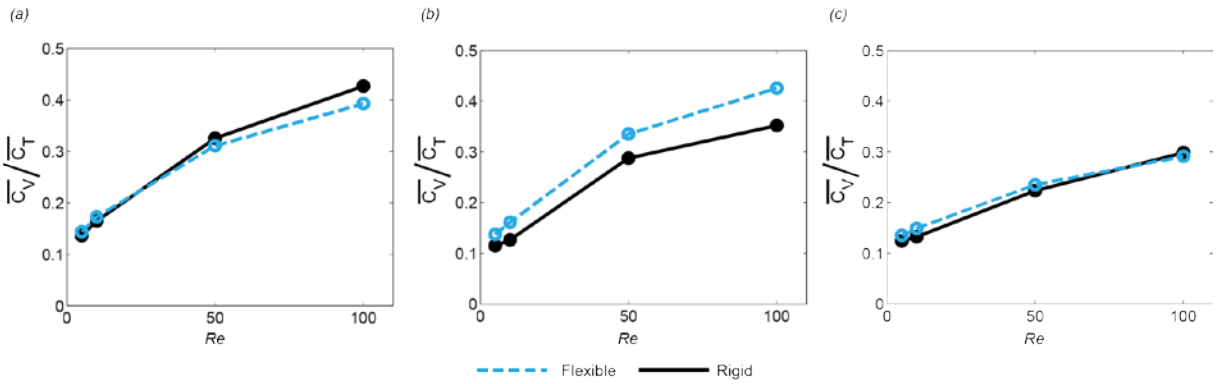

Figure 3.22. $\overline{C_V}/\overline{C_T}$ as a function of *Re* for the flexible and rigid wing, shown for (a) the horizontal stroke, (b) the titled stroke, and (c) the vertical stroke.

3.4. Discussion

The results of this study suggest that: (*1*) lift-based mechanisms produce more C_V than drag-based mechanisms at $Re > 2$, whereas drag-based mechanisms produce more C_V than lift-based mechanisms at $Re < 2$; (*2*) lift-based mechanisms have greater $\overline{C_V}/\overline{C_T}$ than drag-based mechanisms at $Re > 5$, while drag-based mechanisms have greater $\overline{C_V}/\overline{C_T}$ than lift-based mechanisms at $Re < 5$; (*3*) a faster downstroke increases C_V and $\overline{C_V}/\overline{C_T}$ of a drag-based mechanism, although this effect is modest at lower *Re*; and (*4*) flexibility has little effect on a lift-based mechanism, although flexibility increases C_V in a drag-based mechanism and increases both C_V and $\overline{C_V}/\overline{C_T}$ in a stroke that uses both drag- and lift-based mechanisms. At greater *Re*, a lift-based strategy produces more C_V and has a greater $\overline{C_V}/\overline{C_T}$ than a drag-based strategy; however, at the *Re* pertinent to small insect hovering there is little difference in performance between the two strategies. According to the results of this study, a drag-based mechanism of flight would have a greater $\overline{C_V}/\overline{C_T}$ than a lift-based mechanism for insects at $Re<5$, although I am unaware of flapping insect flight at $Re <5$.

Wang suggested that to benefit from the large drag found in symmetric horizontal strokes, an insect could tilt the downstroke by ~56° so that the net force points vertically up (Wang 2004). Then the wing could return to the starting position with a zero angle of attack during the upstroke. Rather than tilting the horizontal stroke as Wang suggested, I created a theoretical stroke in the vertical plane. This stroke also has a net force that points vertically up during the downstroke, and a wing that returns to the starting position with a zero angle of attack during the upstroke. Assuming that the upstroke contributes almost no force, Wang estimated that the average $\overline{C_V}$ would be 0.99 for a complete stroke at *Re*=150. Our results indicate that $\overline{C_V}$ would be ~0.9 at *Re*=150. Our results are slightly lower than Wang's because our model does not assume zero force during the upstroke and the upstroke does contribute some negative C_V.

Bennet (1973) suggested that a faster downstroke velocity would enhance $\overline{C_V}$ produced by a drag-based mechanism. Observed insects to-date actually have downstrokes that are slower than their upstroke. Since little is known about the flapping kinematics of the smallest insects, I wanted to investigate the effectiveness of a drag-based stroke with faster downstrokes. The results indicate that a faster downstroke does increase $\overline{C_V}$ and $\overline{C_V}/\overline{C_T}$ in a vertical stroke. The increase in performance with increasing downstroke velocity is dependent on *Re*. The magnitude of the effect decreases as *Re* decreases. At the *Re* of the smallest flying insects, a vertical stroke with the downstroke twice as fast as the upstroke actually slightly outperforms a lift-based horizontal stroke; however, the increase in performance is modest. Interestingly, *Encarsia formosa* has been observed to have a faster upstroke than downstroke with η=0.75 (Weis-Fogh 1973). The results suggest that an insect performing a vertical stroke with η=0.75 would perform worse than insects with larger η. It is likely that observed insects have slower downstrokes because they are not engaged in a drag-based vertical stroke. I did not investigate the effect of faster or slower

downstrokes on lift-based kinematics, but it has been suggested that the upstroke is relatively fast so as to minimize the loss of lift (Grimaldi and Engel 2005).

Flexibility has been demonstrated to play an important role in drag reduction in a number of studies (Alben, Shelley et al. 2002, Miller and Peskin 2004, Miller and Peskin 2009, Miller, Santhanakrishnan et al. 2012). Consequently, I expected that flexibility would impact wing performance. I compared the three stroke types using both a flexible and a rigid wing (**Figs. 3.21 and 3.22**). There was little difference between the flexible and rigid wings for the lift-based horizontal stroke. However, $\overline{C_V}$ increased for the flexible wing case for the tilted and vertical strokes, and the $\overline{C_V}/\overline{C_T}$ increased for the flexible wing case for the tilted stroke. The greatest increase in $\overline{C_V}$ and $\overline{C_V}/\overline{C_T}$ was observed for the tilted stroke (**Fig. 3.22b**). However, even with the increase in performance with added flexibility, the tilted and vertical stroke still had lower forces and $\overline{C_V}/\overline{C_T}$ than the horizontal stroke at *Re* pertinent to the smallest insects.

The results of this study suggest it is possible that a small insect could use a drag-based strategy to produce as much $\overline{C_V}$ as a lift-based strategy, although I am unaware of any insects that have a drag-based stroke at very low *Re*. It is important to point out that neither lift- nor drag-based weight support mechanisms are efficient at *Re*<100, and particularly at *Re<20*, which is the range of the smallest flying insects. This may help explain the importance of additional flight strategies not included in this study, such as wing-wing interactions (Lighthill 1973, Weis-Fogh 1973, Maxworthy 1979, Ellington 1984, Ellington 1984, Spedding and Maxworthy 1986, Sun and Xin 2003, Lehmann, Sane et al. 2005, Miller and Peskin 2005, Sun and Yu 2006, Lehmann and Pick 2007, Miller and Peskin 2009) and bristled wings (Cheer and Koehl 1987, Sunada, Takashima et al. 2002).

3.5. Limitations

This study only considers the vertical force that could be produced by tiny insects. I did not consider the advantages that either lift or drag based mechanisms might have for other components of flight. Previous computational work for larger insects has shown that it is easy to synthesize optimized computational models of wing strokes that exceed the performance of the biological stroke when the measurement of aerodynamic performance is defined in terms of force, power, or efficiency (Berman and Wang 2007, Nakata and Liu 2012, Zheng, Hedrick et al. 2013). However, the design of insect wing kinematics is the result of compromise among many factors, including stability, maneuverability, control, and wing strength. Vertical force alone cannot fully explain whether tiny insects would use lift or drag mechanisms. For example, at higher *Re*, stability increases as the stroke plane angle increases (Xu and Sun 2014). Additional studies into the maneuverability, stability and control of insects at low *Re* would be beneficial to understanding the flight strategies employed by these insects.

While this study was conducted using 2D cross sections of an insect wing, I expect that the 3D geometry of wings will play an important role in aerodynamic performance. In general, 2D studies fail to capture any effects from spanwise flow, and there can be differences in the separation of the LEV, especially at higher *Re* (Wang, Birch et al. 2004). The 2D study also fails to take into account that the flapping wings of insects are rotated about a wing base, rather than translated. Especially during stroke reversal with a tilted stroke plane, the vector normal to the wing surface does not typically point upward. This effect is more significant for insects with larger wing stroke amplitudes. I only considered linear stroke planes, but the wing tip of many insects actually trace more complicated patterns such as ovals, parabolas, or figure eights (Wang 2004). I also did not consider the effects of wing-wing interactions, which could be quite important since it is widely

believed that many tiny insects use clap and fling to enhance lift (Weis-Fogh 1973). Large forces are required to fling the wings apart at low *Re* (Miller and Peskin 2005), but it is possible that bristles on the wing could reduce the force required to clap the wings together and fling the wings apart (Miller and Peskin 2009). The flight mechanisms employed by insects at $Re<100$ requires further investigation.

CHAPTER 4: A NUMERICAL STUDY OF THE ROLE OF BRISTLES IN SMALL INSECT FLIGHT

4.1 Introduction

The fluid dynamics of flow through bristled appendages similar to those on the wings of small insects have been explored with physical (Loudon, Best et al. 1994, Sunada, Takashima et al. 2002), analytical (Cheer and Koehl 1987) and numerical models (Barta and Weihs 2006, Weihs and Barta 2008, Barta 2011, Davidi and Weihs 2012). However, the physiological or mechanical importance of bristled insect wings remains a mystery.

Previous work suggests that a single wing with bristles engaged in steady translation or rotation is almost as effective as a solid wing at producing aerodynamic forces (Sunada, Takashima et al. 2002) (Davidi and Weihs 2012). While these works suggest that bristles may not significantly alter the aerodynamic forces experienced by a single wing during steady translation, the bristles might offer an aerodynamic benefit during wing-wing interactions (i.e. 'clap and fling'). Miller and Peskin (2005) showed that very large forces are required to fling insect wings apart, particularly at $Re<20$, the range of the smallest flying insects. They suggested that bristled wings could reduce the force required to clap the wings together and fling the wings apart (Miller and Peskin 2009).

If the Re_b and spacing of the bristles are near the transition where the bristled appendage acts either as a solid paddle or leaky rake (Cheer and Koehl 1987), then during clap and fling it could be possible for the wing to preserve lift by acting as a solid plate during the translational part of the stroke and a leaky rake during the fling. Experiments with physical models have

shown that leakiness is increased when bristles move near a boundary (Loudon, Best et al. 1994). During the fling, there could be some flow between the wings' bristles enhanced by the presence of the other wing, which would reduce the force required to fling the wings apart. This idea is supported by a previous numerical study of porous wings that showed that porous wings, compared to solid wings, reduce the drag required to fling two wings apart (Santhanakrishnan, Robinson et al. 2014). However, it is unclear if a bristled wing can be treated as a homogenized porous layer, and if so, what the biologically reasonable permeability should be.

The goal of this study was to investigate if bristled wings could reduce the force required to fling the wings apart during clap and fling while still maintaining lift during translation. The challenge of studying the fluid dynamics of bristles was in resolving the fluid flow between the bristles. In order to accurately model the flow between the bristles, a very high grid resolution was required. The effect of Reynolds number, angle of attack, bristle spacing, and wing-wing interactions were investigated.

4.2 Methods

4.2.1. Bristles modeled in 2D.

An insect wing stroke is commonly approximated in two dimensions using a cross section through the chord of the wing, as was seen in Chapter 3. Similarly, a row of bristles on an insect wing can be modelled in two dimensions by taking a cross section through the bristles (**Fig. 4.1a**). The resulting row of two-dimensional cylinders can then be moved to perform desired kinematics (**Fig. 4.1b**), and the resulting forces and flow structures can be quantified.

In this study, bristles were modeled as rows of two-dimensional cylinders. In cases with full wings, three different gap to diameter (G/D) ratios were compared to each other and to a solid wing (**Fig. 4.2**). The G/D ratios were 5:1, 11:1, and 17:1, and the number of bristles per

wing were 25, 13, and 9, respectively. These G/D ratios were selected because they capture the range commonly observed in tiny flying insects (approximately 4-12). The number of bristles per wing was selected to allow for the total chord length of the wing, *c*, to remain constant at 145 bristle diameters. In this way, the chord-based Reynolds number, Re_c was identical for all of the wings, regardless of G/D.

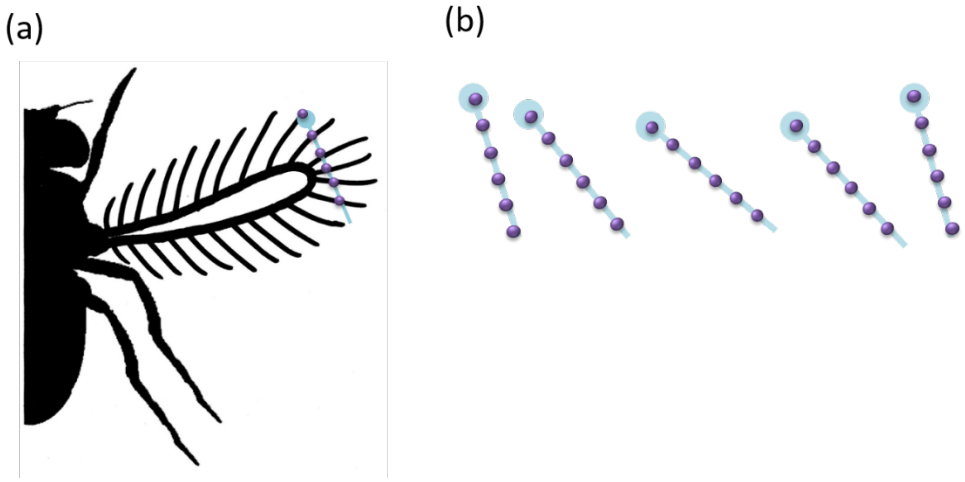

Figure 4.1. A bristled wing can be modeled in two-dimensions using a cross section through the chord of the wing (a). The row of two-dimensional cylinders can then be modeled performing desired kinematics (b).

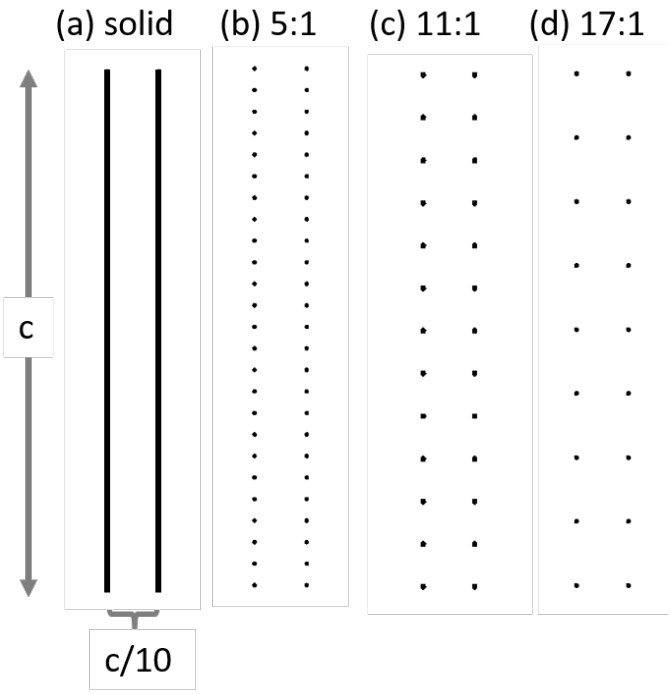

Figure 4.2. The fluid dynamic forces and leakiness were compared between (a) a solid wing and bristled wings with three gap to diameter (G/D) ratios: (b) 5:1, (c) 11:1 and (d) 17:1. In all four cases, the wings were the same length, c, and in cases with two wings, the wings were spaced c/10 apart.

4.2.2 Chord-based and bristle-based Reynolds numbers

For this study, it was important to differentiate the bristle-based Reynolds number (Re_b) and the chord-based Reynolds number (Re_c). Re_b and Re_c were each defined using Eq. 1.1.

$$Re_b = \frac{\rho U D}{\mu} \quad \text{and} \quad Re_c = \frac{\rho U c}{\mu}$$

where the diameter of the bristle, D, was the characteristic length for Re_b. And the total length of the chord, *c*, was the characteristic length for Re_c. In general, the characteristic velocity, *U*, is defined as the average wing tip velocity of the insect, and in the simulations, *U* was defined as the steady state velocity of the chord. Tiny insects are generally reported to fly at Re_c ranging from 4-20. In contrast, Re_b has been reported to be on the order of 10^{-2} for thrips (Ellington 1975) and 10^{-1} for *Encarsia formos*a (Kuethe 1975). For this study, Re_b was varied from 10^{-1} to 10^{-3} for

cases with full wings. Because the total chord length of the wing remained constant at 145D, Re_c was 145 times larger than Re_b (see **Table 4.1**). The Re_b most relevant to tiny insects are 10^{-1} and 10^{-2}, which corresponds to Re_c of 14.5 and 1.45, respectively. While Re_c=1.45 is slightly lower than that observed biologically, these Re_c are of the order of magnitude relevant to tiny insect flight.

Table 4.1 Comparison of bristle-based and chord-based Reynolds numbers for full wings

Re_b	Re_c
0.5	72.5
10^{-1}	14.5
10^{-2}	1.45
10^{-3}	0.145

4.2.3 Leakiness.

The leakiness (**Fig. 4.3**) of a pair of bristles was defined as the ratio of the volume of fluid that actually moves between a pair of bristles to the volume across which that bristle pair sweeps in a unit of time (Cheer and Koehl 1987).

$$Leakiness = \frac{V_{leak}}{V_{sweep}}$$

Where V_{leak} is the volume of fluid that actually moves between two cylinders, and V_{sweep} is the volume across which the cylinders sweep. The leakiness for a pair of cylinders has been calculated analytically over a range of Re_b previously (**Fig. 4.4**). In general, leakiness increases with increasing Re_b and G/D (Cheer and Koehl 1987).

I used Visit (Childs 2013) to determine the leakiness from numerical simulations. I performed a lineout operation on the fluid velocity between two bristles, then integrated to determine the leakiness.

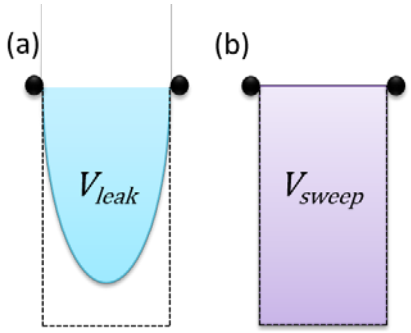

Figure 4.3. Leakiness is the ratio of (a) the volume of viscous fluid that actually moves between a pair of bristles to (b) the volume across which that bristle pair sweeps in a unit of time (the volume of fluid that would move between the bristles in an inviscid fluid).

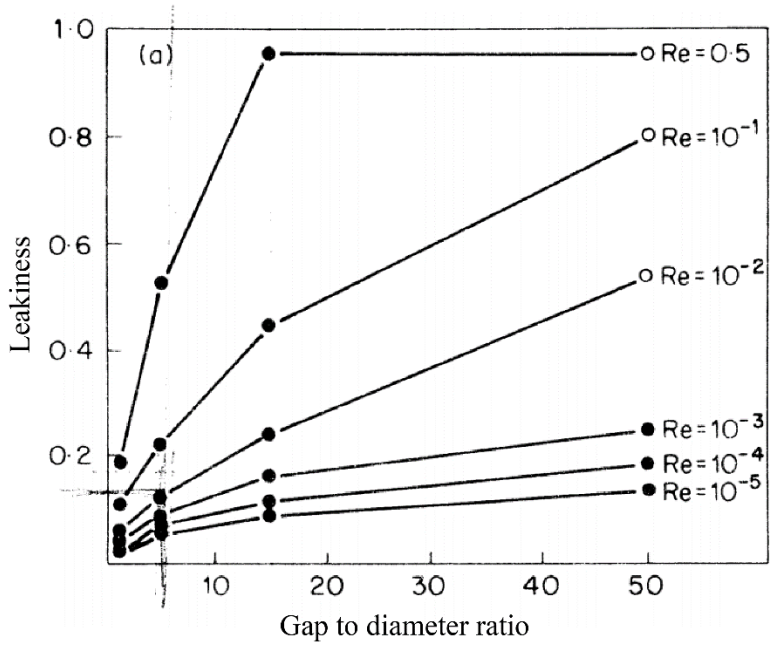

Figure 4.4. Leakiness as a function of gap to diameter ratio for a pair of cylinders (reproduced from Cheer and Koehl 1987).

4.2.4 Dimensionless drag

In order to compare the forces from the computations, instantaneous forces experienced by the wing were non-dimensionalized by $0.5\rho U^2 L$, where U was the characteristic steady state velocity. L was the characteristic length and depended on the application. For simulations with only 2 bristles and simulations comparing the effect of additional bristles, L was the bristle diameter, D, and the reported force was that for each individual bristle. For simulations with full length wings, L was the chord length, c, and the reported force was the sum of the forces experienced by the entire row of bristles. C_L and C_D denote the lift and drag coefficients, respectively.

4.2.5 Numerical method

I used the IBFE method as described in Chapter 2.1.2 to model two-dimensional bristles immersed in a viscous, incompressible fluid. The finite element bristle meshes were constructed using Gmsh (Geuzaine and Remacle 2009) and each individual bristle consisted of at least 16 triangular elements. In cases with full wings, the wings used the G/D ratios and number of bristles listed in Section 4.2.1. The computational domain was 500 bristle diameters wide and high. And the bristles were at least 100 bristle diameters from the edges of the computational domain at all times.

I used IBAMR (Griffith, Hornung et al. 2007), as described in Chapter 2, for all of the fluid dynamic simulations. The adaptive method used four grid levels to discretize the Eulerian equations with a refinement ratio of four between levels. Regions of fluid that contained the bristles or vorticity above 0.125 were discretized at the highest refinement. The effective resolution of the finest level of the grid corresponded to that of a uniform 2048×2048 discretization. The boundary conditions were set to no-slip (**u**=0) on all sides of the computational domain. The bristles were

moved using a preferred position that was changed in time. A penalty force was applied proportional to the distance between the actual and desired boundaries. Other simulation-specific numerical parameters are listed in **Table 4.2**.

Table 4.2. Numerical parameters.

Dimensionless parameter	**Value**
Bristle diameter (D)	0.001
Velocity	0.02
Domain length (L)	0.5
Finest Grid Refinement	2048×2048
Number of refinement levels	4
Refinement ratio	1:4
Time step (dt)	1.0e-6
Final simulation time	5
Spatial step size (dx)	L/2048
Stiffness (kappa_s)	1e11

4.2.6 Grid convergence study.

The grid convergence study had two components. (1) Unique to this study, the effective radius of the immersed boundary in IBFE, as a result of the discretized, smooth delta functions, was investigated and the radii of the bristles were modified to compensate for the extra width due to the delta functions. (2) As is typical in immersed boundary numerical studies, spatial convergence was investigated.

Because I am investigating the effect of bristle size and spacing in this study, the effective diameter of the bristles is important. When using the standard delta function (**Fig. 4.5.a**) for the classical immersed boundary method (Peskin 2002), a single immersed boundary point interacts with the fluid like a sphere with radius 1.255 grid cells in Stokes flow (Bringley and Peskin 2008), however this needs to be validated for the full Navier Stokes equations. As a

result, a bristle of diameter, D, (**Fig. 4.5.b**) would have an effective radius greater than D (**Fig. 4.5.c**), and the diameter of the bristle would need to be decreased to accommodate the effective radius (**Fig. 4.5.d**).

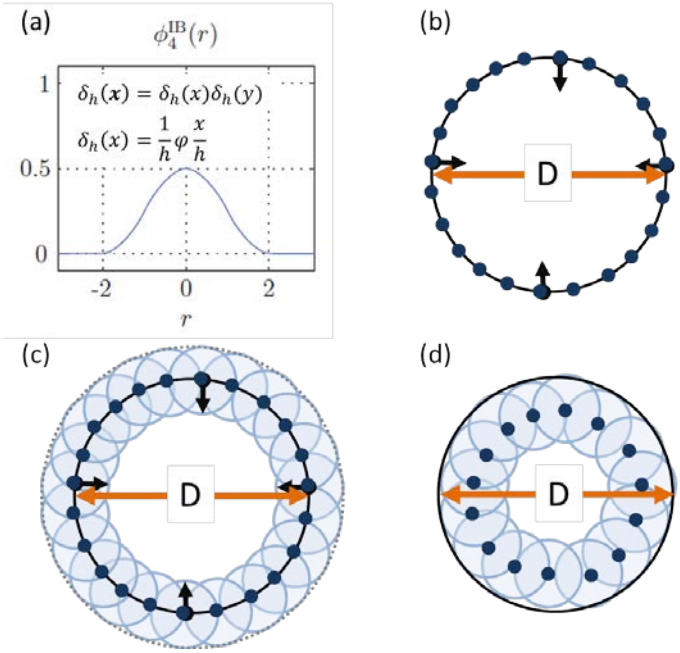

Figure 4.5. The effect of the delta function on the diameter of an immersed boundary bristle. (a) The regularized 2D delta function has the support of 4 Cartesian grid cells in the classical immersed boundary method. A bristle modeled as a 2D cylinder (b), with diameter, D, would actually have an effective diameter greater than D (c), because each boundary point acts like a sphere with an effective radius (light blue circles) dependent on the fluid discretization. (d) When constructing the bristles, the center of the immersed boundary points should be adjusted inward so that the effective diameter is D.

A key difference between the classical IB method and the IBFE method used in this chapter is that rather than spreading forces from the nodes of the boundary mesh, the forces are instead spread from quadrature points within the interiors of the Lagrangian finite elements. Consequently, calculating the effective radius of the node points of a mesh was not straight forward, and needed to be quantified numerically. I assumed that the effective radius was between 0 and 2 fluid grid points, and decreased the radius of the bristle meshes accordingly. I

combined this study with a standard spatial convergence study across different grid sizes (**Fig. 4.6**).

Changes in spacing between neighboring bristles have the most pronounced effect at Re_b approaching 1 and when the bristles are already fairly close together (Cheer and Koehl 1987). For that reason, the grid refinement study focused on two bristles with $Re_b = 10^{-1}$ (the largest Re_b used in this study) and a G/D ratio of 5:1 (the smallest spacing used in this study). To test for spatial convergence, I compared a uniform 1024×1024 discretization, a uniform 2048×2048 discretization, and a uniform 4096×4096 discretization. These three resolutions were compared for 2 bristles translating at a constant velocity (G/D=5:1, Re_b=1e-1). The average leakiness at steady state are shown in **Fig. 4.6**.

To accommodate the effect of the discretized delta functions, I confirmed that the appropriate distance required to compensate for the effective added radius was 1.5 grid cells, by investigating the effect that decreasing the bristle radius from 0 to 2 grid cells had on leakiness. The bristle radius was decreased by 1.5 fluid grid cells for all further simulations in this chapter. With this adjustment, the average percent difference in leakiness between the 2048×2048 discretization and the 4096×4096 discretization was less than 3%. For computational efficiency, effective 2048×2048 discretization was used for all other simulations in this chapter.

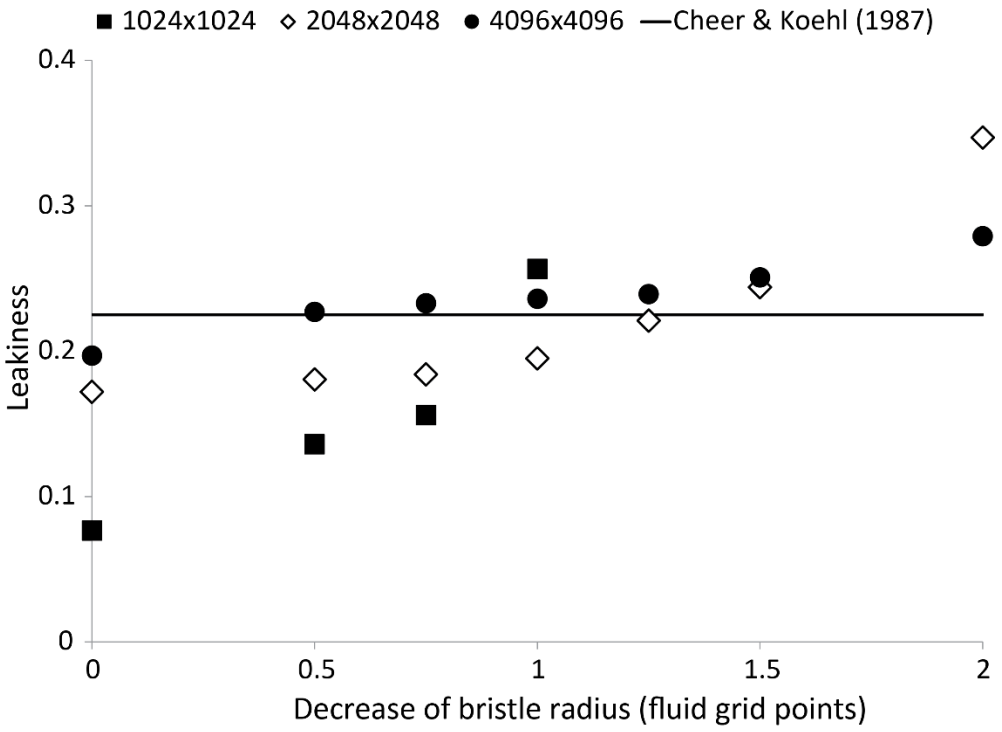

Figure 4.6. Grid convergence study. Leakiness for three mesh widths (2 bristles at Re_b=10^{-1} and G/D=5). The x-axis is the number of fluid grid points that the bristle radius is decreased in order to compensate for the effective radius of an immersed boundary point using the discretized delta function. The leakiness determined by Cheer and Koehl using an analytical model at this Re_b and G/D is plotted for reference. The 2048X2048 grid and 1.5 dx adjustment were used for all remaining simulations in this chapter.

4.2.7 Considering wall effects.

In this study, the boundaries of the computational fluid domain acted as walls, just like the walls of an experimental flow tank. The effect these walls have on the fluid flow needs to be considered when interpreting the results. At low *Re*, the influence of walls, even at great distances, is unexpectedly great; for example, a two-fold increase in drag is observed for a cylinder 500 diameters from a wall at Re_b=10^{-4} (White 1946). The following formula estimates when wall effects can be ignored (Vogel 1981):

$$\frac{y}{l} > \frac{20}{Re} \qquad \text{Eq. 4.1}$$

where y is the distance to the wall and l is a characteristic length. Using this estimate, the nearest wall would have to be 20,000 diameters away before wall effects could be ignored at $Re_b=10^{-3}$. Unfortunately, limitations in the computational models in this study prevent wall distances of this magnitude.

Luckily, Loudon and Koehl demonstrated that when the distance from the closest side wall is 15 cylinder diameters or greater, leakiness changes very slowly with distance from the wall (Loudon, Best et al. 1994). So while wall effects cannot be avoided, the magnitude of the effect should be minimal so long as the distance from the sides are greater than 15 diameters. In this study, the bristles are always at least 100 diameters from the walls.

4.3 Results

4.3.1 Validation study.

In order to validate the numerical model, I compared the results of the model to a previously published analytical model given by Cheer and Koehl (1987). In the model by Cheer and Koehl, the drag acting on the bristles and leakiness between 2 two-dimensional bristles were solved analytically. To compare my numerical model to the previously published analytical model, I simulated two bristles translating at a steady velocity over a range of Re_b (**Fig. 4.7**). At lower Re_b, a large region of fluid was moved with the bristles and the bristles acted more like a solid plate. At larger Re_b, the bristles entrained a smaller region of fluid, and the bristles were leakier. For example, at $Re_b=10^{-3}$ (**Fig. 4.7.d**) the region around the bristles looked like a uniform flow field, whereas at $Re_b=0.5$ (**Fig. 4.7.a**), the direction of flow quickly changed over a short distance from the bristles.

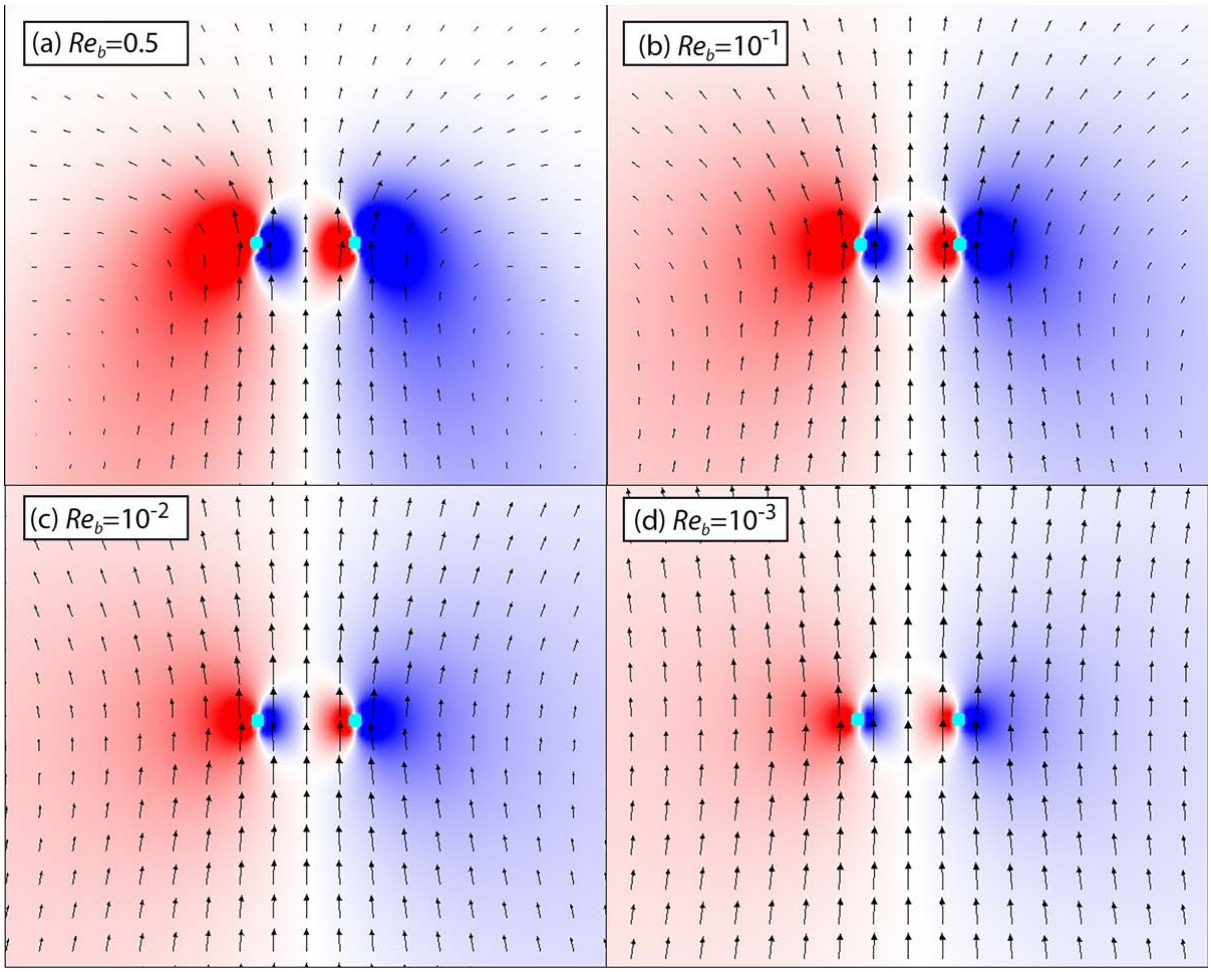

Figure 4.7. Vorticity plots of two bristles (light blue) translating at (a) Re_b=0.5, (b) Re_b=1e-1, (c) Re_b=1e-2 and (d) Re_b=1e-3 (G/D=5:1). The frame shown is at steady state, after the bristles have traveled 150 bristle diameters (the bristles are moving toward the top of the page at a constant velocity). The vectors show the direction of flow and are scaled to the magnitude of the flow velocity (min=0, max=0.2). The color map shows the vorticity of the fluid (min=-30 and max=30; red, counterclockwise rotation; blue, clockwise rotation).

Fig. 4.8 shows the (a) leakiness and (b) forces of my numerical simulation compared to Cheer and Koehl's analytical solution (1987) over a range of Re_b. The reported leakiness and drag are for bristles at steady state. I defined steady state as less than a 1% change in leakiness or force per unit of dimensionless time. Overall, there was good agreement between the IBAMR simulations and the analytical model by Cheer and Koehl (1987). The differences can probably be attributed to the different boundary conditions used in the numerical and analytical models. In the numerical model, wall effects had a greater effect on leakiness and forces at lower Re_b,

whereas the analytical model assumed an infinite domain. This explains why the numerical model was leakier and experienced greater forces than the analytical model at lower Re_b. Differences at higher Re_b may be due to the use of the Oseen approximation in the analytical model.

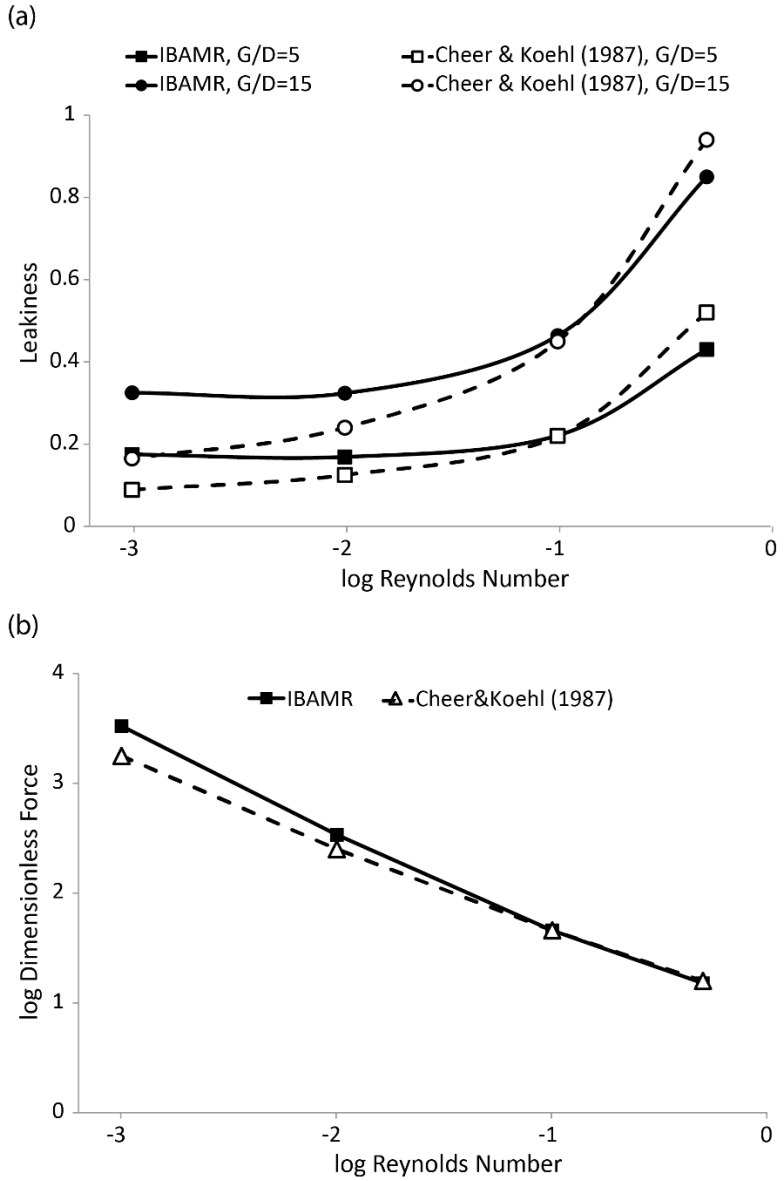

Figure 4.8. Comparison of the numerical method (IBAMR) to a previously published analytical model of 2 bristles. (a) Leakiness as a function of Re_b for a gap to diameter ratio of 5:1 (squares) and 15:1 (circles). Dotted lines represent analytical results from Cheer and Koehl (1987), and solid lines represent the numerical results. (b) The log of the drag coefficient (C_D) plotted vs. the log of Re_b. The data from IBAMR are for a gap to diameter ratio of 5:1. The data from Cheer and Koehl (1987) are those for a 0.1um cylinder with a neighbor 0.3µm away.

4.3.2 Effect of additional bristles on a row.

Given that insect wings consist of an array of 10-100s of bristles, depending on the species, it was important to consider the effect of additional bristles on leakiness and drag. Cheer and Koehl pointed out that under certain conditions, the width of a row of bristles will likely affect leakiness and drag, however they do not explore it quantitatively (Cheer and Koehl 1987). Later work showed that increasing the number of cylinders from two to four decreased the leakiness between individual bristles at Re_b=0.5 and increased the leakiness at Re_b=4 (Koehl 1993). Cheer and Koehl suggested that the shear gradients in the middle region of a row of bristles might be larger than predicted if the row is wide enough that it is easier for fluid in the middle region to move between bristles rather than around the edges (Cheer and Koehl 1987). Therefore, investigating leakiness and drag along the entire width of a finite array of bristles is important to our understanding of bristle function.

A number of studies have investigated the leakiness and drag along a finite row of cylinders in creeping flow (Barta and Weihs 2006, Weihs and Barta 2008, Barta 2011). The more bristles added to the row, the lower the drag exerted on each body becomes, and the drag near the edge of the row is greater than that near the center (Barta and Weihs 2006). Davidi and Weihs reported similar results with the drag distribution along a row of 50 cylinders for Re_c=0.01-100 (Davidi and Weihs 2012) , but they did not report the effect of additional bristles.

I investigated the effect of adding additional bristles for parameters similar to the bristles of thrips (Re_b =10^{-2} and G/D=10). In all cases, the row of bristles was positioned perpendicular to the direction of motion, at a constant velocity. The leakiness and drag were reported when the bristles had traveled 150 diameters and were at steady state. The number of bristles was varied

from 2 to 20 bristles (**Fig. 4.9**). Note that while Re_b remained constant with additional bristles, Re_c would increase as the length of the row increases.

Adding additional bristles to a row had a significant effect on both leakiness and drag. The leakiness was greatest at the edge of a row of bristles (**Fig. 4.9.a**), and smallest at the center. In all cases, the drag (**Fig. 4.9.b**) near the edge of the row was greater than that near the center, which supports previous research (Barta and Weihs 2006). In the absence of wall effects, I would expect that the more bristles added to the row, the lower the drag exerted on each bristle and the lower the leakiness. In these simulations, increasing the number of bristles from 2 to 4 decreased the drag experienced by the center bristles. However, as the number of bristles increased above 6, the drag experienced by each bristle increased. I expect that this was in part due to wall effects. Another possibility was that as the row became wider, it was easier for fluid in the middle region to move between bristles rather than around the edges, increasing the shear gradients around the middle bristles (Cheer and Koehl 1987).

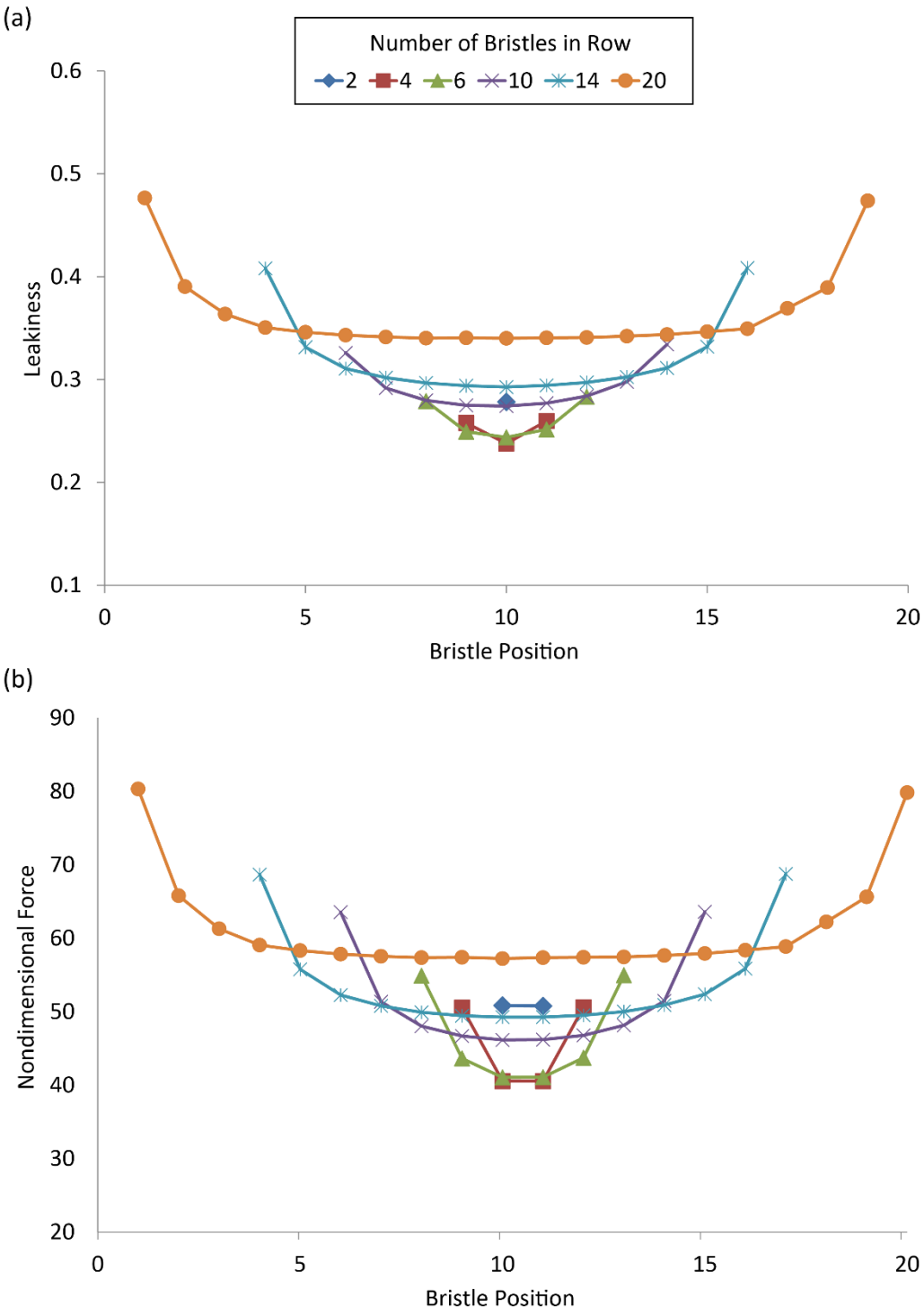

Figure 4.9. Effect of additional bristles on a row (Re_b =10^{-2} and G/D=10). (a) Leakiness and (b) nondimensional drag experienced by each bristle in a two dimensional row, shown for row lengths ranging from 2 to 20 bristles. Steady state drag and leakiness are reported for each bristle translating at a constant velocity.

4.3.3 Bristles and angle of attack.

In addition to the number of bristles, I expected the performance of bristles to change with the angle of the wing relative to the approaching flow (eg. the angle of attack). While studying flow between gill rakers, Cheer et al. discovered that the speed and approaching angle of the flow played a role in generating vortices that reduce the effective size of the gap between rakers, leading to changes in leakiness (Cheer, Cheung et al. 2012). While these results were obtained at Re_b=37.5 to 225, I might expect to see a similar change in leakiness with angle of attack at lower Re_b.

To investigate the effect of angle of attack on bristle performance, I compared the lift and drag experienced by a single wing translating with three different G/D ratios (see **Fig. 4.2**) and at the relevant Re_b of thrips (Re_b=10^{-2}, Re_c=1.45). The angle of attack of the row of bristles ranged from 0° to 90°, and the row translated at a steady velocity until each wing traveled 150 bristle diameters (approximately 1 wing length). The reported force was the sum of the forces experienced by the entire row of bristles, normalized by the chord length as described in Section 4.2.4. C_L and C_D denote the lift and drag coefficients, respectively.

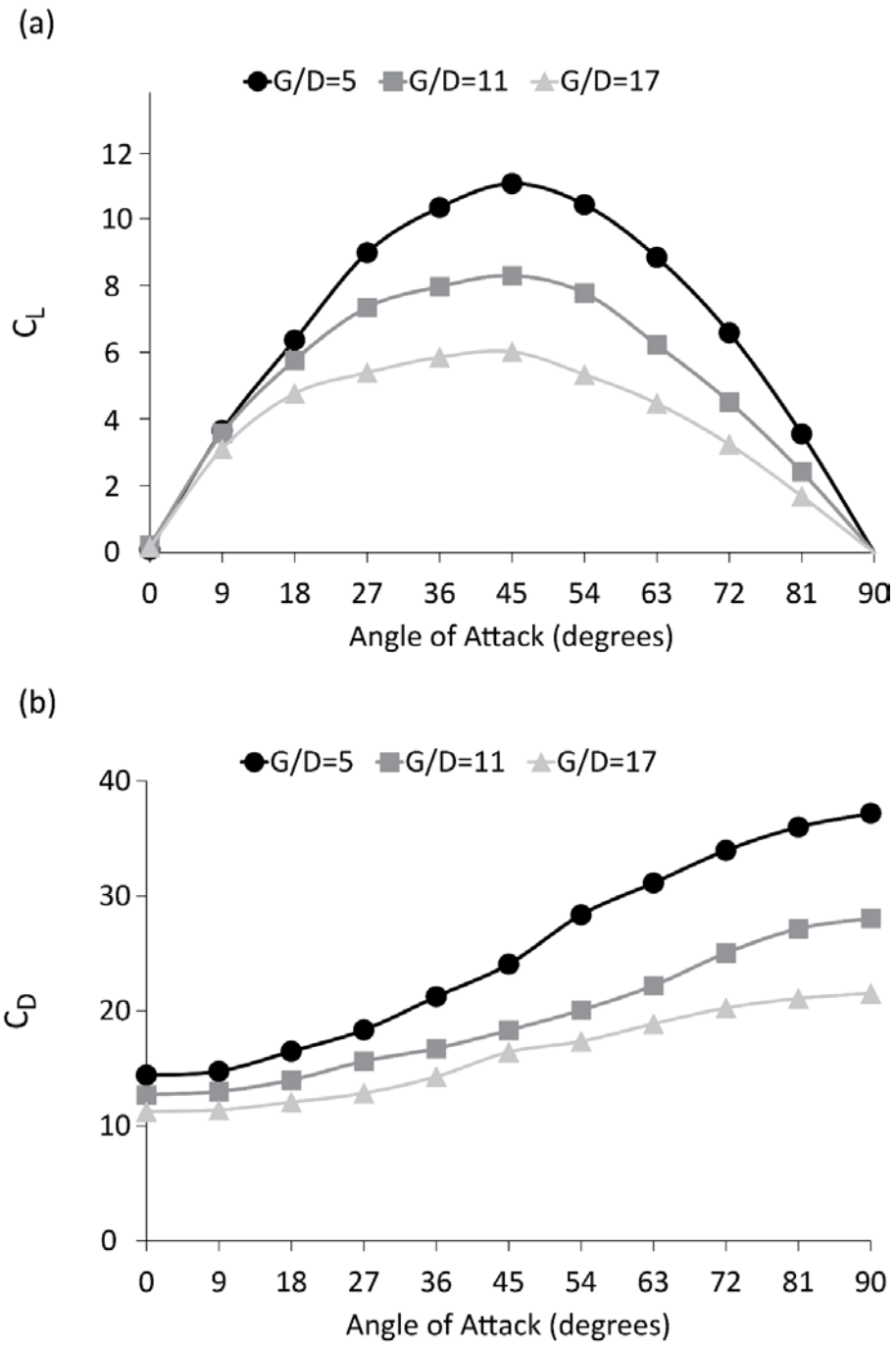

Figure 4.10. Dimensionless (a) lift and (b) drag coefficients experienced by a bristled wing translating at steady state over a range of angles of attack (Re_b=10^{-2}, Re_c=1.45). Three different gap to diameter ratios were investigated: 5:1 (circles), 11:1 (squares), and 17:1 (triangles).

For all angles of attack, the magnitude of the force coefficients decreased with increasing G/D ratios (**Fig. 4.10**). The magnitude of this effect was greatest for lift at angles of attack near 45° (**Fig. 4.10.a**) and the magnitude of this effect was greatest for drag at angles of attack approaching 90° (**Fig. 4.10.b**). Interestingly, the effect of G/D was greater at higher angle of attack than at lower angles of attack. For example, at angle of attack=9°, there was little difference in lift between the three wings, whereas at angle of attack=81°, there was a noticeable increase in lift as G/D decreases. Similarly, there was a smaller difference in drag at lower angles of attack, whereas there was a large increase in drag with decreasing G/D at higher angles of attack. This was most likely because lower angles of attack reduced the effective size of the gap between bristles, leading to changes in leakiness and forces (Cheer, Cheung et al. 2012).

The effect of angle of attack on bristle performance was particularly evident in the aerodynamic polars of the average coefficients of lift and drag shown in **Fig. 4.11.a.** While the G/D affected the lift and drag coefficients at higher angles of attack, it appears to have less influence on the lift and drag at lower angles of attack. While G/D certainly changed the lift and drag experienced by a bristled wing, interestingly it appeared to have little effect on the lift-to-drag ratio (**Fig. 4.11.b.**) In these simulations, there was no difference in C_L/C_D for angles of attack < 27°. And at angles of attack >27°, there appeared to be no difference between G/D=5 and G/D=11, and G/D=17 performed only slightly below the other two.

Flow visualization of the entire bristled wing revealed differences between the different G/D ratios (**Fig. 4.12**). Vector fields of the three G/D ratios translating at an angle of attack of 45° reveal that significantly more fluid was entrained by the wing at lower G/D ratios. The leading edge vortex was slightly more diffuse at G/D=17 (**Fig. 4.12.c**) than at G/D=5 (**Fig. 4.12.a**), which might help explain the slightly larger lift-to-drag ratio at G/D=5 (**Fig. 4.11.b**).

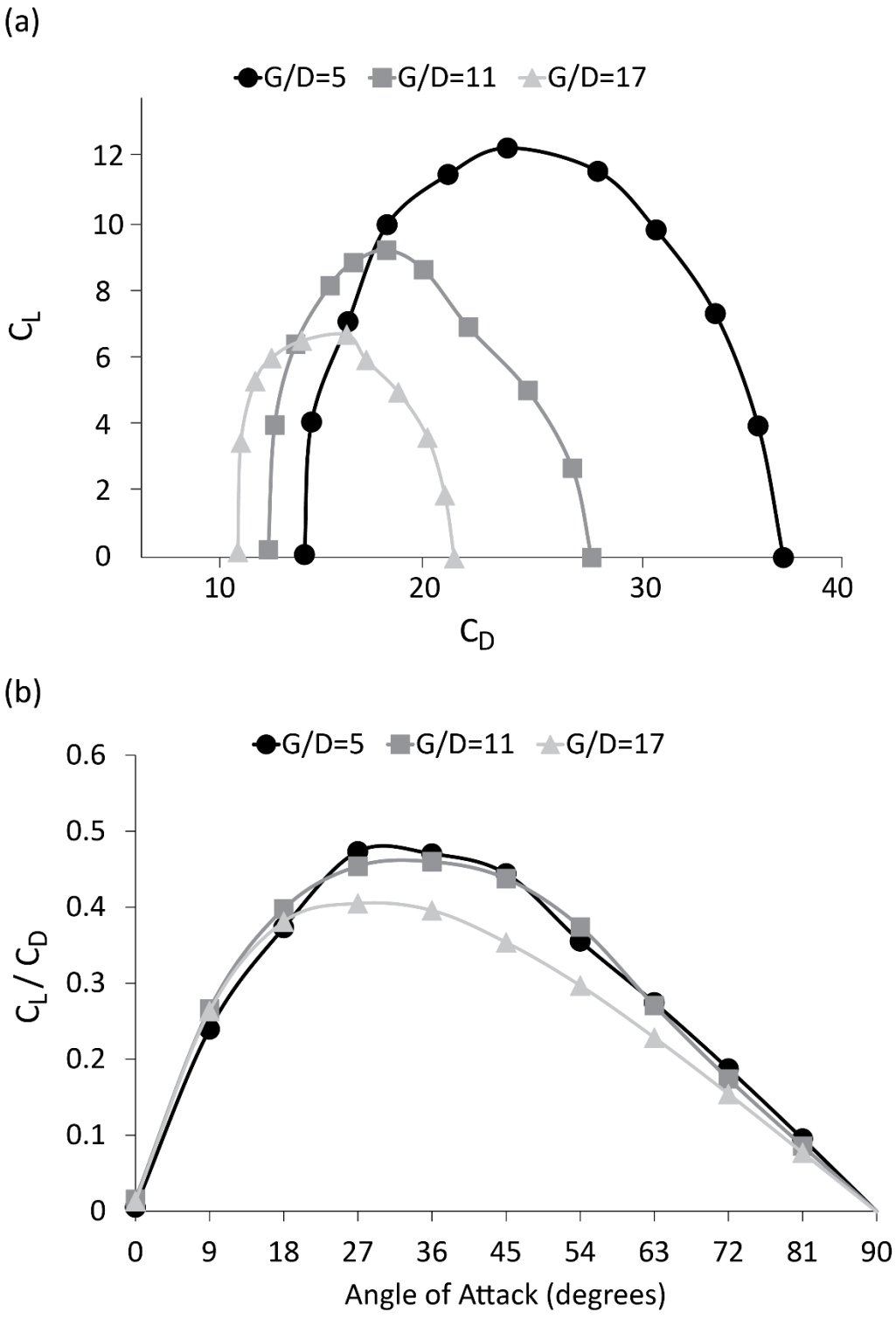

Figure 4.11. Aerodynamic performance of a row of bristles translating at steady state for a range of angles of attack (Re_b=10^{-2}, Re_c=1.45). (a) The aerodynamic polars of the average coefficients of lift and drag for three different gap to diameter ratios and (b) the lift-to-drag ratio over a range of angles of attack.

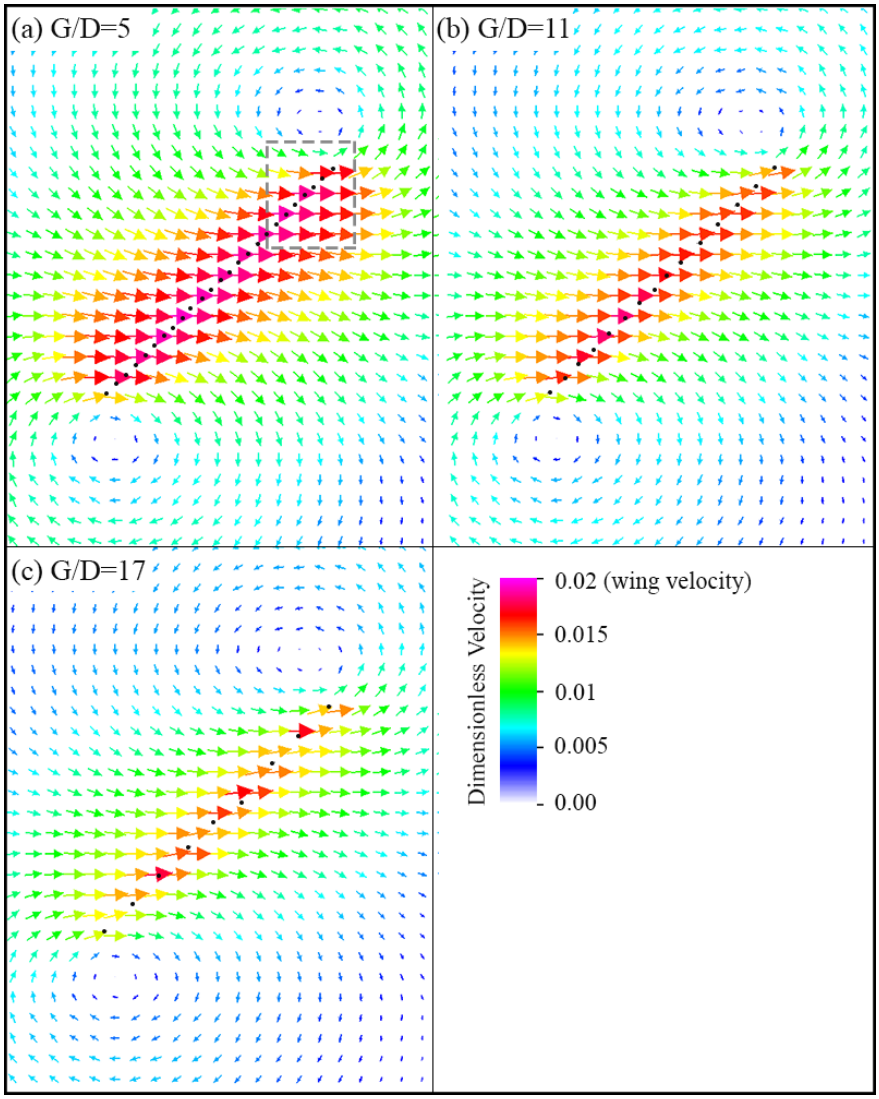

Figure 4.12. Vorticity plots of a row of bristles translating at 45 degree angle of attack and $Re_b=10^{-2}$ ($Re_c=1.45$) with (a) G/D=5, (b) G/D=11, and (c) G/D=17. The row of bristles are moving to the right. The frame shown is at steady state, after the bristles have traveled 150 bristle diameters (approximately 1 wing length). The wing is traveling at a dimensionless velocity of 0.02. The vectors show the direction of flow and the color is scaled to the magnitude of the flow velocity (min=0, max=0.02). The gray dashed box in (a) is the region shown in Figure 4.13.

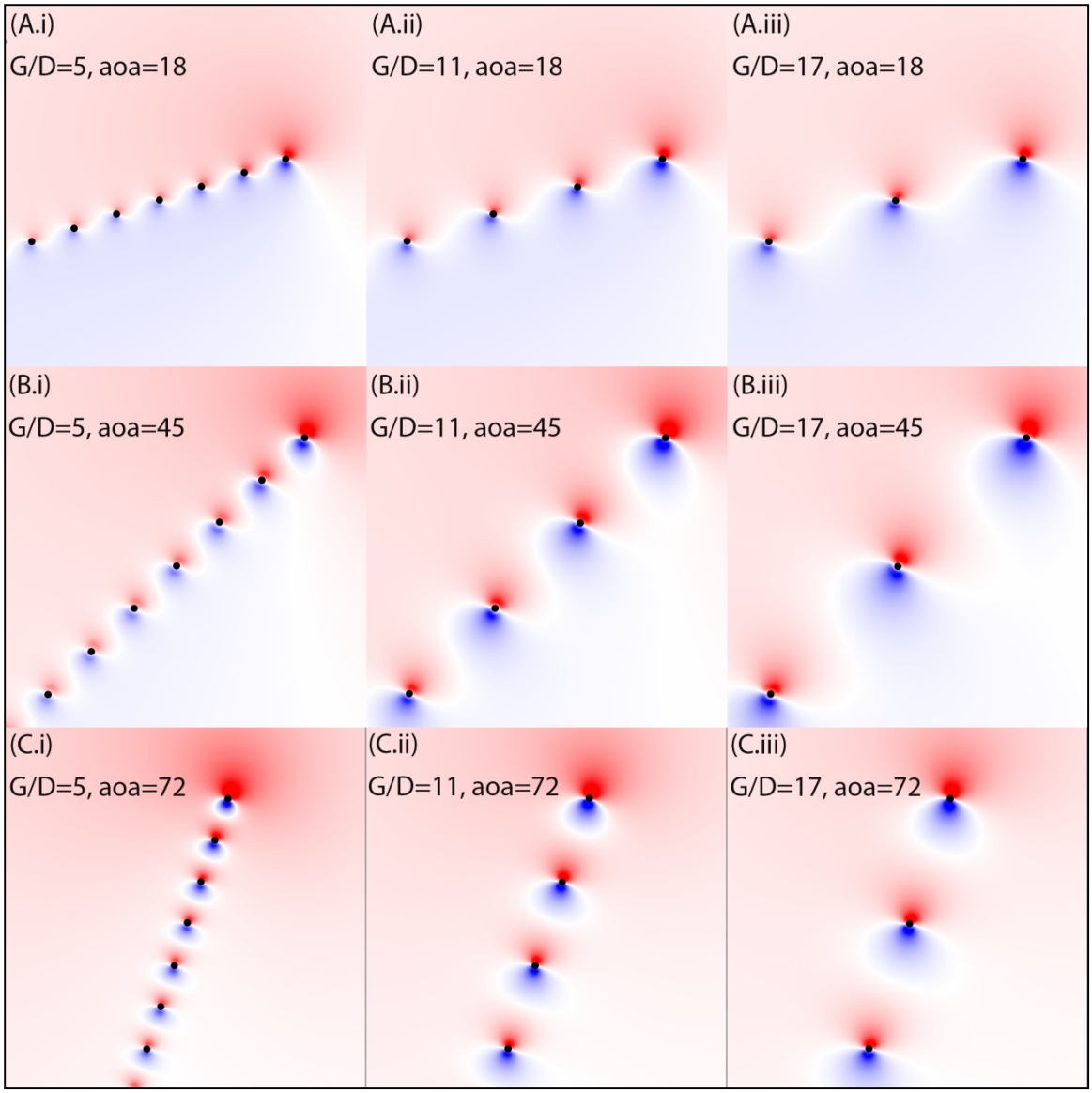

Figure 4.13. Vorticity plots of the leading edge of a row of bristles translating at (a) angle of attack=18°, (b) angle of attack=45°, and (c) angle of attack=72°. The gap to diameter ratios are (i) 5, (ii) 11, and (iii) 17. The row of bristles are moving to the right, and have reached steady state (Re_b=10^{-2}, Re_c=1.45). Only the leading edge of the row is shown (the dashed box in Figure 4.12.a corresponds to B.i. in this figure). The color map shows the vorticity of the fluid (min=-5 and max=5; red, counter clockwise rotation; blue, clockwise rotation).

Concentrating the view in on the dashed box shown in **Fig. 4.12.a** revealed interesting fluid dynamics around the bristles. Vorticity plots (**Fig 4.13**) of the leading edges of the row of bristles at angles of attack = 18°, 45°, and 72° showed differences in the fluid behavior as the angle of attack changes. Each translating bristle generated a pair of oppositely spinning attached vortices.

The magnitude and size of these vortices were greater near the leading and trailing edges of the wing, and smallest near the center of the wing. With decreasing angle of attack, the vortices became more diffuse and extended over a greater area, effectively reducing the size of the gap between bristles (see **Fig 4.13.A**). While studying flow between gill rakers, Cheer et al. discovered a similar relationship between angle of the flow and the effective size of the gap between rakers, leading to changes in leakiness (Cheer, Cheung et al. 2012). This suggests that at lower angles of attack, bristled wings may act more like solid wings than they do at higher angles of attack.

4.3.4 Wing-wing interactions.

To investigate the effect of wing-wing interactions (**Fig 4.14**), I compared a single wing to a pair of wings moving apart. I investigated both pure wing translation and pure wing rotation for bristled and solid pairs of wings (see **Fig 4.2**) at Re_b ranging from 10^{-1} to 10^{-3} (Re_c ranging from 14.5 to 0.145). The wing length, L, was defined as the length of the row of bristles and is constant across all G/D ratios.

In the case of two wings translating apart (**Fig 4.14.a**), the wings started at a distance of 0.1c, where c is the chord length of the wing, based on observations of clap and fling in thrips (Santhanakrishnan, Robinson et al. 2014). They accelerated over a distance of 0.05c, then translated at a steady state velocity until each wing had traveled 0.8c, so that the two wings were 2c apart at the end of the simulation. For a single wing translating, the wing performed the exact same kinematics, without the presence of a second wing.

In the case of two wings rotating apart (**Fig 4.14.b**), the wing rotated about the trailing edge of the wing, as is commonly seen in fling. The velocity and distance traveled was based on the leading edge of the wing. Similar to translation, the wings started at a distance of 0.1c. They accelerated apart until the wing tips had traveled 0.05c, then rotated at a steady velocity until the

wings tips had each traveled 1*c*. For a single wing rotating, the wing performed the exact same kinematics, without the presence of a second wing. Re_b was based on the wing tip velocity.

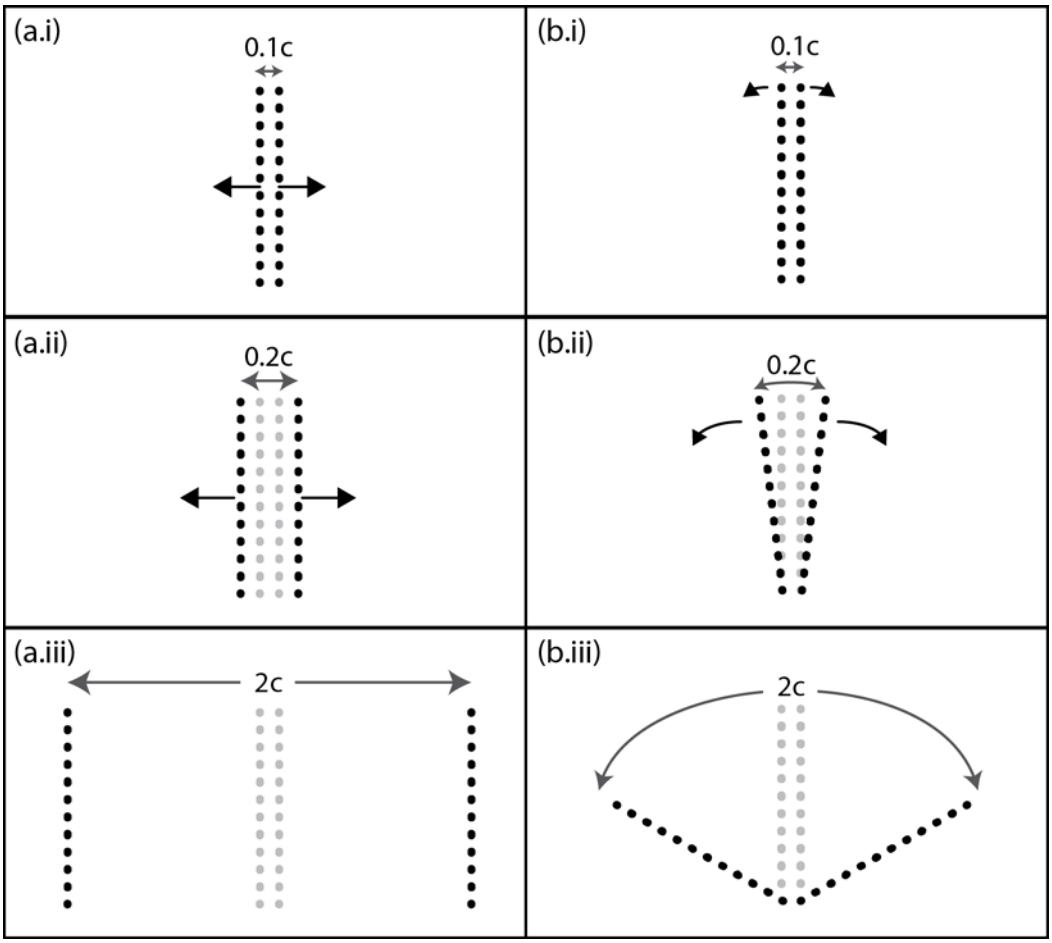

Figure 4.14. Illustration of bristled wing-wing interactions: a row of bristles can (a) translate or (b) rotate apart. In the numerical simulations, the bristled wings start a distance of 0.1c apart (i). They accelerate until they are 0.2c apart (ii), and then translate or rotate at a steady velocity until they are 2c apart (iii). In the case of a translating wing (a), the angle of attack is 90 degrees. In the case of a rotating wing (b), the wing rotates about the trailing edge. Velocity and distance traveled is based on the leading edge. Numerical simulations of a single wing perform the exact same kinematics in the absence of a second wing.

In all cases, the drag required to translate (**Fig 4.15**) or rotate (**Fig 4.16**) two wings apart was greater than the drag required to move a single wing. The peak drag experienced during two

wings performing a “fling” was much greater than the peak drag experienced by a single wing (**Fig 4.15**). This was particularly true at lower Re_b and smaller G/D ratios. For example, there was a 28-fold increase in the maximum drag required to translate two solid wings vs one solid wing at $Re_b=10^{-3}$, whereas, there was only a 5-fold increase in the max drag at $Re_b=10^{-1}$. In contrast, there was a 4-fold increase in the drag required to translate two bristled wings vs one bristled wing at $Re_b=10^{-3}$ and G/D=17, whereas there was only a 0.1-fold increase in the drag required at $Re_b=10^{-1}$. At the biological conditions most relevant to thrips ($Re_b=10^{-2}$ and G/D=11), there was only a 2-fold increase in the drag required to translate two bristled wings vs one bristled wing, compared to a 10-fold increase for a solid wing at the same Re_b.

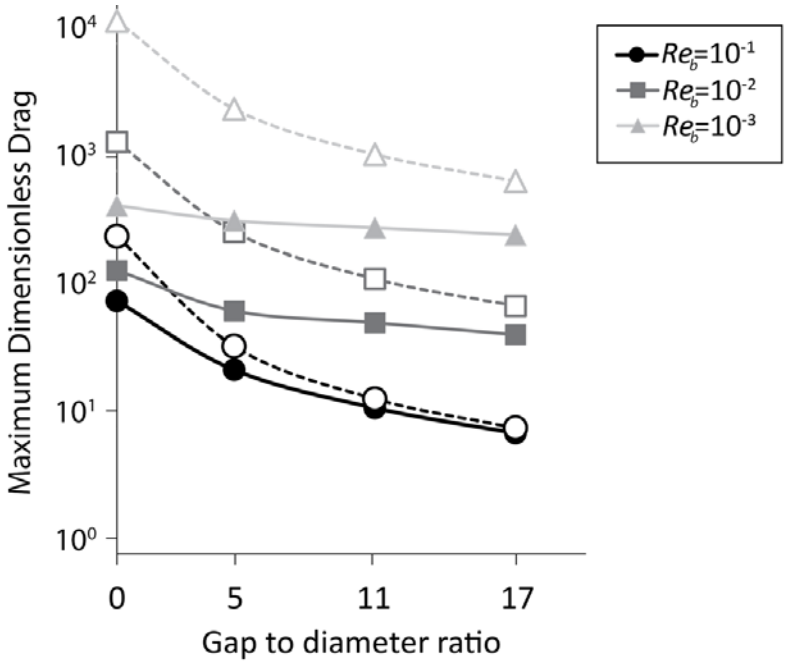

Figure 4.15. Maximum dimensionless drag experienced by 1 wing translating (solid markers) or 2 wings translating apart (open markers) at $Re_b=10^{-1}$ (Re_c=14.5), $Re_b=10^{-2}$ (Re_c=1.45), and $Re_b=10^{-3}$ (Re_c=0.145). The wings accelerate over a distance of 0.05 wing lengths, then translate at a steady velocity. For cases with two wings, the wings start at a distance of 0.1 wing lengths apart. The maximum drag is the peak drag experienced by a single wing translating or the drag experienced by an individual wing that is part of a pair moving apart.

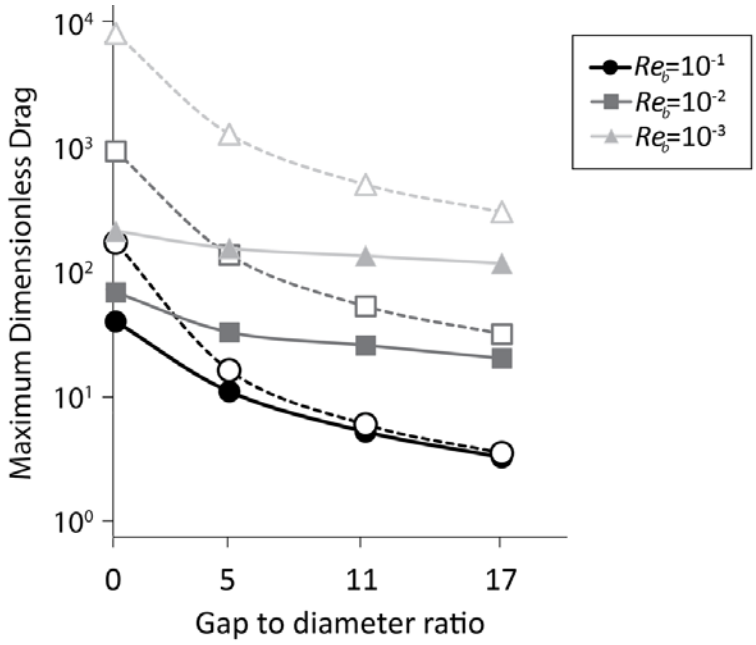

Figure 4.16. Maximum dimensionless drag experienced by 1 wing rotating (solid markers) or 2 wings rotating apart (open markers) at Re_b =10^{-1} (Re_c=14.5), Re_b =10^{-2} (Re_c=1.45), and Re_b =10^{-3} (Re_c=0.145). The wings rotate about the trailing edge of the row of bristles. The wings accelerate until the wing tips are 0.05 wing lengths, then rotate at a steady rotational velocity. For cases with two wings, the wings start at a distance of 0.1 wing lengths apart. The maximum drag is the peak drag experienced by a single wing rotating or the drag experienced by an individual wing that is part of a pair moving apart.

A more careful inspection of the drag as a function of time as two wings translate apart (**Fig 4.17**) reveals more details about the effect of bristles in wing-wing interactions. A similar pattern was seen for the drag of two wings rotating (not shown). In all cases, the drag peaked as the wings accelerated at the beginning of the stroke, then the drag plateaued to a steady state. In all cases, two wings experienced greater drag than a single wing. In particular, the magnitude of the peak was much larger in the presence of a second wing. However, as the wings continued to move farther apart, the drag decreased and approached that of a single wing. The increase in drag in the presence of a second wing was dependent upon Re_b and G/D. The magnitude of the effect increased with decreasing Re_b and decreasing G/D ratio. At the conditions most relevant to thrips

(Re_b =10^{-2} and G/D=11), there was little difference in drag due to the presence of a second wing after the wings traveled 0.5 wing lengths (**Fig 4.17.b**).

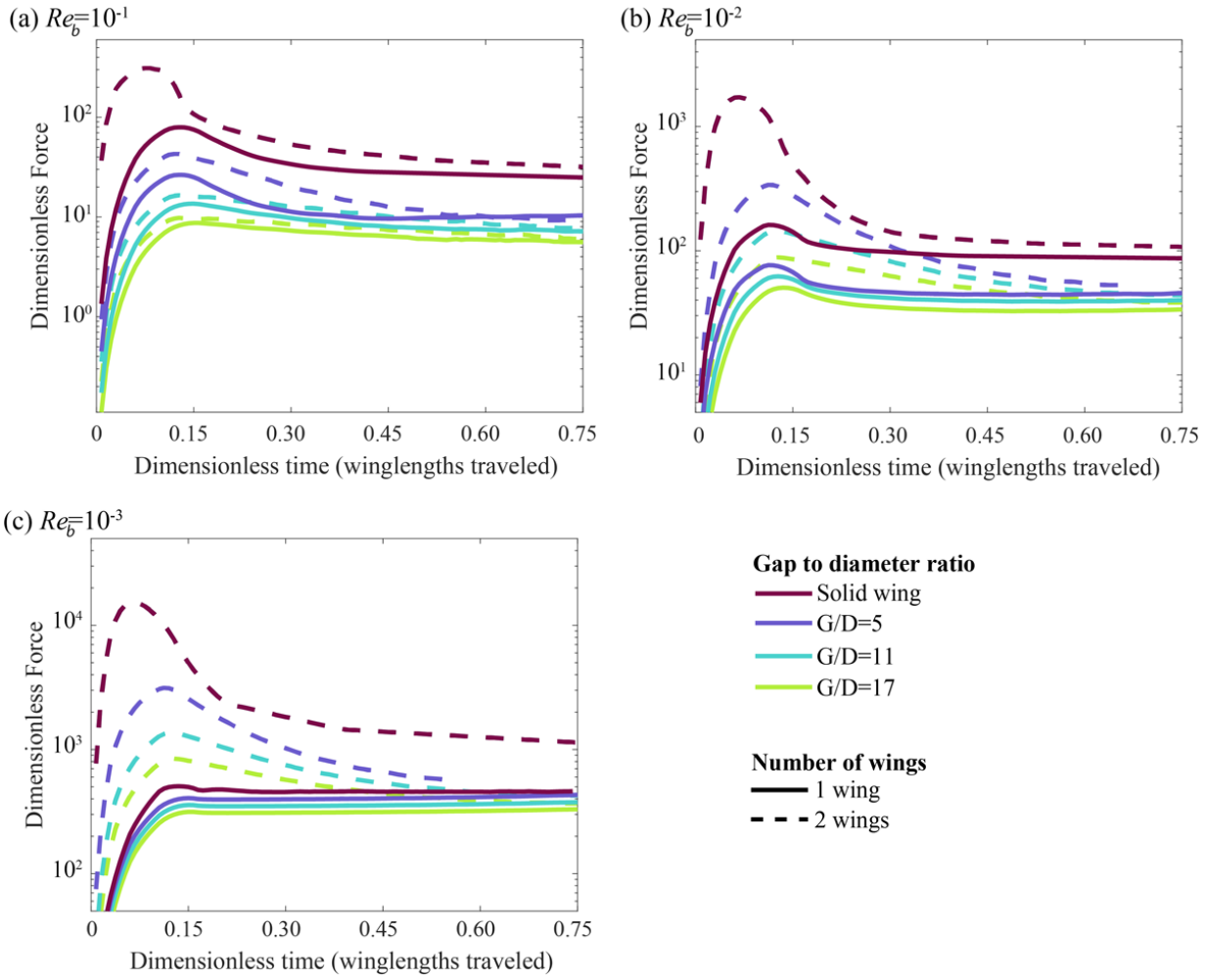

Figure 4.17. Instantaneous dimensionless drag as functions of dimensionless time at (a) Re_b =10^{-1} (Re_c=14.5), (b) Re_b =10^{-2} (Re_c=1.45), and (c) Re_b =10^{-3} (Re_c=0.145). A single wing translating (solid lines) is compared to two wings performing a "fling" (dashed lines) for three different bristle gap to diameter ratios and a solid wing (angle of attack=90°). Only the first 0.75 wing lengths traveled are shown.

Velocity vectors of the fluid around the leading edge of two wings moving apart and a single wing translating are shown for Re_b=10^{-1}, Re_b=10^{-2} and Re_b=10^{-3} in **Figs 4.18**, **4.19** and **4.20**, respectively. In general, the bristles were more leaky as Re_b increased and as G/D increased. The leakiness of the bristles was enhanced with the presence of a second wing. There

were fewer differences in the flow between a single wing and two wings as the Re_b increased and G/D increased. For example, at $Re_b=10^{-1}$ and G/D=17, the fluid fields were very similar between a single wing (**Fig. 4.18.b.i**) and two wings (**Fig. 4.18.a.i**). There was also little difference in the forces experienced by these two cases (**Fig 4.15** and **Fig. 4.17.a**). In both cases, there was fluid flow between bristles in the direction opposite to motion. The magnitude of this fluid flow was greater in the presence of a second wing (**Fig. 4.18.a.i**). As the G/D decreased, however, less fluid was able to flow between bristles.

As the Re_b decreased, differences between one and two wings became more apparent. At $Re_b=10^{-2}$ and $Re_b=10^{-3}$, there was a visible difference in the amount of fluid that travelled with a single wing translating (b) compared with two wings moving apart (a). The presence of a second wing (a) enhanced the flow between bristles, especially at lower Re_b. For example, in the presence of a second wing, fluid flowed between bristles in the direction opposite to motion when G/D=17 (**Figs. 4.19.a.i** and **4.20.a.i**), whereas fluid moved in the direction of motion between bristles in the absence of a second wing (**Figs. 4.19.b.i** and **4.20.b.i**).

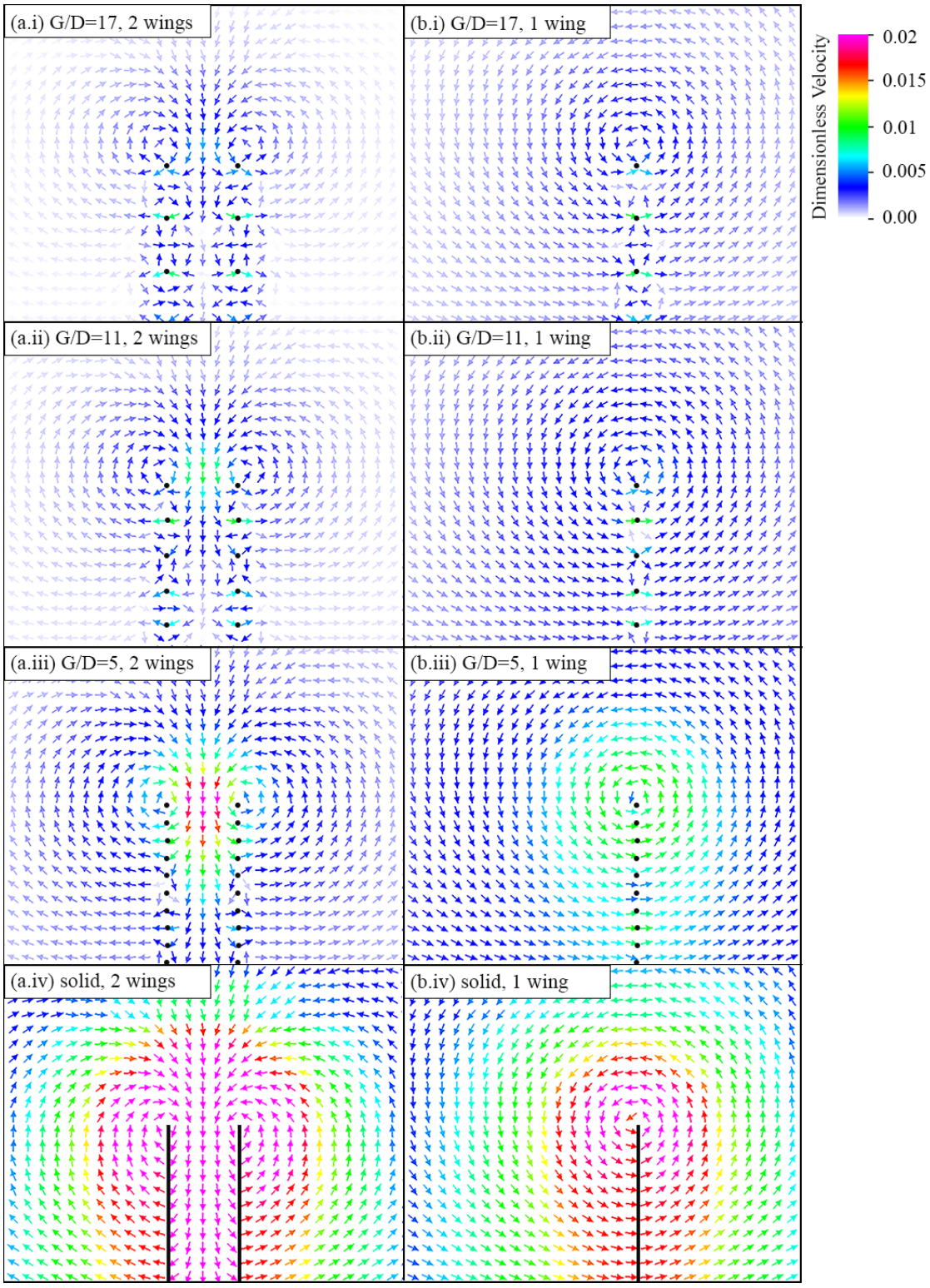

Figure 4.18. Velocity vector field plots of the leading edges of (a) two wings translating apart and (b) a single wing translating to the right at $Re_b=10^{-1}$ ($Re_c=14.5$). Three gap to diameter ratios, (i) 17, (ii) 11, and (iii) 5, are compared to (iv) a solid wing. The frame shown is at the end of acceleration, when the wings are 0.2 wing lengths apart. The vectors show the direction of flow and the color is scaled to the magnitude of the flow velocity (min=0, max=0.02).

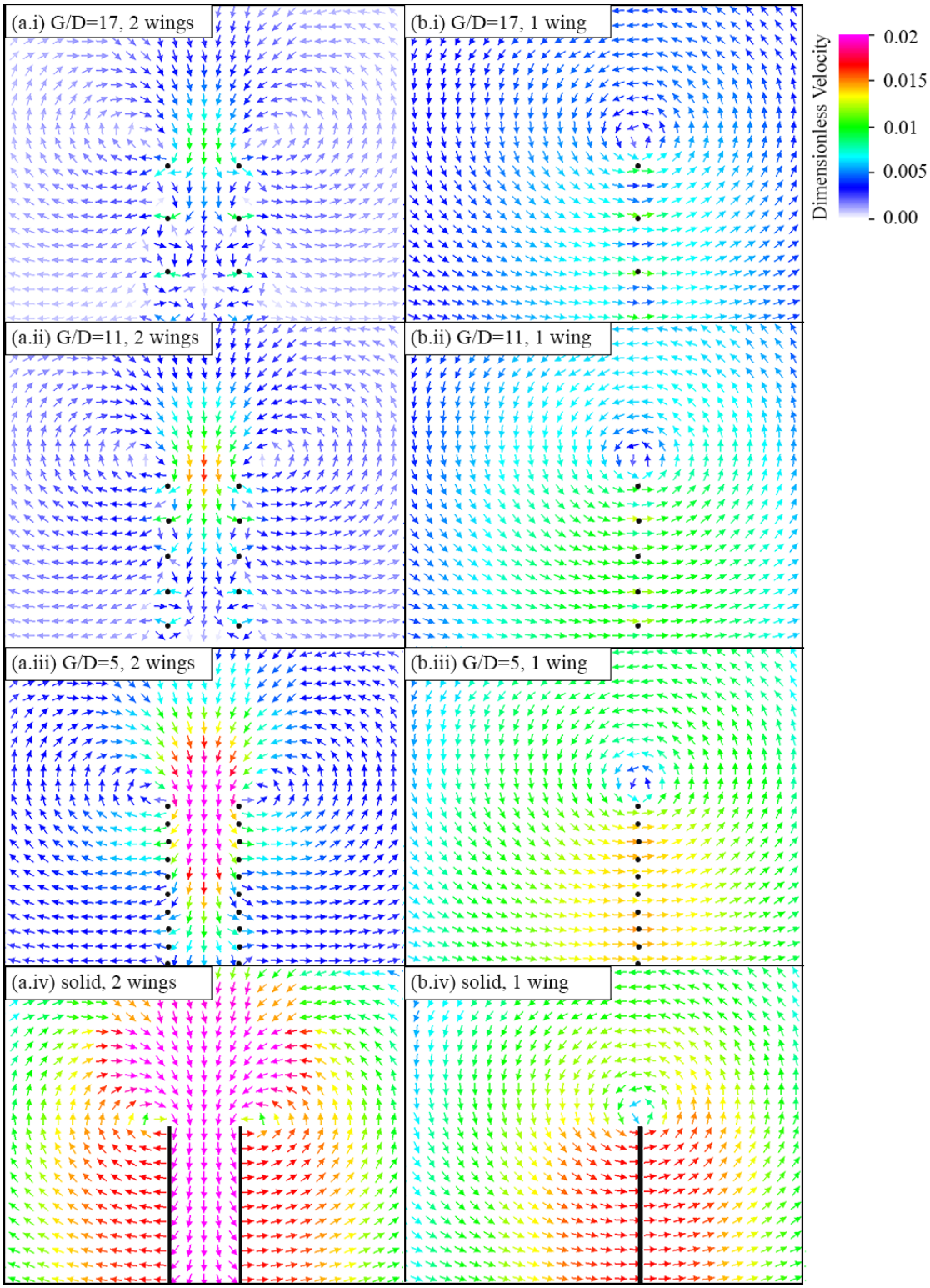

Figure 4.19. Velocity vector field plots of the leading edges of (a) two wings translating apart and (b) a single wing translating to the right at $Re_b=10^{-2}$ ($Re_c=1.45$). Three gap to diameter ratios, (i) 17, (ii) 11, and (iii) 5, are compared to (iv) a solid wing. The frame shown is at the end of acceleration, when the wings are 0.2 wing lengths apart. The vectors show the direction of flow and the color is scaled to the magnitude of the flow velocity (min=0, max=0.02).

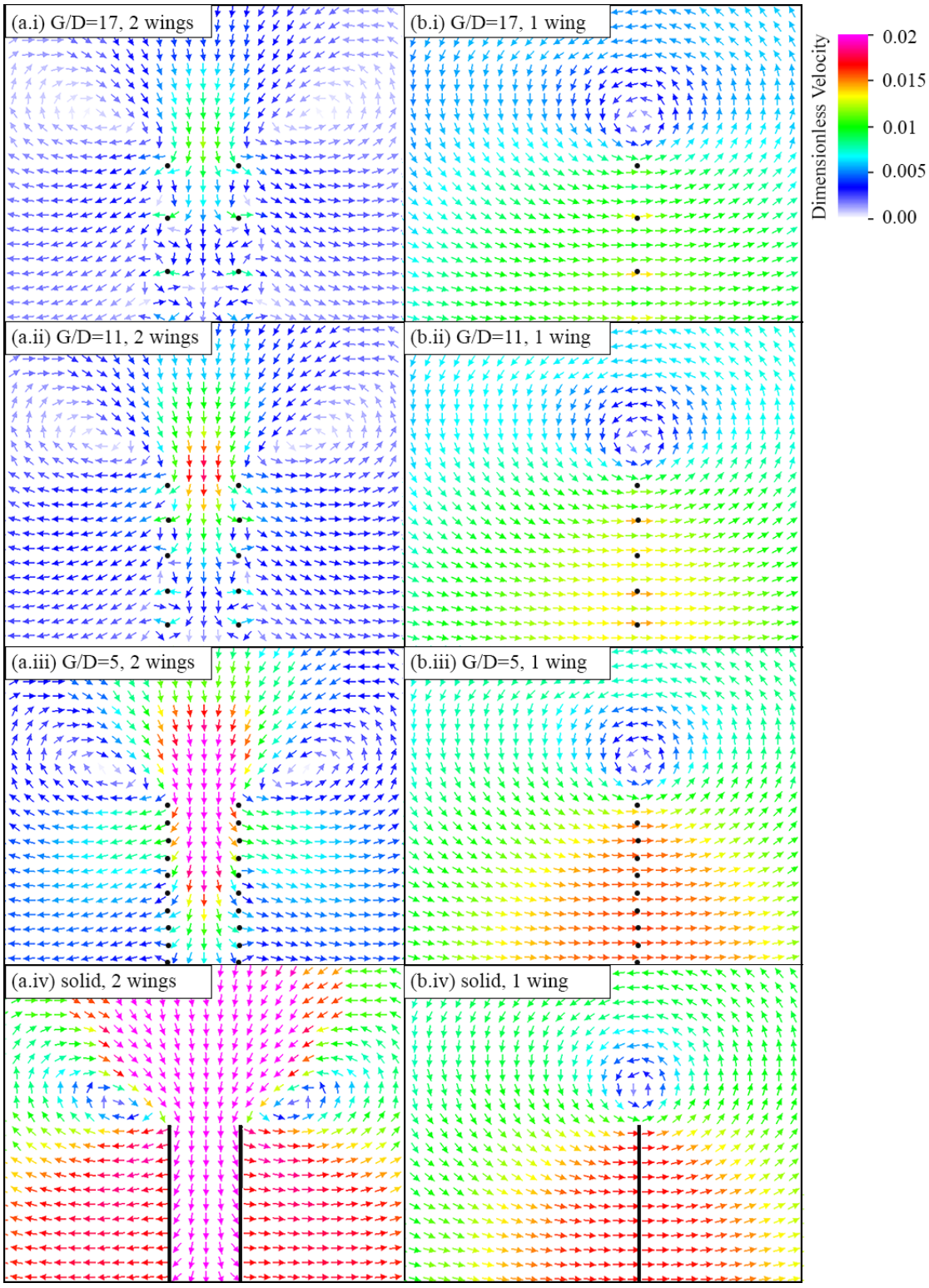

Figure 4.20. Velocity vector field plots of the leading edges of (a) two wings translating apart and (b) a single wing translating to the right at $Re_b=10^{-3}$ ($Re_c=0.14$). Three gap to diameter ratios, (i) 17, (ii) 11, and (iii) 5, are compared to (iv) a solid wing. The frame shown is at the end of acceleration, when the wings are 0.2 wing lengths apart. The vectors show the direction of flow and the color is scaled to the magnitude of the flow velocity (min=0, max=0.02).

4.4 Discussion

In this numerical study, I found that: (1) leakiness and drag are greatest at the edge of a row of bristles and smallest at the center; (2) the decrease in force with increasing gap-to-diameter ratio is greater at higher angles of attack than at lower angles of attack, suggesting that bristled wings may act more like solid wings at lower angles of attack than they do at higher angles of attack; (3) in wing-wing interactions, an increase in drag in the presence of a second wing is Re_b and gap-to-diameter ratio dependent—the magnitude of the effect increased with decreasing Re_b and decreasing gap-to-diameter ratio; and (4) bristled wings significantly decrease the drag required to fling two wings apart compared with solid wings, especially at lower Re_b.

Previous work suggests that single translating bristled wings produce almost as much aerodynamic force as solid wings (Sunada, Takashima et al. 2002) (Davidi and Weihs 2012). My results show that drag and lift decrease as the space between bristles increases (**Fig. 4.10**), however the spacing between bristles appears to have little effect on the lift-to-drag ratio (**Fig. 4.11.b**) over a range of Re_b and angles of attack. A previous study of porous wings in single wing translation also showed no improvement in the lift-to-drag ratio for a biologically relevant range (Santhanakrishnan, Robinson et al. 2014).

My results support the idea that bristles could offer an aerodynamic benefit during wing-wing interactions. To improve lift generation, many tiny insects clap their wings together at the end of upstroke and fling them apart at the beginning of the downstroke in a flight mechanism called ‘clap and fling’. At the Re_b relevant to tiny insects, very large forces are required to clap the wings together and fling the wings apart (Miller and Peskin 2005). A computational study by Miller and Peskin (2009) showed that flexibility can reduce the drag required to fling wings

apart, however the drag generated is still 3-5 times greater than a single wing translating at Re<30. In addition to flexibility, bristles may help reduce the drag experienced during fling. For example, at the biological conditions most relevant to thrips (Re_b =10^{-2} and G/D=11), the drag required to fling two bristled wings was only 2 times greater than a single wing translating, compared to a 10-fold increase in drag for a solid wing at the same Re_b.

My results show that bristles significantly decreased the drag required to 'fling' wings apart compared to a solid wing (**Fig. 4.15**). **Table 4.3** shows the fraction of the drag produced by a single wing, compared to a solid wing, engaged in steady translation at the same Re_b. These results show that as G/D increased, the drag decreased. As the Re_b decreased, the bristled wing started to act more like a solid wing. **Table 4.4** shows the fraction of the peak drag produced by two bristled wings, compared to two solid wings, engaged in "fling". Bristles significantly reduced the drag required to fling two wings apart, even at lower Re_b.

Table 4.3. Fraction of drag produced by a single bristled wing translating compared to a solid wing (angle of attack=90°).

	Gap-to-diameter ratio			
Re_b	17	11	5	Solid
10^{-1}	0.09	0.14	0.29	1
10^{-2}	0.31	0.39	0.48	1
10^{-3}	0.59	0.67	0.76	1

Table 4.4. Fraction of max drag produced by two bristled wings performing fling compared to two solid wings performing fling.

	Gap-to-diameter ratio			
Re_b	17	11	5	Solid
10^{-1}	0.03	0.05	0.14	1
10^{-2}	0.05	0.08	0.20	1
10^{-3}	0.06	0.09	0.20	1

Comparing **Tables 4.3** and **4.4** reveals significant differences between single wings and wing-wing interactions. At $Re_b = 10^{-3}$, a bristled wing with G/D=5 experienced 76% of the drag of a solid wing when engaged in steady translation, whereas a wing engaged in fling experienced only 20% of the drag of a solid wing. At the biological conditions of thrips ($Re_b=10^{-2}$, G/D=11), the max drag required to fling two solid wings apart was 12 times greater than the drag required to fling two bristled wings. Whereas, the drag during steady translation was only 2.5 times greater for a solid wing than a bristled wing.

Single bristled wings may act even more like solid plates than is suggested by **Table 4.3** if they are translating at an angle of attack < 90. **Fig. 4.10** shows that the decrease in force with increasing G/D ratio was greater at higher angles of attack than at lower angles of attack, suggesting that bristled wings may act more like solid wings at lower angles of attack than they do at higher angles of attack. Furthermore, the spacing between bristles appeared to have little effect on the lift-to-drag ratio (**Fig. 4.11.b**) for a single wing translating.

These results support the idea that bristles may offer an aerodynamic benefit during clap and fling in tiny insects. My results showed that bristles significantly reduce the force required to fling the wings apart, compared to a solid wing. Although this study only considered “fling”, I expect that bristles have a similar force-reducing effect during the “clap” portion of the stroke. The idea that bristles offer an aerodynamic benefit during clap and fling is supported by a numerical study of porous wings, which showed that porous wings, compared with solid wings, reduce the drag required to move two wings apart (Santhanakrishnan, Robinson et al. 2014). My results show that bristles reduce the force experienced by a wing to a greater extent during fling than during steady translation. Following fling, the force approaches that experienced by a single

wing. Additionally, it could be possible for the bristled wing to preserve lift by acting more like a solid plate during the translational part of the stroke, especially if the angle of attack is < 90°.

4.5 Limitations.

While this study was conducted using 2D cross sections of infinitely long bristles, I expect that the 3D geometry and length of insect wing bristles will play an important role in their leakiness. I expect that the leakiness of bristles in 3D would be lower than the leakiness in 2D: rather than flowing between bristles, fluid may flow around the bristles in 3D. Cheer et al. demonstrated differences in the leakiness of the lower and upper part of fish rakers, so we may expect leakiness to vary with distance from the solid portion of the wing (Cheer, Cheung et al. 2012). Another limitation to the 2D study is that the bristles are modeled as an array of cylinders that are parallel to the long axis of the wing (**Fig. 4.21a**). The actual wings have bristles that point forward and backward, in addition to pointing laterally at the tip (**Fig. 4.21b**). This simplification may have major implications for the results, particularly in the study on the role of angle of attack. For example, the bristles that face forward and backward will not experience the same change in the angle of oncoming flow that the bristles at the tip of the wing do. Similarly, the velocity at the base of the wing will be lower than the velocity at the tip, which will change the leakiness and force. Three dimensional studies of a bristled wing would be an important next step to understanding the aerodynamics of bristles.

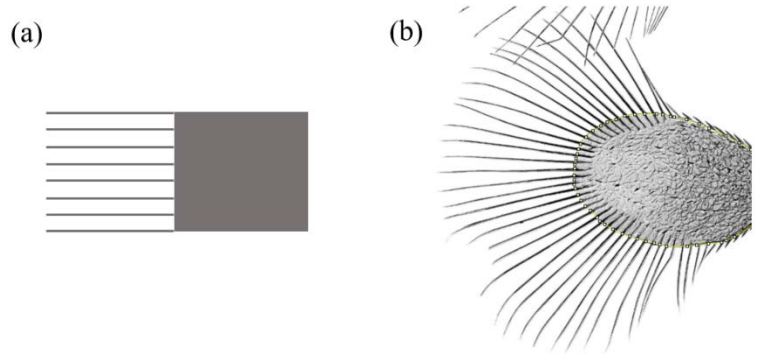

Figure 4.21. Modeling the bristles in 2D simplifies the orientation of the bristles. The 2D model assumed that the bristles were an array (a) that was parallel to the long axis of the wing, but the bristles on actual wings (b) point forward and backward at the base and laterally at the tip.

In this study, the distance between the wings at the start of fling was not varied: the wings started at 0.1 wing lengths apart. Kolomenskiy et al. demonstrated that lift is enhanced as the distance between wings approaches zero (Kolomenskiy, Moffatt et al. 2010, Kolomenskiy, Moffatt et al. 2011). However, observations of clap and fling in thrips has shown that the distance between the wings at the beginning of fling varies from about 1/4 to 1/10 of the chord length (Santhanakrishnan, Robinson et al. 2014).

I also expect that the flexibility will play a role in bristle performance—flexibility of biological structures has been demonstrated to reduce drag in a number of studies (Koehl 1984, Vogel 1989, Etnier and Vogel 2000, Alben, Shelley et al. 2002, Alben, Shelley et al. 2004, Miller, Santhanakrishnan et al. 2012). For example, when two hairs are very close and are flexible, they behave as a single hair with half of the deflection of an individual hair (Heys, Gedeon et al. 2008). Ferner and Gaylord showed that deformation of bristled appendages may result in a reduction in leakiness across a range of low Re_b (Ferner and Gaylord 2008).

CHAPTER 5: COMPUTATIONAL FLUID DYNAMICS OF A THREE-DIMENSIONAL WING AT LOW REYNOLDS NUMBERS

5.1 Introduction

Although a large body of work has examined the three-dimensional flow and forces around insect wings, most studies of insect flight have focused on insects at Re>100. Similarly, computational fluid dynamic studies of insect flight at the lowest Re have generally been conducted in two-dimensions (Miller and Peskin 2004, Wang 2004, Wang, Birch et al. 2004, Miller and Peskin 2005, Miller and Peskin 2009, Kolomenskiy, Moffatt et al. 2010, Arora, Gupta et al. 2014, Santhanakrishnan, Robinson et al. 2014). However, two-dimensional studies fail to capture the effects of spanwise flow and other three-dimensional effects. Previous research has shown that there can be differences between the results of two-dimensional and three-dimensional studies. For example, differences can exist in the separation of the leading edge vortex, especially at higher Re (Wang, Birch et al. 2004). For these reasons, it is important to consider the three-dimensional flow and forces when investigating insect flight.

Collaborators in Laura Miller's group and Michael Dickinson's groups experimentally investigated the forces and flow structures around a dynamically scaled physical model of an insect wing (Birch, Dickson et al. 2004, Wang, Birch et al. 2004, Lentink and Dickinson 2009). To complement the study, I completed a three-dimensional study of the forces and flow structures around a numerical insect wing of the same dimensions and engaged in the same kinematics. A three-dimensional numerical study can provide additional insights that enhance an experimental study. The PIV performed on the physical model is limited to capturing the flow

structures in a two-dimensional slice through the fluid domain, whereas a three-dimensional numerical study can capture the three-dimensional flow structures in the entire fluid domain. Using the computational model, I investigated the role of spanwise flow and other three-dimensional effects. I also compared the experimental and the computational models to increase the confidence in the results of the study.

In this study, I used a computational approach to investigate the effect of changing *Re* from 1 to 128 on the generation of aerodynamic forces and the flow structures of a three-dimensional elliptical wing. To date, this is the first study to quantify the flow structures around a three-dimensional wing at a range of angles of attack and at the *Re* range of the smallest flying insects (*Re*<10). Of particular interest, I compared the numerical results to those obtained by collaborators using a dynamically scaled physical wing model. I also investigated the effect of changing *Re* on spanwise flow, and I compared the aerodynamic forces generated at this range to the *Re* of larger insects, such as a fruit fly (*Re*~100).

5.2 Methods

5.2.1 Computational wing.

I modeled the wing to mimic a dynamically scaled robotic fly wing called the "Robofly" (Dickinson et al. 1999, Sane and Dickinson 2001, Birch and Dickinson 2003). The robot consists of a model wing attached to a coaxial arm, immersed in a 1 m x 1 m x 2 m tank filled with oil. Computer driven servo-motors control the orientation and movement of the wing, while force sensors record the lift and drag experienced by the wing. Collaborators for this project investigated the flow structures around a wing at *Re* ranging from 4 to 130 using particle image velocimetry (PIV), and recorded the forces experienced by the wing at various angles of attack (aoa).

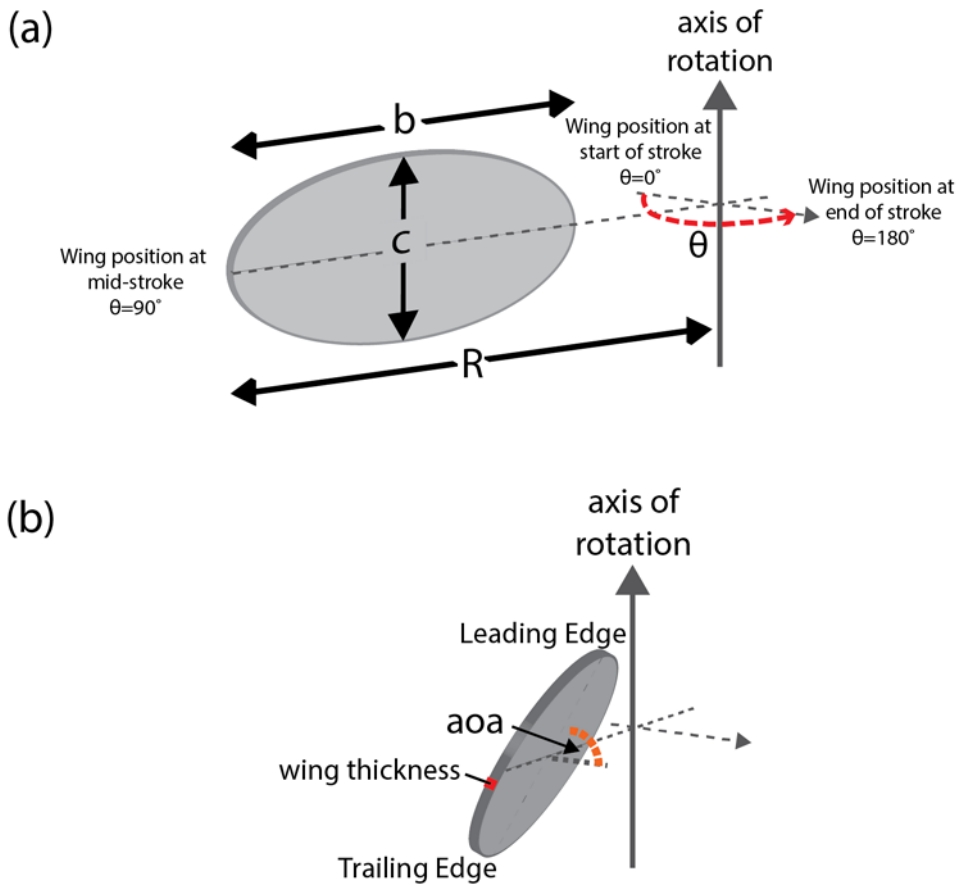

Figure 5.1. The three-dimensional elliptical wing (a) was based on the dimensions of a dynamically scaled robotic fly (c = 8.25 cm, b = 16.5 cm, R = 20.11 cm, and the wing was 2.0 mm thick). The wing was prescribed to move through a 180 degree arc at a fixed angle of attack. (b) The angle of attack (aoa) of the wing was varied from 0° to 90° degrees. Flow structures in following figures were captured when the wing position was at mid-stroke (θ=90°).

The computational wing (**Fig. 5.1**) did not have a force sensor or drive shaft, but otherwise had the same dimensions and prescribed motion as the experimental scaled model wing. Specifically, the wing consisted of an elliptical wing mesh based on the dimensions of the Robofly: c = 8.25 cm, b = 16.5 cm, R = 20.11 cm, and the wing was 2.0 mm thick. The wing was immersed in a 1 m x 1 m x 1 m fluid domain. The angle of attack (aoa) of the wing was varied from 0° to 90°. The kinematic pattern consisted of a single wing revolving through a 180° arc with constant angular velocity and a fixed angle of attack. Constant acceleration and deceleration

were used to start and end the stroke, respectively. The duration of the acceleration and deceleration was 10% of the stroke duration. Three-dimensional flow structures were investigated when the wing was at mid-stroke (θ =90°), and the forces were averaged over the steady part of the stroke.

Re was calculated for the wing as follows:

$$Re = \frac{\bar{\omega} R c \rho}{\mu} \qquad \text{Eq. 5.1}$$

where $\bar{\omega}$ is the angular velocity of wing revolution during the steady portion of the revolution, R is the wingtip radius, c is the chord length, ρ is the fluid density, and μ is the dynamic viscosity of the fluid. *Re* was varied in the computational model by changing μ while holding all other parameters constant.

5.2.2 Numerical method.

I used the IBFE method as described in Chapter 2.1.2 to model a three-dimensional revolving wing immersed in a viscous, incompressible fluid. The computational wing mesh was constructed using the dimensions described in Section 5.2.1 using Gmsh (Geuzaine and Remacle 2009) and consisted of 1994 tetrahedral elements with at least two elements across the wing thickness. The computational domain was 12 chord lengths in each direction and the wing tip was at least 4 chord lengths from the edges of the computational domain at all times.

I used IBAMR (Griffith, Hornung et al. 2007), as described in Chapter 2, for all of the fluid dynamic simulations. The adaptive method used four grid levels to discretize the Eulerian equations with a refinement ratio of four between levels. Regions of fluid that contained the bristles or vorticity above 0.125 were discretized at the highest refinement. The effective resolution of the finest level of the grid corresponded to that of a uniform 256^3 discretization. The boundary conditions were set to no-slip (**u**=0) on all sides of the computational domain. The wing was moved

using a preferred position that was changed in time. A penalty force was applied proportional to the distance between the actual and desired boundaries. Other simulation-specific numerical parameters are listed in **Table 5.1**.

Table 5.1. Numerical parameters.

Dimensionless parameter	**Value**
Chord length	0.0825
Span length	0.165
Radius of wingtip	0.2011
Sweep distance (degrees)	180
Final simulation time	1
Acceleration time	0.1
Deceleration time	0.1
Domain length (L)	1
Finest Grid Refinement	256^3
Number of refinement levels	4
Refinement ratio	1:4
Time step (dt)	1.0e-5
Spatial step size (dx)	L/256
Stiffness (kappa_s)	1e14

5.2.3 Grid convergence study.

To test for spatial convergence, I compared a uniform 256^3 discretization to a uniform 512^3 discretization. These two resolutions were compared using aoa=45° and *Re* ranging from 1 to 128. The average dimensionless lift and drag coefficients over the steady part of the stroke are shown in **Fig. 5.2**. The average percent difference in force between the 256^3 grid and the 512^3 grid was $\leq$3% for lift and $\leq$7% for drag. For computational efficiency, effective 256^3 grid discretization was used for all remaining simulations in this chapter.

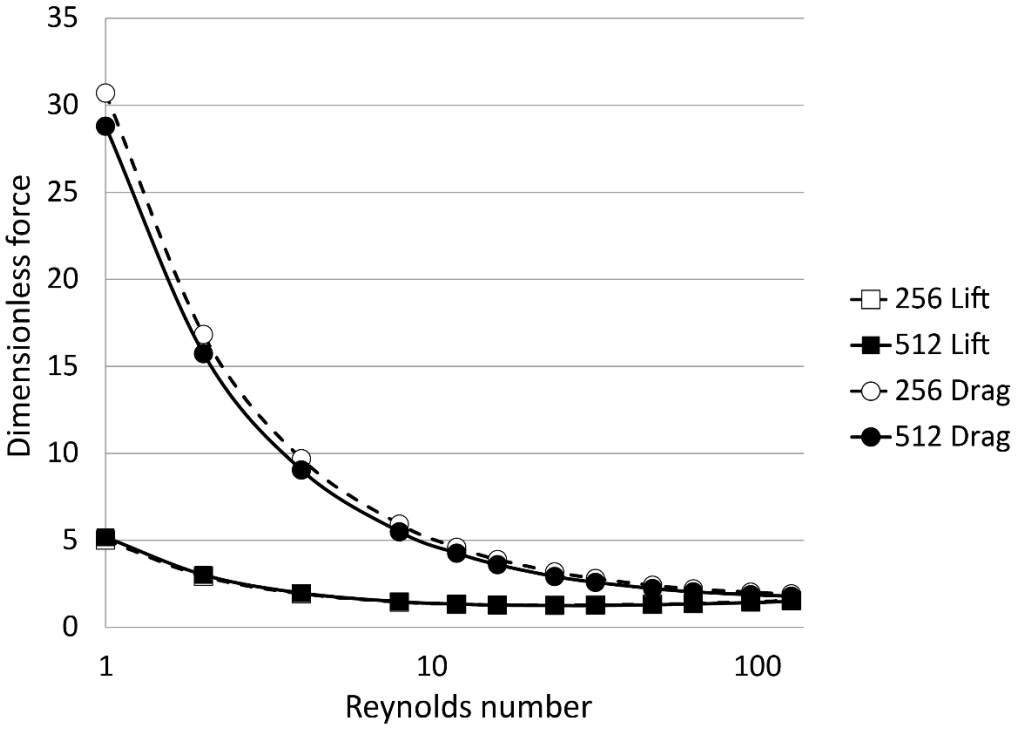

Figure 5.2. Refinement study comparing average dimensionless lift and drag over a range of *Re* at 256^3 and 512^3 grid discretization. Average dimensionless force was calculated over the steady part of the stroke. Effective 256^3 grid discretization was used for all other simulations in this study.

5.3 Results

5.3.1 Forces around a revolving 3D wing at low Reynolds numbers

The time-averaged lift and drag coefficients for the revolving physical and numerical model wings as functions of the angle of attack are shown in **Fig. 5.3** across three values of *Re*. The forces were sampled for 11 values of angle of attack for the computational model and 21 values of angle of attack in the experimental model in the range of 0° to 90°. In general, there was good agreement between the computational and experimental models. The drag measured for the numerical model was higher than the drag measured for the physical model at lower *Re* (**Fig. 5.3b**). The *Re* of the physical model was varied by changing the angular velocity of the

wing. At the lowest *Re*, very slow velocities were required, and this may have impacted the accuracy of the results of the physical model.

The behavior seen for *Re* = 130 was consistent with previously published results on a three-dimensional flapping wing at *Re* pertinent to fruit flies (Dickinson, Lehmann et al. 1999, Wang, Birch et al. 2004, Lentink and Dickinson 2009). And the overall relationship between force coefficients and angles of attack supported previous studies (Dickinson and Gotz 1993, Wang, Birch et al. 2004).

In general, as the *Re* decreased, the force coefficients increased. This effect was stronger for drag than for lift. Drag coefficients increased with increasing angle of attack. Note that the drag was nonzero at a 0° angle of attack due to the non-negligible viscous forces. The maximum value of lift coefficient occurred at an angle of attack of 45° for all values of *Re*. The drag coefficient increased significantly with decreasing *Re* as compared to the slight increase in values of lift coefficient with decreasing *Re*. Both the computational and experimental results showed the same trends in forces generated as a function of *Re* and angle of attack. The drag in the numerical simulations was larger than the experiments for lower *Re*.

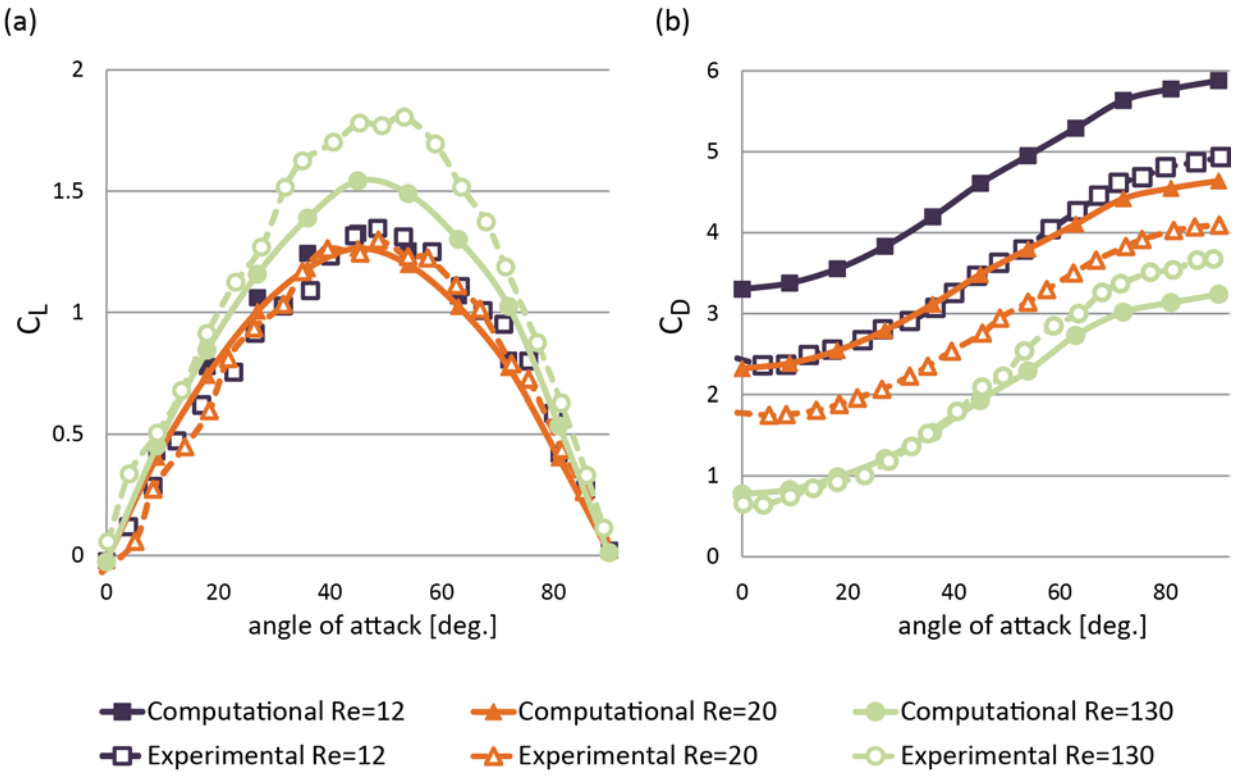

Figure 5.3. Comparison of (A) lift and (B) drag for computational and experimental models over a range of angles of attack.

A careful examination of the effect of changing *Re* on the lift and drag coefficients revealed differences in the aerodynamics of tiny insects, such as thrips, compared with larger insects, such as fruit flies. The aerodynamic performance comparison shown in **Fig. 5.4** corresponds to the steady motion of a revolving model wing at a fixed angle of attack of 45°, a value that is typically observed during most of the downstroke in the flapping translation of flying insects (Sane 2003). Overall, there was good agreement between the computational and the experimental results. The average difference between the experimental and computational lift was <10% and the difference between the experimental and computational drag was <20%. In the lower *Re* end, applicable to thrips flight, there was a marked doubling in the values of drag coefficients, which has been seen in previous numerical studies (Miller and Peskin 2004). At

such low *Re*, viscous effects in the flow are highly pronounced as compared to inertial forces. The onset of the transition to highly elevated drag coefficients occurred near *Re* = 30 (**Fig. 5.4**). **Fig. 5.5** shows the ratio of lift to drag over a range of *Re*.

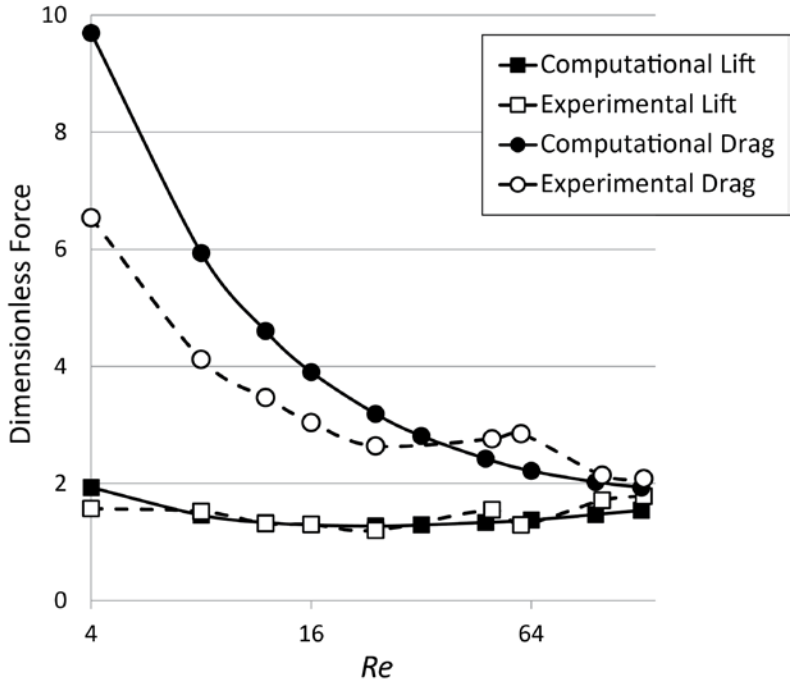

Figure 5.4. Comparison of computational model to experimental model (aoa=45°). Average dimensionless lift and drag was calculated over the steady part of the stroke.

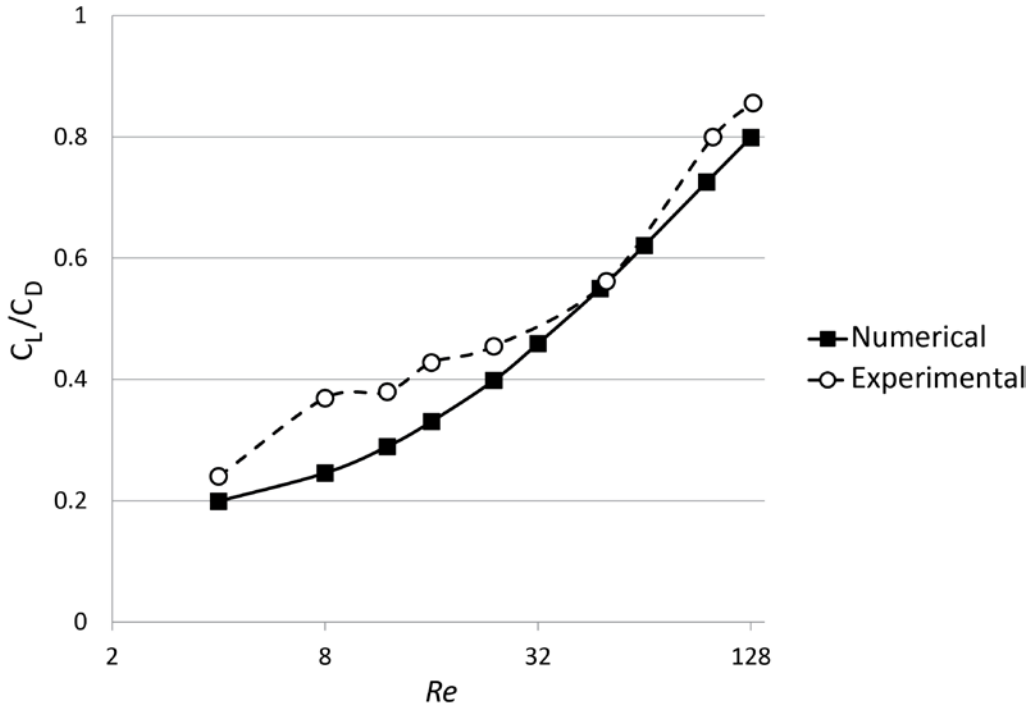

Figure 5.5. Lift/drag coefficient for the computational and experimental models over a range of *Re* (aoa=45°).

Fig. 5.6a shows the aerodynamic polar plots for the lower *Re* (12-20). Notice that while peak lift coefficient remained relatively constant, the entire polar plot shifted to the right with decreasing *Re*. This illustrates the sensitivity of the drag coefficient to *Re* at all angles of attack. **Fig. 5.6b** shows the aerodynamic polars for higher *Re* (50-130). The aerodynamic polar for *Re*=100 was in good agreement with previous experimental models at *Re*=110 (Lentink and Dickinson 2009) and *Re*=120 (Birch, Dickson et al. 2004). The lift coefficient did slightly increase at high *Re*, and the graph shifted to the left as *Re* increases (see **Fig. 5.7** for additional aerodynamic polars and **Fig 5.8** for a plot of the ratio of lift-to-drag over a range of angles of attack). Overall, these observations suggest that there are drastic differences in the aerodynamics of flight at the scale of the smallest insects as compared with larger insects.

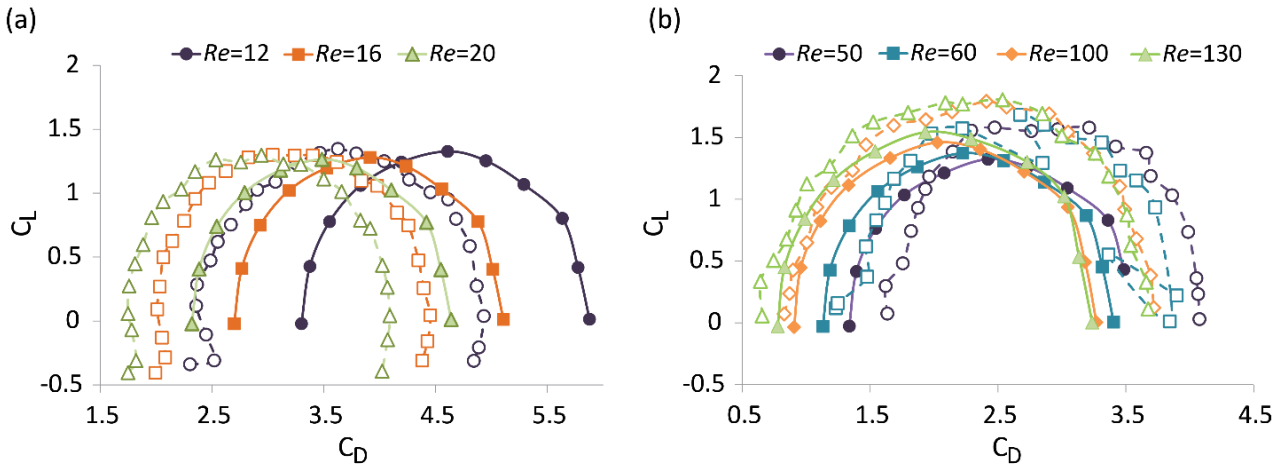

Figure 5.6. Comparison of computational model (solid markers) and experimental model (open markers) at (a) lower *Re* range and (b) higher *Re* range.

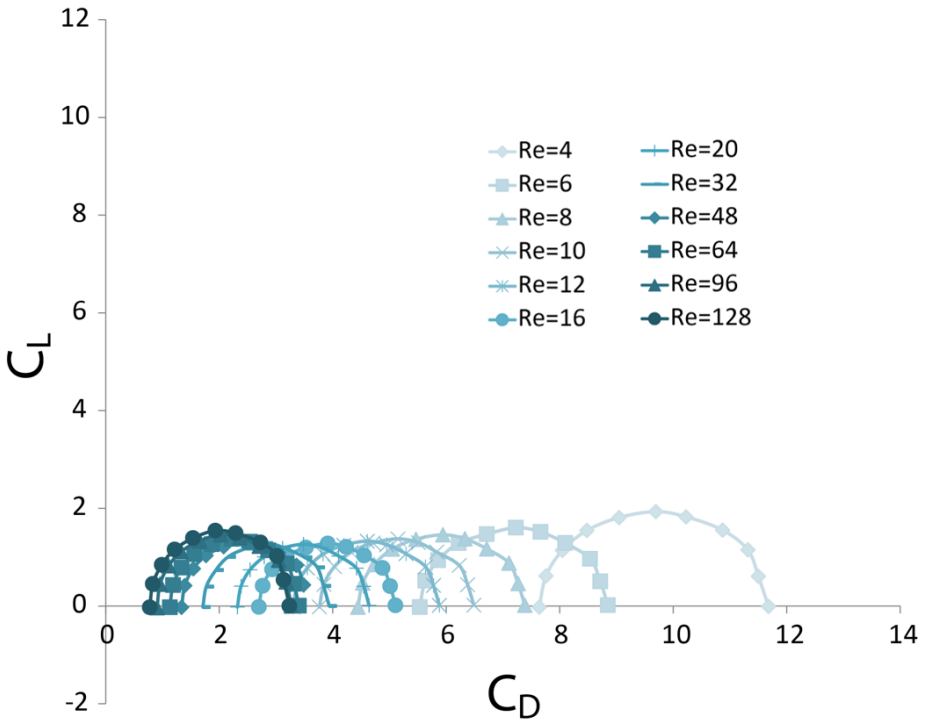

Figure 5.7. Plot of average dimensionless lift vs average dimensionless drag for the computational model over a range of *Re*. In all cases, peak lift occurs at angle of attack of 45°.

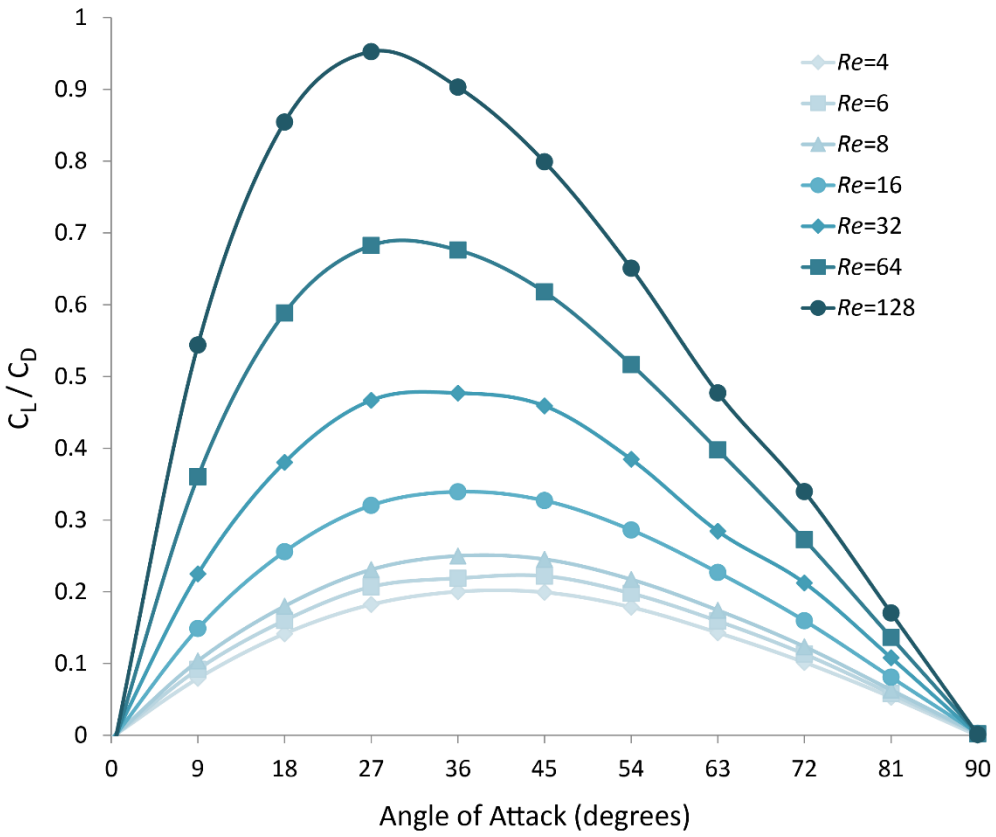

Figure 5.8. Plot of the ratio of lift-to-drag vs angle of attack for the computational model over a range of *Re*.

5.3.2 Flow structures at low Reynolds numbers

The effect of changing *Re* on the flow structure around the wing can be examined from the streamlines plotted for the computational wing (**Fig. 5.9**). The wing was revolved at a fixed angle of attack of 45° for 1<*Re*<128, and the flow field shown in these figures corresponds to the instant when the wing had swept a 90˚ arc from starting at rest. The streamlines are instantaneous curves that begin at seed locations along the leading edge of the wing and are tangential to the local fluid velocity at every point in the vector field. Each streamline was computed by a Runge-Kutta based numerical integration of the seed location through the vector field.

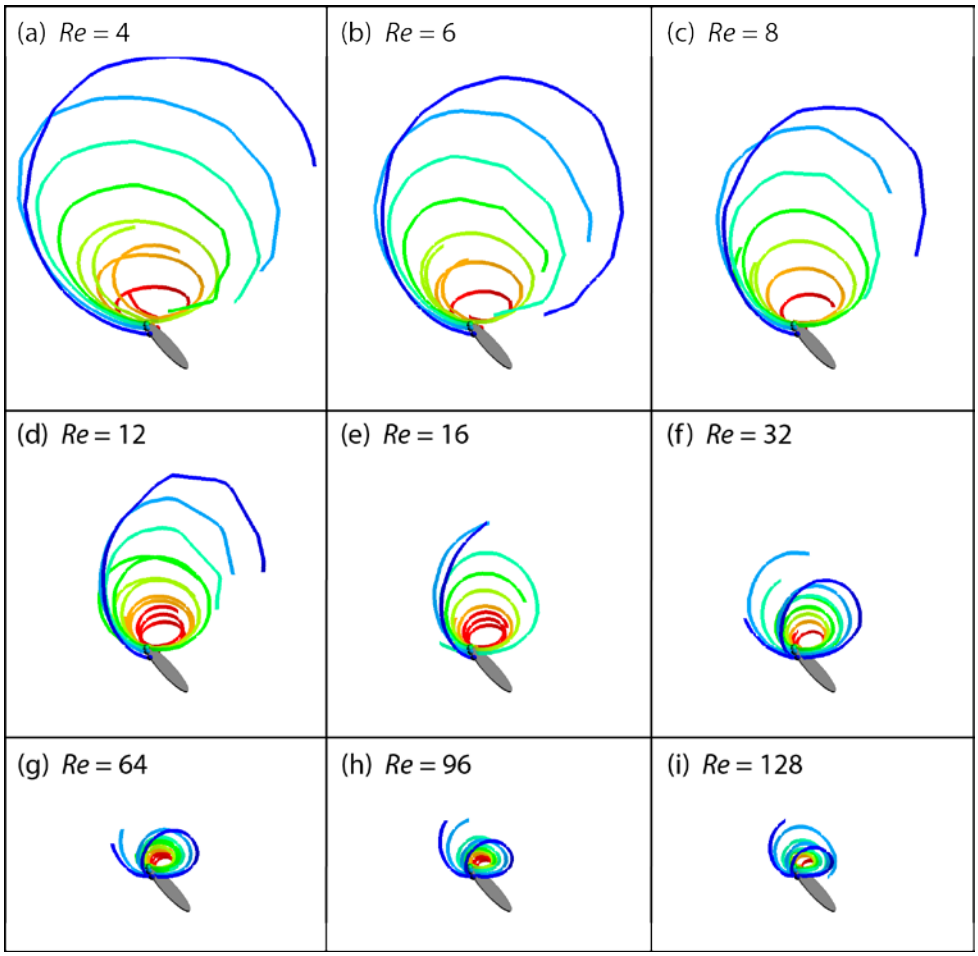

Figure 5.9. Streamlines around the wing at mid-stroke (aoa=45, *Re* range from 4-128). Seven streamlines are evenly spaced along the leading edge. Streamlines are color-coded to indicate starting position. The streamline closest to the camera (blue) is furthest from the axis of rotation. Note that the wing is traveling to the left.

For a revolving model insect wing at *Re*=128, closer to the dynamic scale of fruit flies, an attached LEV was observed at mid-stroke when the wing had traversed a quarter circle (**Fig. 5.9i** and **5.10i**). At the start of motion, the TEV that formed on account of vorticity conservation was shed in the wake and was no longer attached to the trailing edge of the wing at mid-stroke. An attached LEV and shed TEV have been seen previously at *Re* pertinent to fruit flies and higher (Ellington, Van Den Berg et al. 1996, Dickinson, Lehmann et al. 1999, Birch, Dickson et al. 2004, Wang, Birch et al. 2004). The attached LEV is primarily responsible for delayed stall and

enhanced lift generation (Dickinson, Lehmann et al. 1999). Furthermore, the asymmetric attached LEV and shed TEV structure of the flow around the wing has been shown in several insect flight studies to result in higher lift forces (Ellington, Van Den Berg et al. 1996, Birch and Dickinson 2001, Miller and Peskin 2004). The LEV, if formed, remained attached to the wing throughout the range of *Re* considered. The computational results showed that the TEV moved closer to the wing with decreasing *Re* (**Fig. 5.10**).

At a *Re* range of 4-32, which is representative of the range of flight experienced by the smallest insects, both the LEV and TEV did not separate from the wing (**Figs. 5.10a-f**). The TEV was not shed into the wake at this range of *Re* due to the increased viscous forces present in the flow field that stabilize the vortex. This 'vortical symmetry' is in agreement with numerical results of Miller and Peskin for 2D wings (2004). With decreasing *Re* and correspondingly reduced kinetic energy of the flow, both the LEV and TEV were more diffuse. The lack of separation of the TEV resulted in an overall reduction in the bound circulation around the wing.

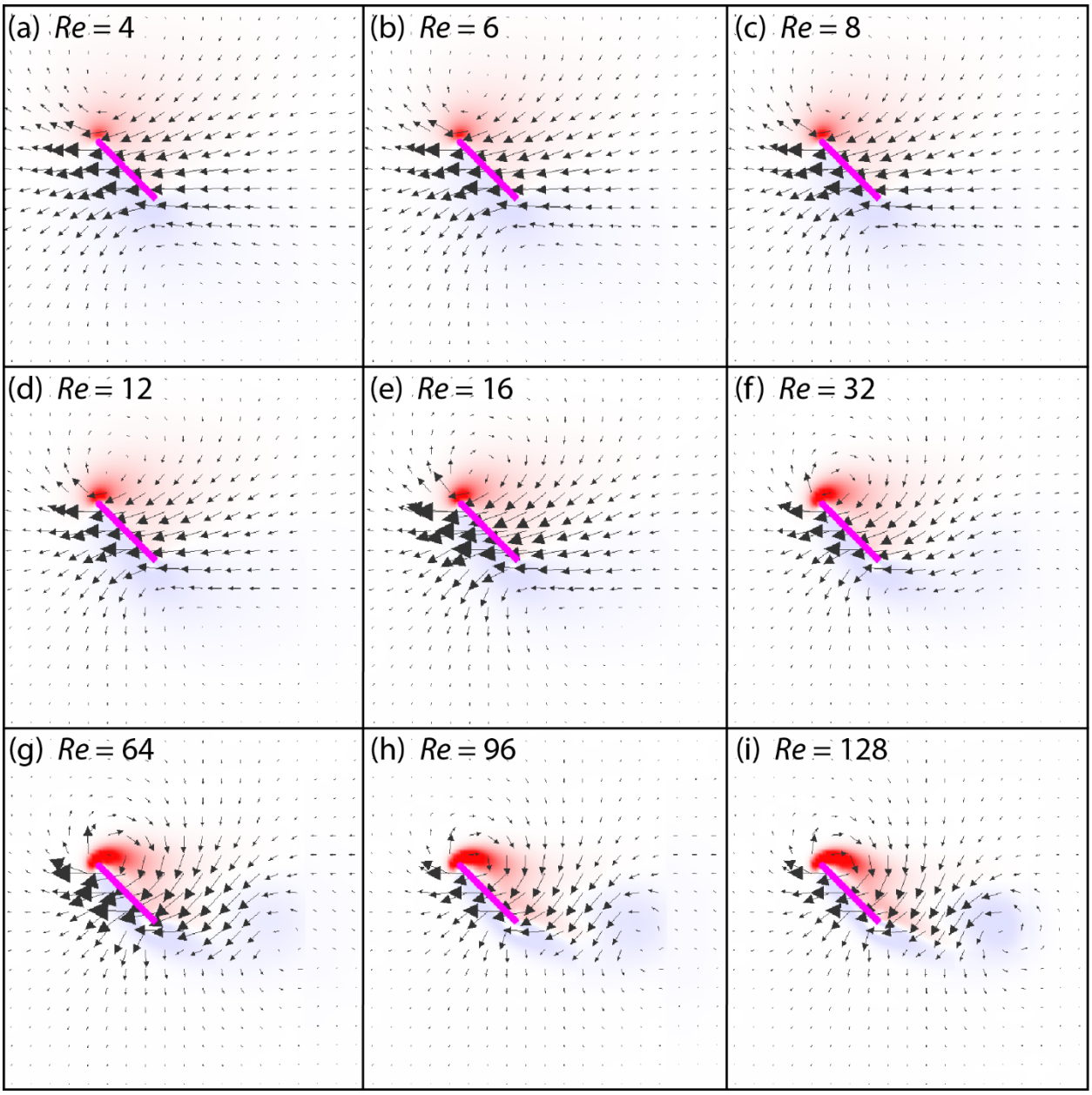

Figure 5.10. Vorticity plots for aoa=45° at a range of *Re*. Cross section shown is through the chord at the midpoint of the span, midway through the stroke. The vectors show the direction of flow and are scaled to the magnitude of the flow velocity. The color map shows the vorticity of the fluid (min=-30 and max=30). Note that the wing is traveling to the left.

5.3.3 Spanwise flow

An advantage of performing 3D computational studies is that we can readily obtain detailed information on spanwise flow and 3D flow structures. **Fig. 5.11** shows a top-down view of a pseudocolor plot of the spanwise flow through a slice just above the wing. In **Fig. 5.12**, 2D velocity vectors are shown in a plane that cuts through a cross section of the wing. A pseudocolor plot of the spanwise velocity (in the direction normal to the plane) is also provided to illustrate the three-dimensionality of the flow. At *Re*=4 (**Fig. 5.11A** and **Fig. 5.12A**), spanwise flow occurred over a broad region behind the wing. As the *Re* increased, the magnitude of the spanwise flow increased, and the region of non-negligible spanwise flow became smaller. **Fig. 5.12** also shows that the shape of the region of spanwise flow became more elongated as *Re* increases. The size and shape of the region of spanwise flow at *Re*=128 matched a previous experimental study at *Re*=120 (Birch, Dickson et al. 2004) and a computational study at *Re*=120 (Harbig, Sheridan et al. 2013).

Figs. 5.11 and **5.12** show that maximum spanwise flow occurred farther behind the wing as the *Re* decreased. This is in agreement with the results of a previous experimental study (Birch, Dickson et al. 2004) which found similar results comparing *Re*=120 and *Re*=1400, and the results of a computational study (Harbig, Sheridan et al. 2013) which found similar results comparing *Re*=120 and *Re*=1500. **Fig. 5.12** further shows that there was little spanwise flow in the LEV at *Re*<128, which is supported by previous experimental studies (Birch, Dickson et al. 2004, Lentink and Dickinson 2009, Harbig, Sheridan et al. 2013). In a numerical study, Aono et al. (2008) showed that spanwise flow was primarily confined to the core of the LEV at *Re*=6300, but little spanwise flow existed in the LEV at *Re*=134.

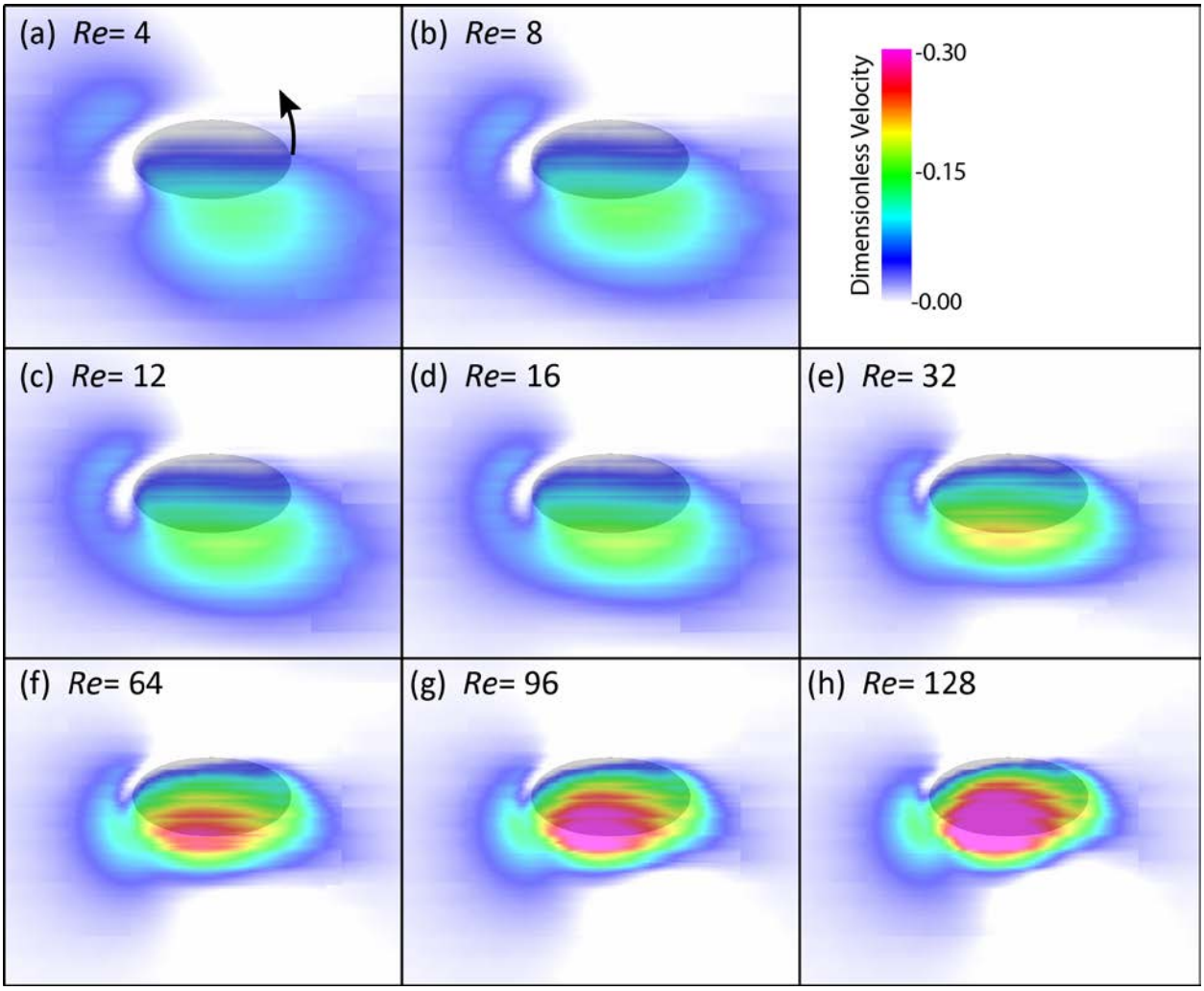

Figure 5.11. Spanwise flow above the wing at mid-stroke (aoa=45°, *Re* range from 4-128). The color map shows the spanwise flow through a slice parallel to the wing and 1/10 chord length above the wing (min=0 and max=0.3). Note that the wing is traveling counterclockwise, indicated by the arrow in (a), about an axis of rotation to the left.

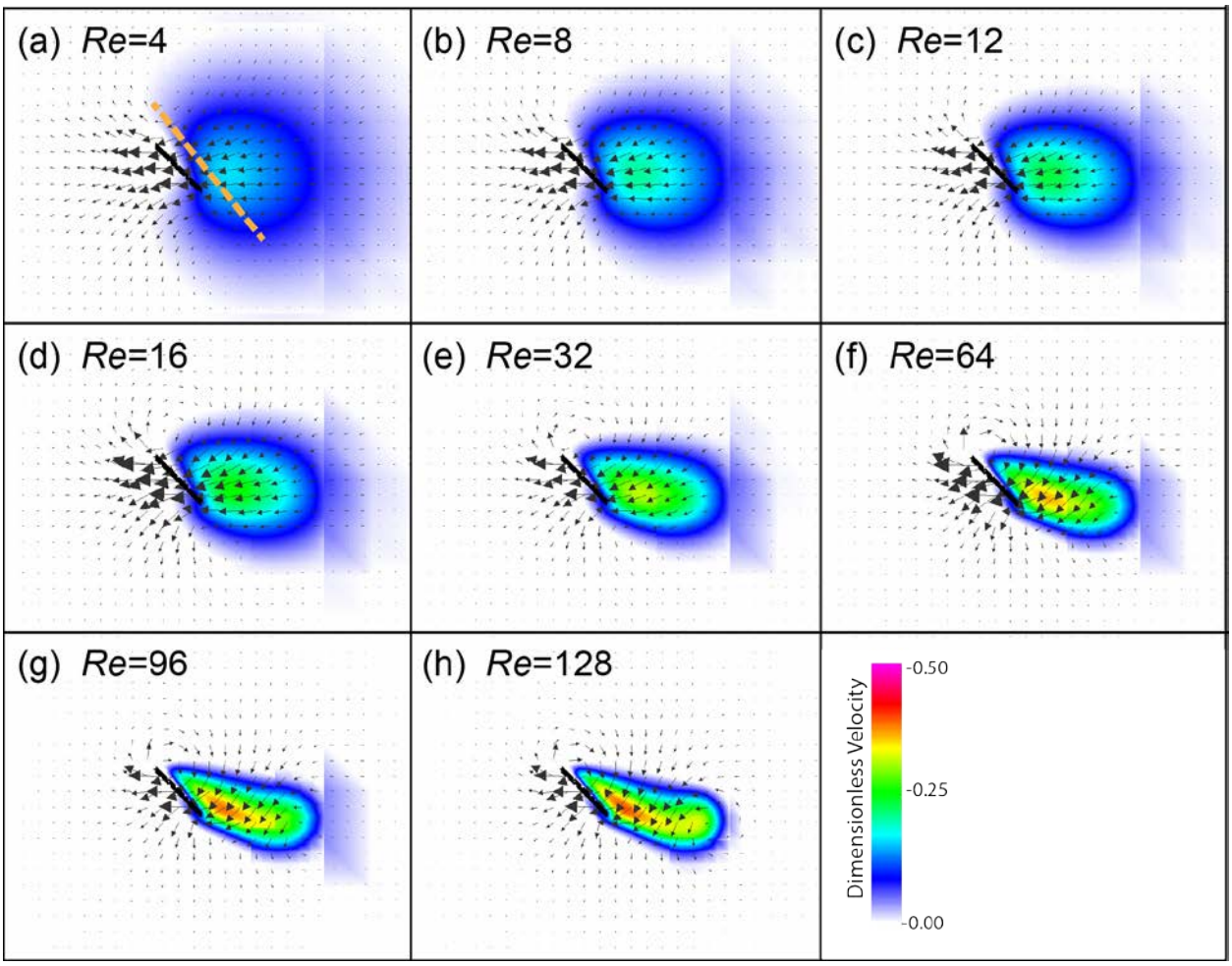

Figure 5.12. Vector fields and spanwise flow at mid-stroke (aoa=45°, *Re* range from 4-128). Cross section shown is through the chord at the midpoint of the span. The vectors show the direction of flow and are scaled to the magnitude of the flow velocity. The color map shows the spanwise flow (min=0 and max=0.5). Note that the wing is traveling to the left. Average spanwise flow was calculated along the dashed transect in (a), and is shown in **Fig. 5.13.**

Fig. 5.13 shows the average spanwise flow for a range of *Re* (aoa=45°) calculated along the dashed transect shown in **Fig. 5.12A**. Average spanwise flow increased with increasing *Re*, which has been observed previously at *Re*>100 (Birch, Dickson et al. 2004, Aono, Liang et al. 2008, Harbig, Sheridan et al. 2013). The dependence of the average spanwise flow on *Re* was the most sensitive for lower *Re*, particularly *Re*<20. For 40<*Re*<128, average spanwise flow increased linearly with *Re*. It is interesting to note that the most sensitive *Re* range also

corresponded to the scales at which the TEV did not separate from the wing and the drag coefficient became particularly sensitive to *Re*.

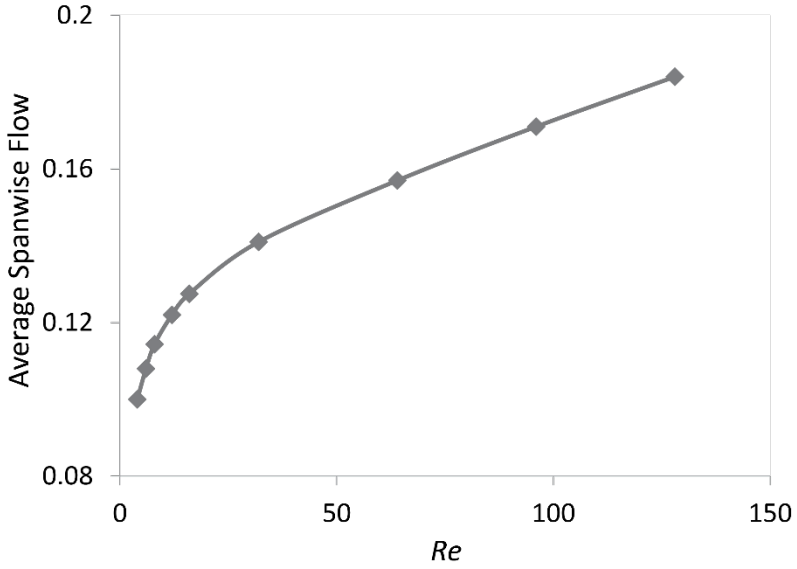

Figure 5.13. Average spanwise flow along the dashed transect shown in Fig. 5.11a as a function of *Re* (aoa=45).

I also investigated how small changes in the angle of attack affected the 3D flow structure at *Re*=4 (**Fig. 5.14**), *Re*=32 (**Fig. 5.15**), and *Re*=128 (**Fig. 5.16**). For all angles of attack, the spanwise flow increased and became less diffuse as the *Re* increased. As expected, the flow field structure was symmetric for both 0° and 90° angles of attack at all *Re*. As the angle of attack increased from 0° to 90°, the magnitude of the spanwise velocity also increased. The magnitude of this effect was greater at larger *Re*. At *Re*=4, the maximum spanwise flow increased by only 42% between 0° and 90° angles of attack, whereas at *Re*=128 the maximum spanwise flow increased by 200% between 0° and 90° angles of attack. The shape of the region of significant spanwise flow was the most sensitive to the angle of attack at higher *Re*. At *Re*=4,

there was little change in the shape of the region of spanwise flow as the angle of attack increased, whereas at *Re*=128, the shape of the region of spanwise flow was greatly influenced by the angle of attack. As the angle of attack increased from 0° (**Fig. 5.16a**) to 45° (**Fig. 5.16i**), the region of spanwise flow extended behind and below the wing. As the angle of attack increased from 45° to 90° (**Fig. 5.16j**), the region of spanwise flow became symmetric again, and no longer extended below the trailing edge of the wing.

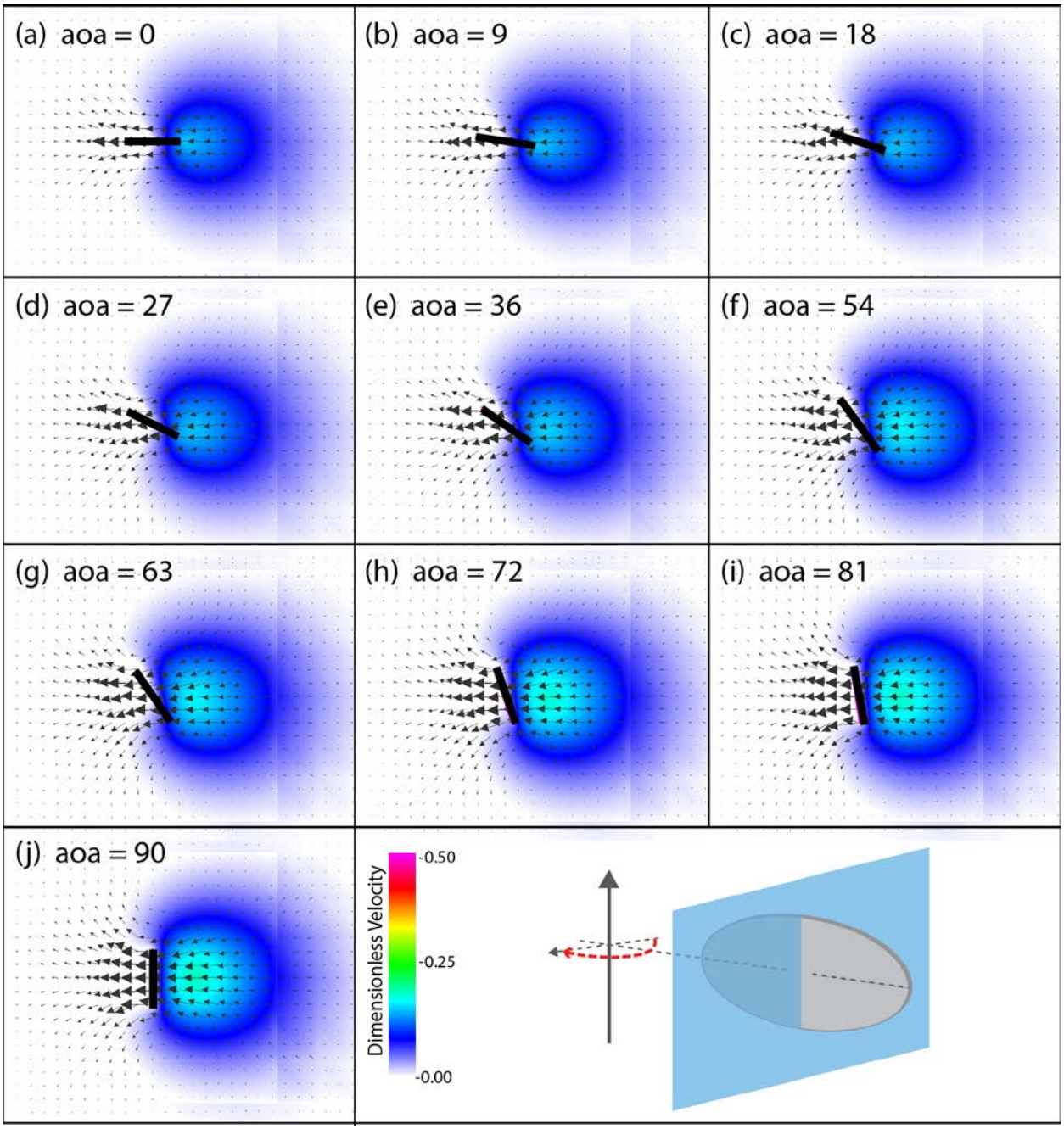

Figure 5.14. Vector fields and spanwise flow at mid-stroke (*Re* = 4, aoa range from 0° to 90°). Cross section shown is through the chord at the midpoint of the span. The vectors show the direction of flow and are scaled to the magnitude of the flow velocity. The color map shows the spanwise flow (min=0 and max=0.5). Note that the wing is traveling to the left.

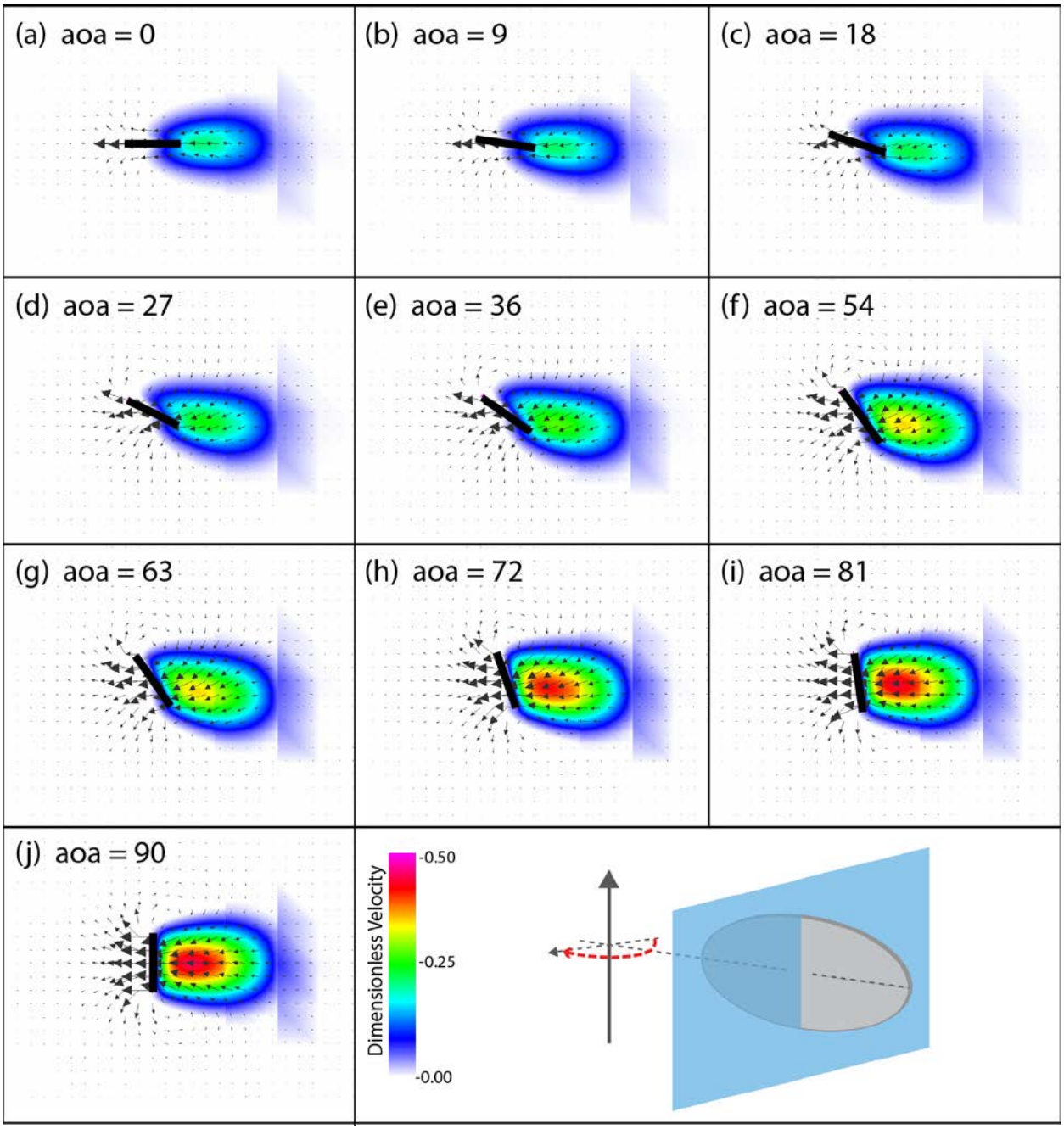

Figure 5.15. Vector fields and spanwise flow at mid-stroke (*Re* = 32, aoa range from 0° to 90°). Cross section shown is through the chord at the midpoint of the span. The vectors show the direction of flow and are scaled to the magnitude of the flow velocity. The color map shows the spanwise flow (min=0 and max=0.5). Note that the wing is traveling to the left.

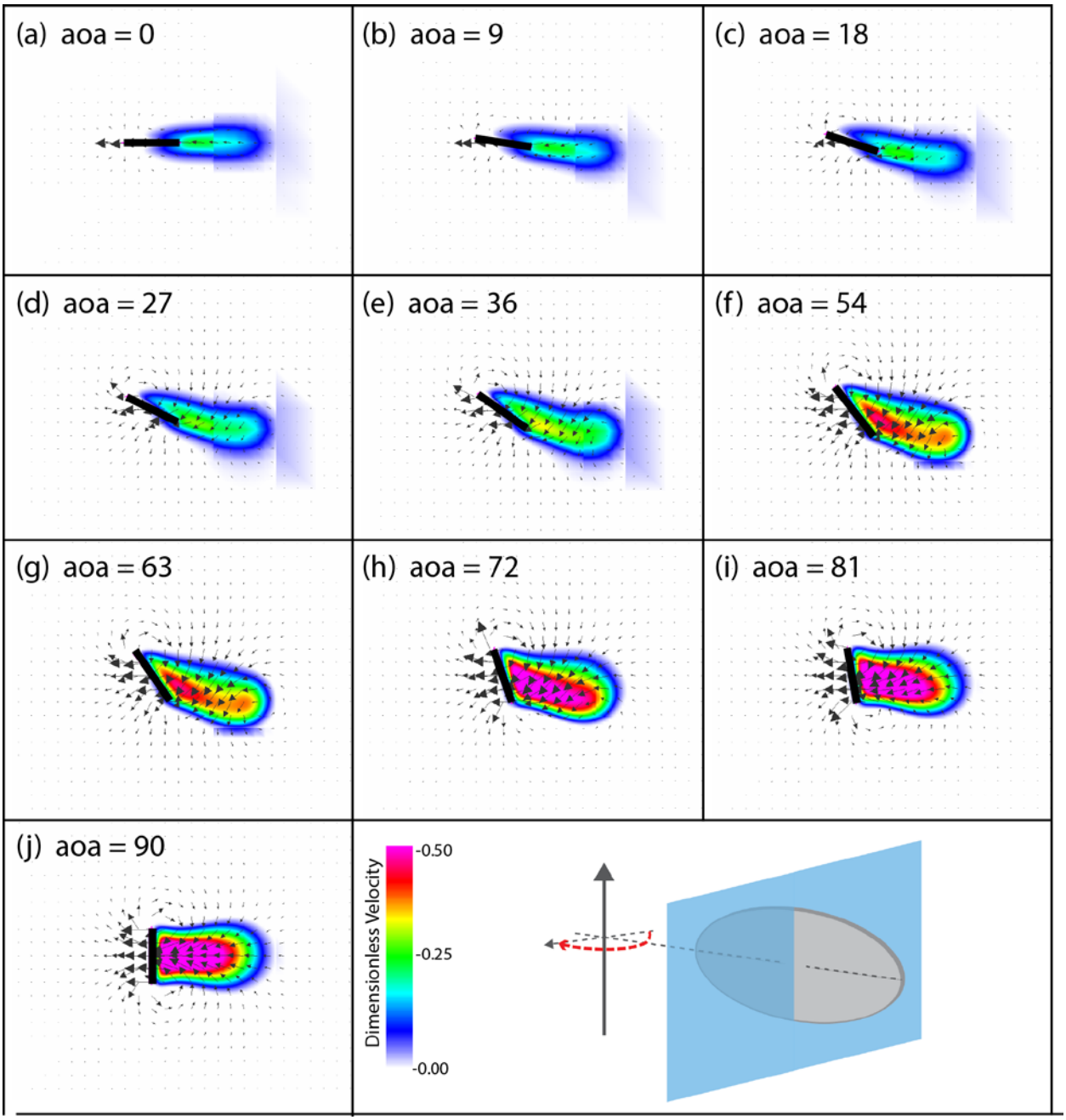

Figure 5.16. Vector fields and spanwise flow at mid-stroke (*Re* = 128, aoa range from 0° to 90°). Cross section shown is through the chord at the midpoint of the span. The vectors show the direction of flow and are scaled to the magnitude of the flow velocity. The color map shows the spanwise flow (min=0 and max=0.5). Note that the wing is traveling to the left.

5.4 Discussion

To better understand the flight of the smallest insects, I have performed a more complete study of three-dimensional aerodynamics at low *Re*. I analyzed the forces and flow structures around a three-dimensional numerical wing model at the *Re* relevant to the smallest flying insects. My results were in good agreement with a dynamically scaled physical model. A number of previous studies have investigated the forces and flow structures around a wing in 3D at low *Re* (Sun and Yu 2006, Liu and Aono 2009, Zheng, Hedrick et al. 2013), however most of these studies only considered a single *Re* below 100. For that reason, I investigated the flow structures and forces around a three-dimensional wing at a range of angles of attack and *Re* relevant to the smallest flying insects (*Re* ~ 4-100).

The results of this study showed that: (1) as *Re* decreased, drag increased significantly; (2) defined in terms of the average lift to drag coefficient, flight became increasingly less efficient as *Re* decreased; (3) at the range of flight experienced by the smallest insects ($4<Re<32$), both the LEV and TEV remain attached to the wing; and (4) spanwise flow decreased with decreasing *Re*, especially in the range of the smallest flying insects. Overall, these observations suggest that there are drastic differences in the aerodynamics of flight at the scale of the smallest flying insects, which makes their flight more challenging, compared with larger insects.

This study supports previous research that suggests that the aerodynamics of the smallest flying insects may be significantly different from that of larger insects (Weis-Fogh 1973, Ellington 1980, Wang 2000, Sunada, Takashima et al. 2002, Miller and Peskin 2004, Miller and Peskin 2005, Sun and Yu 2006, Miller and Peskin 2009, Kolomenskiy, Moffatt et al. 2010, Kolomenskiy, Moffatt et al. 2011, Santhanakrishnan, Robinson et al. 2014). In general, the

smallest flying insects face many aerodynamic challenges as a result of their size. Both lift and drag coefficients increased as *Re* decreases. However, the drag coefficient was most sensitive to changes in *Re*: drag increased significantly with decreasing *Re*, whereas there were only small changes in lift. At the scale of fruit flies (*Re*~100), the lift to drag ratio approached 1 as seen both here (**Fig. 5.5**) and elsewhere (Dickinson and Gotz 1993, Sane and Dickinson 2001, Wang 2004). Whereas, the lift to drag ratio approached 0.2 for the smallest insects such as fairyflies and haplothrips (*Re*<10).

The TEV and LEV remained attached to the wing at *Re*<32 (**Fig. 5.10**). As *Re* increased above 32, however, the TEV was shed from the wing. This vortical symmetry at lower *Re* has implications for the aerodynamics of the smallest flying insects. An asymmetric attached LEV and shed TEV has been shown to increase lift (Ellington 1999, Birch and Dickinson 2001, Miller and Peskin 2004). At an *Re* range of 4-32, which is representative of the range of flight experienced by the smallest insects, both the LEV and TEV did not separate from the wing due to the increased viscous forces present in the flow field that stabilize the vortex. With decreasing *Re*, the lack of separation of the TEV resulted in an overall reduction in the bound circulation around the wing, and consequently a decrease in lift. Additionally, due to the relative increase in viscous forces present in the flow for *Re* < 10, vorticity is expected to dissipate much faster. For the same reason, vorticity enhancement via 'wake capture' of circulation from the previous stroke (at stroke reversal) is also expected to be minimal for the *Re* range appropriate to flight of tiny insects; this arises from the fact that the strength of the wake at the end of a stroke will be relatively diminished at this range of *Re*.

Using the computational model, I investigated three-dimensional effects, such as spanwise flow. My results showed that as *Re* decreases, the magnitude of spanwise flow

decreased and the region of non-negligible spanwise flow occurred over a broader region behind the wing (**Fig. 5.12**). In larger insects, such as hawkmoths, the spanwise flow is concentrated in the LEV (Aono, Liang et al. 2008). My numerical results showed that there was little spanwise flow in the LEV at $Re<128$, which is in agreement with previous experimental studies (Birch, Dickson et al. 2004, Lentink and Dickinson 2009, Harbig, Sheridan et al. 2013) and numerical studies (Aono, Liang et al. 2008, Kolomenskiy, Moffatt et al. 2011). Interestingly, the shape of the region of non-negligible spanwise flow also changed with *Re*. At $Re=4$ (**Fig. 5.12a**), a cross section of the region of spanwise flow behind the wing was round and symmetrical. As the *Re* increased, however, the region became elongated and began to extend behind and below the wing. The shape of the region of spanwise flow at $Re=128$ (**Fig. 5.12h**) was in agreement with previous experimental studies (Birch, Dickson et al. 2004, Harbig, Sheridan et al. 2013).

My results showed that there is a significant decrease in the average spanwise flow with decreasing *Re*, especially in the range of the smallest flying insects (**Fig. 5.13**), which could have implications for the interpretation of 2D studies. A major difference between 2D computations and 3D insect wings is the presence of 3D effects, such as spanwise flow (Wang, Birch et al. 2004). This can lead to differences between the 2D and 3D results. For example, the LEV is shed after traveling a few chord lengths in 2D models (Dickinson and Gotz 1993, Miller and Peskin 2004), whereas the LEV remains stably attached to a revolving 3D wing for much longer distances (Dickinson, Lehmann et al. 1999, Wang, Birch et al. 2004). The patterns of vortex shedding in our study, however, were in good agreement with the numerical results of a 2D wing at low *Re* (Miller and Peskin 2004). This suggests that three-dimensional effects may play a less significant role in the flight of the smallest insects. And consequently, these results imply that 2D studies may be able to more accurately model small insect flight than large insect flight.

Overall, the results supported previous work which highlight some of the significant challenges faced by insects flying at low *Re* (Ellington 1980, Wang 2000, Miller and Peskin 2004, Miller and Peskin 2005, Sun and Yu 2006, Miller and Peskin 2009, Kolomenskiy, Moffatt et al. 2010, Kolomenskiy, Moffatt et al. 2011, Santhanakrishnan, Robinson et al. 2014). In particular, drag was enhanced and the lift to drag ratio was decreased during steady translation at low *Re*.

While this study quantified the flow structures and forces around a three-dimensional wing at a range of angles of attack and *Re* relevant to the smallest flying insects (*Re* ~ 4-128), I only considered the case of a single rigid wing engaged in steady translation. I did not consider more complicated kinematics or the effects of wing-wing interactions, such as clap and fling (Weis-Fogh 1973). Clap and fling has been observed in tiny insects such as *Encarsia formosa* (Weis-Fogh 1973) and thrips (Ellington 1984), and it is believed to enhance lift by the formation of a large attached LEV (Lighthill 1973, Maxworthy 1979, Ellington 1984, Ellington 1984, Spedding and Maxworthy 1986, Sun and Xin 2003, Lehmann, Sane et al. 2005, Miller and Peskin 2005, Sun and Yu 2006, Lehmann and Pick 2007, Miller and Peskin 2009). A 2D numerical study demonstrated that very large drag forces are required to fling the wings apart at *Re* relevant to the smallest flying insects (Miller and Peskin 2005), however that force is reduced when the wings are flexible (Miller and Peskin 2009). A logical future direction in the analysis of flight of the smallest insects would be an investigation of the three-dimensional forces and flow structures around flexible wings engaged in clap and fling at the *Re* relevant to tiny insects.

CHAPTER 6: CONCLUSIONS

6.1 Conclusions

I used computational fluid dynamics to better understand the challenges of flight at the scale of the smallest flying insects and investigated possible mechanisms to overcome these challenges. Because of their small size and high wing beat frequency, detailed quantitative data on the wing kinematics of the smallest insects is not readily available. As a result, there has been much debate and speculation about the flight strategies employed by these insects. Using the immersed boundary method and a hybrid finite difference/finite element immersed boundary method, I developed both two-dimensional and three-dimensional models of small insect wings to gain insight into the aerodynamics of flight at this scale.

In Chapter 3, I investigated whether lift- or drag-based mechanisms produce the most vertical force at the Reynolds numbers relevant to tiny insects. I compared three idealized two-dimensional hovering kinematics: a drag-based stroke in the vertical plane, a lift-based stroke in the horizontal plane, and a hybrid stroke on a tilted plane. I discovered that drag-based mechanisms produce more vertical force than lift-based mechanisms at $Re < 2$ and drag-based mechanisms have greater $\overline{C_V}/\overline{C_T}$ than lift-based mechanisms at $Re < 5$. A lift-based mechanism produced more vertical force at $Re>2$, and had greater $\overline{C_V}/\overline{C_T}$ at $Re>5$. Next, I explored how a faster downstroke and flexible wings might affect vertical force production. With a faster downstroke, I found an increase in vertical force and $\overline{C_V}/\overline{C_T}$ for a drag-based stroke in the vertical plane, although this effect was modest at lower *Re*. And with added flexibility, I discovered an increase in vertical force in a drag-based mechanism. The results of this study

suggest it is possible that a small insect could use a drag-based strategy to produce as much vertical force as a lift-based strategy at very low *Re*, but I am unaware of any insects that use a drag-based strategy. Regardless, this study demonstrated that neither lift- nor drag-based weight support mechanisms are efficient at $Re<100$, and particularly at $Re<20$, which is the range of the smallest flying insects. This may help explain the importance of additional flight strategies, such as bristled wings and wing-wing interactions.

In Chapter 4, I developed a two-dimensional model of a bristled insect wing using the IBFE method. The effect of Reynolds number, angle of attack, bristle spacing, and wing-wing interactions were investigated. The inverse relationship between force and G/D ratio was smaller at lower angles of attack, suggesting that bristled wings may act more like solid wings at lower angles of attack than they do at higher angles of attack. I also found that bristled wings significantly decreased the force required to fling two wings apart compared to solid wings, especially at lower Re_b. Following fling, and once the two wings were more than one half chord length apart, the force on each wing approached the drag experienced by a single wing. Although translational forces for solid and bristled wings were similar, the wing forces during fling were significantly reduced for the bristled case. These results support the idea that bristles may offer an aerodynamic benefit during clap and fling in tiny insects. Bristled wings could reduce the force required to fling the wings apart during clap and fling while still maintaining lift during translation. Additionally, it may be possible for the bristled wing to preserve lift by acting more like a solid plate during the translational part of the stroke, especially at smaller angles of attack.

In Chapter 5, I used the IBFE method to investigate aerodynamics forces and resulting flow structures generated by a revolving three-dimensional elliptical wing over a range of Reynolds numbers and angles of attack. To date, this is the first study to quantify the flow

structures around a three-dimensional wing at a range of angles of attack and *Re* relevant to the smallest flying insects (*Re* < 10). I compared the numerical results to those obtained by collaborators using a dynamically scaled physical wing model. I discovered that as *Re* decreased, drag increased significantly and flight became increasingly less efficient. At the range of flight experienced by the smallest insects (4<*Re*<32), both the LEV and TEV remained attached to the wing. Spanwise flow decreased with decreasing *Re*, especially in the range of the smallest flying insects.

Overall, the results of Chapters 3, 4, and 5 suggest that there are drastic differences in the aerodynamics of flight at the scale of the smallest flying insects, which makes their flight more challenging, compared to larger insects. As the Reynolds number decreases to that of the smallest insects (*Re* ~ 5), drag increases and the lift-to-drag ratio decreases significantly. Both the LEV and TEV remain attached to the wing and spanwise flow decreases. Additional flight strategies, such as bristled wings and wing-wing interactions, may offer a way for the smallest insects to overcome some of the challenges of flight at lower Reynolds numbers.

6.2 Limitations

There were many limitations to the studies presented in Chapters 3, 4, and 5. The greatest limitation in Chapters 3 and 4 was that the studies were conducted in two-dimensions. In general, two-dimensional studies fail to capture any effects from spanwise flow, and there can be differences in the separation of the LEV, especially at higher *Re* (Wang, Birch et al. 2004). Similarly, in Chapter 4, I expect that three-dimensional geometry and length of insect wing bristles will play an important role in their leakiness. While Chapter 5 considered the three-dimensional effects of a revolving wing, I only investigated the case of a single rigid wing engaged in steady rotation. I did not consider more complicated kinematics or the effects of

wing-wing interactions, such as clap and fling (Weis-Fogh 1973). A logical future direction in the analysis of flight of the smallest insects would be an investigation of the forces and flow structures around flexible wings and bristled wings engaged in clap and fling at the *Re* relevant to tiny insects.

Another limitation was that these studies placed great emphasis on the forces experienced by tiny insect wings. While lift and drag (and the ratio of the two) are certainly important to small insects, there are other important considerations when it comes to aerodynamic performance. For example, a tiny flier would need to find a compromise between force production, stability, maneuverability, control, and wing strength. Additional studies into the maneuverability, stability and control of insects at low *Re* would be beneficial to understanding the flight strategies employed.

REFERENCES

Alben, S., M. Shelley and J. Zhang (2002). "Drag reduction through self-similar bending of a flexible body." Nature **420**: 479-481.

Alben, S., M. Shelley and J. Zhang (2004). "How flexibility induces streamlining in a two-dimensional flow." Phys. Fluids **16**: 1694-1713.

Aono, H., F. Liang and H. Liu (2008). "Near-and far-field aerodynamics in insect hovering flight: an integrated computational study." Journal of Experimental Biology **211**(2): 239-257.

Arora, N., A. Gupta, S. Sanghi, H. Aono and W. Shyy (2014). "Lift-drag and flow structures associated with the “clap and fling” motion." Physics of Fluids (1994-present) **26**(7): 071906.

Austin, A. and M. Dowton (2000). Hymenoptera: Evolution, biodiversity and biological control. Australia, Csiro Publishing.

Ayaz, F. and T. J. Pedley (1999). "Flow through and particle interception by an infinite array of closely-spaced circular cylinders." European Journal of Mechanics B-Fluids **18**(2): 173-196.

Barta, E. (2011). "Motion of slender bodies in unsteady Stokes flow." Journal of Fluid Mechanics **688**: 66-87.

Barta, E. and D. Weihs (2006). "Creeping flow around a finite row of slender bodies in close proximity." Journal of Fluid Mechanics **551**: 1-17.

Bennet, L. (1973). "Effectiveness and flight of small insects." Annals of the Entomological Society of America **66**(6): 1187-1190.

Berman, G. J. and Z. Wang (2007). "Energy-minimizing kinematics in hovering insect flight." Journal of Fluid Mechanics **582**: 153-168.

Birch, J. M. and M. H. Dickinson (2001). "Spanwise flow and the attachment of the leading-edge vortex on insect wings." Nature **412**(6848): 729-733.

Birch, J. M., W. B. Dickson and M. H. Dickinson (2004). "Force production and flow structure of the leading edge vortex on flapping wings at high and low Reynolds numbers." Journal of Experimental Biology **207**(7): 1063-1072.

Borrell, B. J., J. A. Goldbogen and R. Dudley (2005). "Aquatic wing flapping at low Reynolds numbers: swimming kinematics of the Antarctic pteropod, Clione antarctica." Journal of Experimental Biology **208**(15): 2939-2949.

Bringley, T. T. and C. S. Peskin (2008). "Validation of a simple method for representing spheres and slender bodies in an immersed boundary method for Stokes flow on an unbounded domain." Journal of Computational Physics **227**(11): 5397-5425.

Bush, B. L. and J. D. Baeder (2007). Computational investigation of flapping-wing flight. 37th AIAA Fluid Dynamics Conference and Exhibit.

Cheer, A., S. Cheung, T. C. Hung, R. H. Piedrahita and S. L. Sanderson (2012). "Computational fluid dynamics of fish gill rakers during crossflow filtration." Bull Math Biol **74**: 981-1000.

Cheer, A. Y. L. and M. A. R. Koehl (1987). "Paddles and rakes: Fluid flow through bristled appendages of small organisms." Journal of theoretical biology **129**: 17-39.

Childress, S. (1981). Mechanics of swimming and flying, Cambridge University Press.

Childs, H. (2013). "VisIt: An end-user tool for visualizing and analyzing very large data."

Crespi, B. J., D. A. Carmean and T. W. Chapman (1997). "Ecology and evolution of galling thrips and their allies." Annu. Rev. Entomol. **42**: 51-71.

Davidi, G. and D. Weihs (2012). "Flow around a comb wing in low-Reynolds-number flow." AIAA Journal **50**(1): 249-252.

Dickinson, M. H. and K. G. Gotz (1993). "Unsteady aerodynamic performance of model wings at low Reynolds numbers." J. Exp. Biol. **174**: 45-64.

Dickinson, M. H., F.-O. Lehmann and S. P. Sane (1999). "Wing rotation and the aerodynamic basis of insect flight." Science **284**(5422): 1954-1960.

Dickinson, M. H., F. O. Lehmann and S. P. Sane (1999). "Wing rotation and the aerodynamic basis of insect flight." Science **284**: 1954-1960.

Dudley, R. (2002). The biomechanics of insect flight: form, function, evolution, Princeton University Press.

Ellington, C. (1984). "The aerodynamics of hovering insect flight. I. The quasi-steady analysis." Philosophical Transactions of the Royal Society of London. B, Biological Sciences **305**(1122): 1-15.

Ellington, C. P. (1975). Swimming and Flying in Nature Vol. 2. New York, Plenum Press.

Ellington, C. P. (1980). "Wing mechanics and take-off preparation of Thrips (Thysanoptera)." J. Exp. Biol. **85**: 129-136.

Ellington, C. P. (1984). "The aerodynamics of hovering insect flight. III. Kinematics." Philos. Trans. R. Soc. Lond. B Biol. Sci. **305**: 79-113.

Ellington, C. P. (1984). "The aerodynamics of hovering insect flight. IV. Aerodynamic mechanisms." Philos. Trans. R. Soc. Lond. B Biol. Sci. **305**: 79-113.

Ellington, C. P. (1999). "The novel aerodynamics of insect flight: applications to micro-air vehicles." Journal of Experimental Biology **202**(23): 3439-3448.

Ellington, C. P., C. Van Den Berg, A. P. Willmott and A. L. Thomas (1996). "Leading-edge vortices in insect flight."

Etnier, S. A. and S. Vogel (2000). "Reorientation of daffodil (Narcissus Amaryllidaceae) flowers in wind: drag reduction and torsional flexibility." American journal of botany **87**: 29-32.

Fauci, L. J. and A. L. Fogelson (1993). "Truncated Newton methods and the modeling of complex immersed elastic structures." Communications on Pure and Applied Mathematics **46**(6): 787-818.

Fauci, L. J. and C. S. Peskin (1988). "A computational model of aquatic animal locomotion." Journal of Computational Physics **77**(1): 85-108.

Ferner, M. C. and B. Gaylord (2008). "Flexibility foils filter function: structural limitations on suspension feeding." Journal of Experimental Biology **211**(22): 3563-3572.

Fornberg, B. (1991). "Steady incompressible-flow past a row of circular-cylinders." Journal of Fluid Mechanics **225**: 655-671.

Gajjar, J. S. B. and N. A. Azzam (2004). "Numerical solution of the Navier-Stokes equations for the flow in a cylinder cascade." Journal of Fluid Mechanics **520**: 51-82.

Gazzola, M., W. M. Van Rees and P. Koumoutsakos (2012). "C-start: optimal start of larval fish." Journal of Fluid Mechanics **698**: 5-18.

Geuzaine, C. and J. F. Remacle (2009). "Gmsh: A 3-D finite element mesh generator with built-in pre-and post-processing facilities." International Journal for Numerical Methods in Engineering **79**(11): 1309-1331.

Griffith, B. E. (2012). "Immersed boundary model of aortic heart valve dynamics with physiological driving and loading conditions." International Journal for Numerical Methods in Biomedical Engineering **28**(3): 317-345.

Griffith, B. E., R. D. Hornung, D. M. McQueen and C. S. Peskin (2007). "An adaptive, formally second order accurate version of the immersed boundary method." Journal of Computational Physics **223**(1): 10-49.

Griffith, B. E. and X. Luo (2012). "Hybrid finite difference/finite element version of the immersed boundary method." Submitted in revised form.

Griffith, B. E., X. Y. Luo, D. M. McQueen and C. S. Peskin (2009). "Simulating the fluid dynamics of natural and prosthetic heart valves using the immersed boundary method." International Journal of Applied Mechanics **1**(1): 137-177.

Grimaldi, D. and M. S. Engel (2005). Evolution of the Insects, Cambridge University Press.

Grunbaum, D., D. Eyre and A. Fogelson (1998). "Functional geometry of ciliated tentacular arrays in active suspension feeders." Journal of Experimental Biology **201**(18): 2575-2589.

Harbig, R., J. Sheridan and M. Thompson (2013). "Reynolds number and aspect ratio effects on the leading-edge vortex for rotating insect wing planforms." Journal of Fluid Mechanics **717**: 166-192.

Hedrick, T. L., B. Cheng and X. Deng (2009). "Wingbeat Time and the Scaling of Passive Rotational Damping in Flapping Flight." Science **324**(5924): 252-255.

Herschlag, G. and L. Miller (2011). "Reynolds number limits for jet propulsion: a numerical study of simplified jellyfish." Journal of theoretical biology **285**(1): 84-95.

Heys, J. J., T. Gedeon, B. C. Knott and Y. Kim (2008). "Modeling arthropod filiform hair motion using the penalty immersed boundary method." Journal of Biomechanics **41**: 977-984.

Horridge, G. A. (1956). "The flight of very small insects." Nature **178**: 1334-1335.

Huber, J. T. and J. S. Noyes (2013). "A new genus and species of fairyfly, Tinkerbella nana (Hymenoptera, Mymaridae), with comments on its sister genus Kikiki, and discussion on small size limits in arthropods." Journal of Hymenoptera Research **32**: 17-44.

Jones, D. R. (2005). "Plant viruses transmitted by thrips." European Journal of Plant Pathology **113**(2): 119-157.

Kim, Y. and C. S. Peskin (2007). "Penalty immersed boundary method for an elastic boundary with mass." Physics of Fluids (1994-present) **19**(5): 053103.

Koehl, M. A. R. (1984). "How do benthic organisms withstand moving water?" Amer. Zool. **24**: 57-70.

Koehl, M. A. R. (1993). "Hairy little legs: feeding, smelling and swimming at low Reynolds numbers." Contemporary Mathematics **141**: 33-64.

Kolomenskiy, D., H. Moffatt, M. Farge and K. Schneider (2011). "Two-and three-dimensional numerical simulations of the clap–fling–sweep of hovering insects." Journal of Fluids and Structures **27**(5): 784-791.

Kolomenskiy, D., H. K. Moffatt, M. Farge and K. Schneider (2010). "Vorticity generation during the clap–fling–sweep of some hovering insects." Theoretical and Computational Fluid Dynamics **24**(1-4): 209-215.

Kuethe, A. M. (1975). Swimming and Flying in Nature Vol. 2. New York, Plenum Press.

Lehmann, F. O. and S. Pick (2007). "The aerodynamic benefit of wing-wing interaction depends on stroke trajectory in flapping insect wings." J. Exp. Biol. **210**: 1362-1377.

Lehmann, F. O., S. P. Sane and M. Dickinson (2005). "The aerodynamic effects of wing-wing interaction in flapping insect wings." J. Exp. Biol. **208**: 3075-3092.

Lentink, D. and M. H. Dickinson (2009). "Rotational accelerations stabilize leading edge vortices on revolving fly wings." Journal of Experimental Biology **212**(16): 2705-2719.

Lighthill, M. J. (1973). "On the Weis-Fogh mechanism of lift generation." J. Fluid Mech **60**: 1-17.

Lim, S. and C. S. Peskin (2012). "Fluid-mechanical interaction of flexible bacterial flagella by the immersed boundary method." Physical Review E **85**(3).

Liu, H. and H. Aono (2009). "Size effects on insect hovering aerodynamics: an integrated computational study." Bioinspiration & Biomimetics **4**(1): 015002.

Loudon, C., B. A. Best and M. A. R. Koehl (1994). "When does motion relative to neighboring surfaces alter the flow through an array of hairs?" J. Exp. Biol. **193**: 233-254.

Maniyeri, R., Y. K. Suh, S. Kang and M. J. Kim (2012). "Numerical study on the propulsion of a bacterial flagellum in a viscous fluid using an immersed boundary method." Computers & Fluids **62**: 13-24.

Maxworthy, T. (1979). "Experiments on the Weis-Fogh mechanism of lift generation by insects in hovering flight. Part 1. Dynamics of the fling." J. Fluid Mech **93**: 47-63.

McMasters, J. H. (1989). "The Flight of the Bumblebee and Related Myths of Entomological Engineering: Bees help bridge the gap between science and engineering." American Scientist: 164-169.

Miller, L. A. and C. S. Peskin (2004). "When vortices stick: an aerodynamic transition in tiny insect flight." J. Exp. Biol. **207**: 3073-3088.

Miller, L. A. and C. S. Peskin (2005). "A computational fluid dynamics study of 'clap and fling' in the smallest insects." J. Exp. Biol. **208**: 17.

Miller, L. A. and C. S. Peskin (2009). "Flexible clap and fling in tiny insect flight." J. Exp. Biol. **212**: 3076-3090.

Miller, L. A., A. Santhanakrishnan, S. Jones, C. Hamlet, K. Mertens and L. Zhu (2012). "Reconfiguration and the reduction of vortex-induced vibrations in broad leaves." J. Exp. Biol. **215**: 2716-2727.

Morse, J. G. and M. S. Hoddle (2006). "Invasion biology of thrips." Annu. Rev. Entomol. **51**: 67-89.

Müller, U. K., J. G. van den Boogaart and J. L. van Leeuwen (2008). "Flow patterns of larval fish: undulatory swimming in the intermediate flow regime." Journal of Experimental Biology **211**(2): 196-205.

Müller, U. K. and J. L. van Leeuwen (2004). "Swimming of larval zebrafish: ontogeny of body waves and implications for locomotory development." Journal of Experimental Biology **207**(5): 853-868.

Nakata, T. and H. Liu (2012). "Aerodynamic performance of a hovering hawkmoth with flexible wings: a computational approach." Proceedings of the Royal Society of London B: Biological Sciences **279**(1729): 722-731.

Nguyen, H., L. Karp-Boss, P. A. Jumars and L. Fauci (2011). "Hydrodynamic effects of spines: A different spin." Limnology and Oceanography: Fluids and Environments **1**: 110-119.

Osborne, M. (1951). "Aerodynamics of flapping flight with application to insects." Journal of Experimental Biology **28**(2): 221-245.

Palmer, J. M., D. V. R. Reddy, J. A. Wightman and G. V. Ranga Rao (1990). "New information on the thrips vectors of tomato spotted wilt virus in groundnut crops in India." International Arachis Newsletter **7**: 24-25.

Peskin, C. S. (2002). "The immersed boundary method." Acta Numerica **11**: 479-517.

Peskin, C. S. and D. M. McQueen (1996). Fluid dynamics of the heart and its valves. New Jersey, Prentice-Hall.

Peterson, I. (2004). "Flight of the Bumblebee." Science News **116**(11).

Purcell, E. M. (1977). "Life at low Reynolds number." Am. J. Phys **45**(1): 3-11.

Ramamurti, R. and W. C. Sandberg (2007). "A computational investigation of the three-dimensional unsteady aerodynamics of Drosophila hovering and maneuvering." Journal of Experimental Biology **210**(5): 881-896.

Ristroph, L., A. J. Bergou, J. Guckenheimer, Z. J. Wang and I. Cohen (2011). "Paddling Mode of Forward Flight in Insects." Physical Review Letters **106**(17).

Sane, S. P. (2003). "The aerodynamics of insect flight." The journal of experimental Biology **206**(23): 4191-4208.

Sane, S. P. and M. H. Dickinson (2001). "The control of flight force by a flapping wing: lift and drag production." Journal of experimental biology **204**(15): 2607-2626.

Santhanakrishnan, A., A. K. Robinson, S. Jones, A. A. Low, S. Gadi, T. L. Hedrick and L. A. Miller (2014). "Clap and fling mechanism with interacting porous wings in tiny insect flight." The Journal of experimental biology **217**(21): 3898-3909.

Satterlie, R. A., M. LaBarbera and S. A. N (1985). "Swimming in the Pteropod Mollusc, Clione Umacina: I. Behaviour and Morphology." Journal of Experimental Biology **116**(1): 189-204.

Shogren, C. and T. Paine (2015). "Economic Benefit for Cuban Laurel Thrips Biological Control." Journal of economic entomology: tov283.

Sotavalta, O. (1947). The Flight-tone (wing-stroke Frequency) of Insects:(contributions to the Problem of Insect Flight I), Suomen Hyönteistieteellinen Seura.

Spedding, G. R. and T. Maxworthy (1986). "The generation of circulation and lift in a rigid two-dimensional fling." J. Fluid Mech **165**: 247-272.

Srygley, R. and A. Thomas (2002). "Unconventional lift-generating mechanisms in free-flying butterflies." Nature **420**(6916): 660-664.

Sun, M. and Y. Xin (2003). "Flows around two airfoils performing fling and subsequent translation and translation and subsequent clap." Acta Mechanica Sinica **19**: 13-117.

Sun, M. and X. Yu (2006). "Aerodynamic force generation in hovering flight in a tiny insect." AIAA Journal **44**(7): 1532-1540.

Sunada, S., H. Takashima, T. Hattori, K. Yasuda and K. Kawachi (2002). "Fluid-dynamic characteristics of a bristled wing." J. Exp. Biol. **205**: 2737-2744.

Tamada, K. and H. Fujikawa (1957). "The steady two dimensional flow of viscous fluid at low Reynolds numbers passing through an infinite row of equal parallel circular cylinders." Q. J. Mech. Appl. Maths **10**: 426-432.

Terry, I. (2001). "Thrips and weevils as dual, specialist pollinators of the Australian cycad Macrozamia communis (Zamiaceae)." International Journal of Plant Sciences **162**(6): 1293-1305.

Terry, I. (2002). Thrips: the primeval pollinators. Thrips and Tospoviruses: Proceedings of the 7th International Symposium on Thysanoptera.

Thompson, D. W. (1942). "On growth and form." On growth and form.

Tytell, E. D., C. Y. Hsu, T. L. Williams, A. H. Cohen and L. J. Fauci (2010). "Interactions between internal forces, body stiffness, and fluid environment in a neuromechanical model of lamprey swimming." Proceedings of the National Academy of Sciences of the United States of America **107**(46): 19832-19837.

Ullman, D. E., R. Meideros, L. R. Campbell, A. E. Whitfield, J. L. Sherwood and T. L. German (2002). "Thrips as vectors of tospoviruses." Advances in Botanical Research **36**: 113-140.

Usherwood, J. R. and C. P. Ellington (2002). "The aerodynamics of revolving wings I. Model hawkmoth wings." J. Exp. Biol. **205**: 1547-1564.

Vo, G. D. and J. Heys (2011). "Biofilm Deformation in Response to Fluid Flow in Capillaries." Biotechnology and Bioengineering **108**(8): 1893-1899.

Vogel, S. (1981). Life in Moving Fluids: The Physical Biology of Flow. Boston, Willard Grant Press.

Vogel, S. (1989). "Drag and reconfiguration of broad leaves in high winds." J. Exp. Biol. **40**: 941-948.

Vogel, S. (1996). Life in moving fluids: the physical biology of flow, Princeton University Press.

Wang, Z. J. (2000). "Two dimensional mechanism for insect hovering." Phys. Rev. Let. **85**(10): 2216-2219.

Wang, Z. J. (2004). "The role of drag in insect hovering." Journal of Experimental Biology **207**(23): 4147-4155.

Wang, Z. J., J. M. Birch and M. H. Dickinson (2004). "Unsteady forces and flows in low Reynolds number hovering flight: two-dimensional computations vs robotic wing experiments." Journal of Experimental Biology **207**(3): 449-460.

Weihs, D. and E. Barta (2008). "Comb-wings for flapping flight at extremely low Reynolds numbers." AIAA Journal **46**(1): 285-288.

Weis-Fogh, T. (1973). "Quick estimates of flight fitness in hovering animals, including novel mechanisms for lift production." J. Exp. Biol. **59**: 169-230.

Weis-Fogh, T. (1975). "Unusual mechanisms for the generation of lift in flying animals." Scientific American **233**(5): 81-87.

White, C. M. (1946). "The drag of cylinders in fluids at slow speeds." Proc. R. Soc. A **186**(1007): 472-479.

Wilson, M. M., J. Peng, J. O. Dabiri and J. D. Eldredge (2009). "Lagrangian coherent structures in low Reynolds number swimming." Journal of Physics: Condensed Matter **21**(20): 204105.

Wu, J. H. and M. Sun (2004). "Unsteady aerodynamic forces of a flapping wing." Journal of Experimental Biology **207**(7): 1137-1150.

Xu, N. and M. Sun (2014). "Lateral dynamic flight stability of a model hoverfly in normal and inclined stroke-plane hovering." Bioinspiration & biomimetics **9**(3): 036019.

Zanker, J. (1990). "The wing beat of Drosophila melanogaster. I. Kinematics." Philosophical Transactions of the Royal Society of London. B, Biological Sciences **327**(1238): 1-18.

Żbikowski, R. (2002). "On aerodynamic modelling of an insect–like flapping wing in hover for micro air vehicles." Philosophical Transactions of the Royal Society of London A: Mathematical, Physical and Engineering Sciences **360**(1791): 273-290.

Zheng, L., T. Hedrick and R. Mittal (2013). "A comparative study of the hovering efficiency of flapping and revolving wings." Bioinspiration & biomimetics **8**(3): 036001.

Zheng, L., T. L. Hedrick and R. Mittal (2013). "A multi-fidelity modelling approach for evaluation and optimization of wing stroke aerodynamics in flapping flight." Journal of Fluid Mechanics **721**: 118-154.